MUSE spectroscopy of horizontal branch stars in the globular clusters ω Cen and NGC 6752

Bachelorarbeit aus der Physik

Vorgelegt von

Steven Hämmerich

05.10.2017

Dr. Karl Remeis Sternwarte
Friedrich-Alexander-Universität Erlangen-Nürnberg

Betreuer: Prof. Dr. Ulrich Heber, Dr. Marilyn Latour

" ἐρωτηθείς ποτε εἰς τί γεγέννηται, ´ εἰς θεωρίαν, ´ ἔφη, ´ ἡλίου καὶ σελήνης καὶ οὐρανοῦ.´ "
-D. Laertius, Lives of eminent philosophers, 2.3-

Abstract

Globular clusters (GCs) are old objects, hence they are excellent laboratories to study stellar populations and evolution. The horizontal branch (HB) is of particular interest since its morphology varies from cluster to cluster. In color magnitude diagrams (CMDs) some clusters show blue and extreme horizontal branch (BHB, EHB) stars, while an even more extreme part, the blue-hook, is only observed in rare cases. Additionally, this population in GCs is very different from the field population. In order to understand these stars, especially their properties and evolution and the differences between the field and GC population, it is necessary to further characterize these stars.

Optical spectra of 121 BHB, EHB and blue-hook stars in ω Cen and 43 BHB and EHB stars in NGC 6752 obtained with the integral field spectrograph MUSE were preselected from the CMDs. Since this instrument has never been used to analyze this population, it is important to explore its capabilities. In addition, this population has never been analyzed spectroscopically in the center region of the two program clusters.

A quantitative spectral analysis of all available MUSE spectra of sufficient quality is performed. The hydrogen and helium lines present in the spectra are fit with a gird of metal-line blanketed LTE models, in order to derive the radial velocity, effective temperature, surface gravity, and helium abundance.

The effective temperatures measured cover a wide range starting at 12,000 K and ranging up to 41,000 K in ω Cen and 33,000 K in NGC 6752. In the T_{eff} -log g diagram most stars fall onto the theoretical HB band, which means that they are indeed HB objects and thus are helium core burning. In ω Cen and NGC 6752, the BHB and EHB stars are helium deficient and the trends observed are similar to those observed in the field population. However, due to the limits of the model grid used, the helium content of some stars, likely the blue-hook stars in ω Cen, could not be quantified, but it can be concluded that they are most likely helium-rich.

Since MUSE observed stars in the central region of the clusters, this analysis allows for the comparison of the atmospheric parameters of BHB, EHB, and blue-hook stars located in the outer region of the cluster, to where previous studies were limited for observations, to the ones derived for the central region. Although previous studies used spectra of bluer range, higher quality and higher spectral coverage, the derived parameters turn out to be of sufficient quality to allow a detailed comparison. The parameters in the T_{eff} -log g and T_{eff} -helium abundance diagrams are identical with those derived for the outer regions within the uncertainties. Therefore, it can be concluded that the stars in the

inner and outer region have the same properties and that environmental factors, such as stellar density, do not influence the formation of BHB, EHB and blue-hook stars. It also can be concluded that the results presented support the literature values. A good agreement with the expectations is observed. The results pave the way for using MUSE to study the different HBs of GCs and to finally answer the longstanding question what causes the different morphologies.

Table of Contents

List of Tables

List of Figures

1

Globular clusters

For multiple reasons, globular clusters (GCs) are very interesting and intriguing objects. GCs are spherical, dense groups of stars. It is assumed that GCs are in general old objects and formed at about the same time as their host galaxies, hence they can be used to study the conditions at the time the galaxy formed. In the past, GCs revealed some important properties of the Galaxy. Up until the 1900s, it was believed that the solar system is close to the center of the Milky Way, but at that time scientists realized that GCs seem to cluster in a slightly small region in the sky, also it was assumed that GCs are spherically distributed around the center of the Milky Way, which is indeed true. The only reasonable way to explain these findings was that the solar system is further from the center than thought. In addition, also the distance measurements conducted showed that the galaxy is much bigger than assumed.

Since they are spherically distributed but concentrated towards the galactic center, it is fairly easy to observe GCs towards the Galactic center, and because GCs are old objects and their stars formed at the same time they are very suitable objects to study stellar evolution. Due to their high age it is possible to observe all phases of stellar evolution. With the advancements in nuclear physics, it was possible to derive evolution-models for stars. These theories were first tested on GCs for obvious reasons.

In the 1970s, it was discovered that GCs exist within many galaxies in the Local group and also beyond. Thus globular clusters are of high importance to study galaxy formation (Ashman and Zepf 1998).

As this brief review of the research on GCs within roughly the last 100 years demonstrates, GCs are important objects to study all kinds of astronomical and astrophysical phenomena. In this section, a general overview on the properties of GCs will be given. This chapter is mainly based on following reviews: Ashman and Zepf (1998); Harris and Racine (1979); Vandenberg et al. (1996); Gratton et al. (2004); Freeman and Norris (1981).

1.1 Space-distribution in the Milky Way

The Milky Way has about 150 known GCs, but due to effects such as obscuration by the Galactic bulge, the number most likely is underestimated. The actual amount of GCs is most likely between 160 and 200. About half of all GCs are within a distance of 5 kpc from the galactic center, but GCs can also be found at galactocentric distances well beyond 100 kpc. GCs are mostly distributed spherically around the galactic center (see Fig. 1.1) especially the metal-poor ones, so they show a halo distribution. The metal-rich may belong to the Galactic Bulge. Due to this distribution and interstellar extinction, most GCs can be observed around, so above or below, the Galactic center.
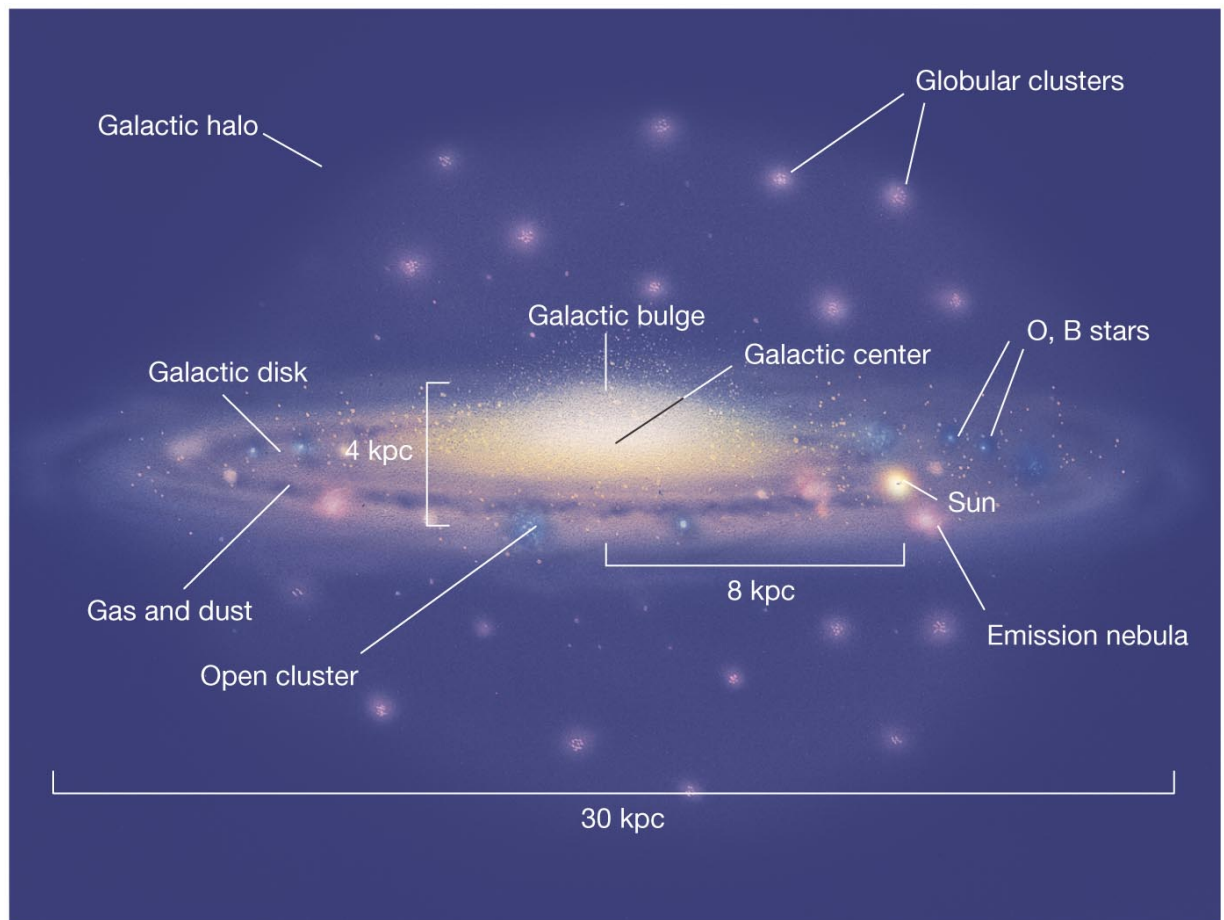
Figure 1.1: Distribution of GCs in the Milky Way [1]

---

[1]http://pages.uoregon.edu/jimbrau/BrauImNew/Chap23/6th/23_10Figure-F.jpg (last accessed: 25.07.2017, 16:27)

1.2 The color-magnitude diagram and stellar evolution
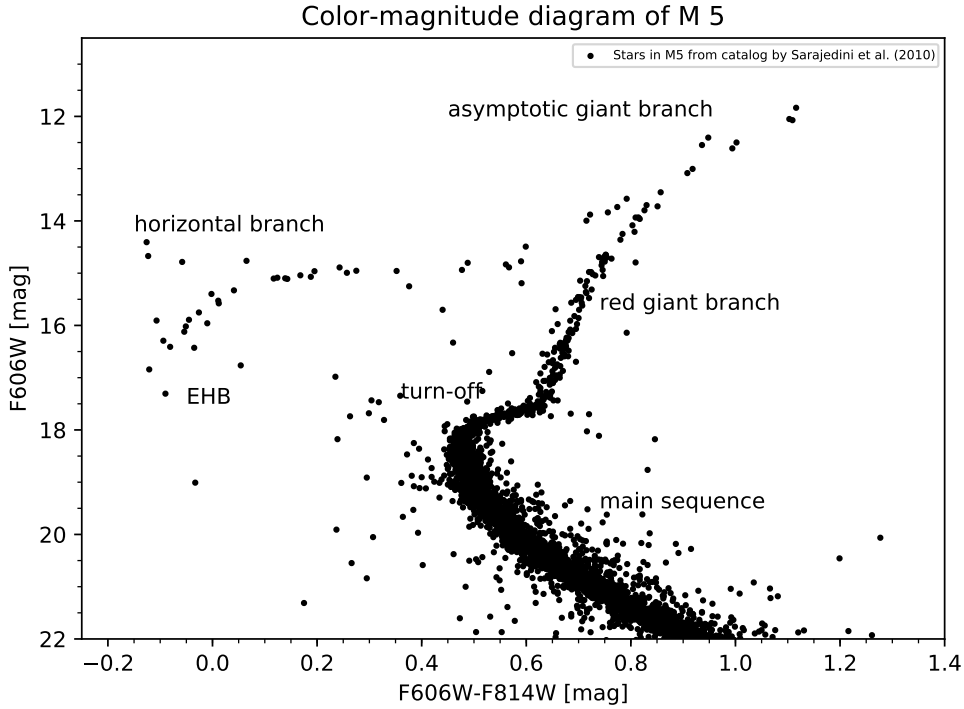
Figure 1.2: Color-magnitude diagram of M 5

The color-magnitude diagram (CMD) is a powerful instrument to visualize all kinds of properties of GCs. In the CMD, the apparent magnitude is plotted against a color index. Figure 1.2 shows the CMD of the GC M 5. This CMD was created using data from a catalog by Sarajedini et al. (2010). Since the purpose of this CMD is to illustrate the general properties of these diagrams, only every tenth data-point was used.

Stars of a certain stage of stellar evolution have distinctive positions in the CMD, meaning a CMD illustrates stellar evolution. GCs have a well defined main sequence (MS). Stars on this sequence produce energy through the fusion of hydrogen to helium. In the CMD, the MS extends from low magnitudes up to the turn off (TO), the point where stars leave the MS because their hydrogen fuel vanishes. Fainter MS stars are redder than MS stars near the TO-point. Parameters such as age and chemical composition influence the morphology of the MS in the CMD. Most GCs have very narrow MS in the CMD which leads to the assumption that, in those cases, all MS stars share a similar chemical composition.

The TO-point is located at the luminous end of the MS. The TO in GCs occurs at fainter luminosities than in the field, indicating that GCs are old objects. The metallicity of the cluster influences the position of the TO-point. For high metallicities, the TO is shifted to the redder and fainter region of the CMD at a given age. A sharp TO, which is often

observed in GC, indicates that the stars of the GC were all formed at the same time.
The red giant branch (RGB) is connected to the MS through the sub-giant sequence. After their MS life, stars ignite hydrogen burning in their shell. As the hydrogen burning shell travels towards the outer layers of the star, the star becomes brighter and travels upwards in the CMD. Reaching the tip of the RGB, the star ignites helium in its core and wanders off towards the horizontal branch (HB). The morphology of the RGB is also influenced by the metallicity of the cluster. Higher metallicity causes the branch to be more shallow and redder in the CMD. The reason for this phenomenon is the same as for the morphology of the MS.

The HB consists of stars with helium burning cores, which evolved of the RGB. The RR-Lyrae instability strip separates the blue and the red parts of the horizontal branch. RR-Lyrae stars are luminosity variable. The morphologies of the HBs are a very complex issue. At least two parameters have an influence on it, as will be discussed in detail later on.

Once the helium burning in the core is exhausted, a phase of helium-shell burning begins. This causes the star to change its place in the CMD again. Stars then ascend the so called asymptotic giant branch (AGB). Multiple effects cause a significant mass loss for stars on the AGB. One mechanism, for example, is a strong stellar wind. This mass loss makes it fairly difficult to predict the post-AGB phase of stellar evolution in GCs. Low mass stars evolve to become white dwarfs (WD).

Their cooling sequence is not shown in Fig. 1.2. This sequence is located beneath the MS.

So-called blue stragglers can be found beneath the HB and next to the MS. These stars are an extension of the MS since they are bluer and more luminous than TO stars, thus seem to be younger. Many theories have been proposed to explain the presence of these stars and probably more than one scenario can explain them. For example, blue stragglers could be stars formed later than all the other stars in the cluster which also explains their name. They could also be produced by mass transfer in binary systems or be formed via stellar collisions. Another important part of the CMD is the so called extreme horizontal branch (EHB). Actually, this sequence is just the blue extension of the HB. This part is vertically orientated towards lower luminosities, but not all GCs show EHBs in their CMDs. As for the HB, this sequence will be characterized later on.

1.3 Age of globular clusters

The age of GCs is a very important property because it indicates the role GCs play in the Galaxy halo and bulge as well as their relevance for galaxy formation. Since GCs are really old objects they provide a lower limit for the age of the universe and allow us to study the oldest stars known. The age of GCs can be determined through the CMD. Since all the stars are assumed to have formed at the same time, the TO-point allows to determine the age of the cluster. This estimate results in the most accurate age measurements for halo objects. From the position of the TO in the CMD, the distance to the cluster and the reddening in the line of sight, the absolute magnitude is estimated.

Then, by making use of stellar atmosphere models, the bolometric magnitude and effective temperature are derived. These results are used to estimate the age of the star via stellar interior models.

The age also depends on the metallicity of the cluster since the position of the TO is influenced by metallicity, as can be seen in Fig. 1.3. In general, it is expected that the metal-poor clusters are older since the fraction of heavy elements was lower at their time of formation. These clusters were assumed to be about 15 Gyr old, but new revised ages are younger. The uncertainties arise from the uncertainties of the distance, metallicity and other parameters influencing the models used. These models put the oldest clusters in an age range between 11 and 21 Gyr. Younger or older clusters seem to be highly unlikely. The age estimations are also used to put a lower limit on the age of the universe. At a 95 % confidence level a lower limit of 11.2 Gyr can be derived (Krauss and Chaboyer 2003). This puts the galactic GCs in an age range between 11 Gyr and 13 Gyr.

Another interesting relation is the relative age difference between GCs since it puts constraints on the time it took to form the GC-system and on halo formation time. The age difference is determined by comparing the luminosity of the TO-point and HB of the clusters. This method yields far smaller uncertainties than the absolute age-estimation. For metal-poor clusters the age spread is about 0.8 Gyr but there are also clusters showing a larger age spread. Clusters such as Pal 12 seem to be 3 Gyr younger than most clusters. In the case of Pal 12, its chemical composition and age difference indicate that this particular cluster was probably acquired from another dwarf galaxy in the Local group.
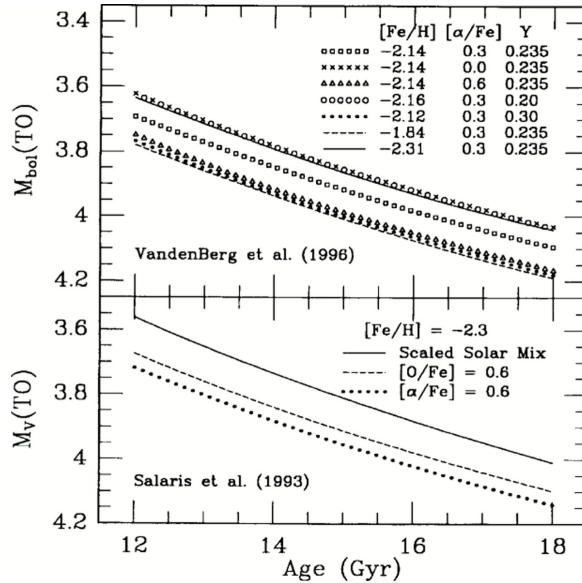
Figure 1.3: Relation between the TO-point and the age of the cluster, considering different metallicities (Vandenberg et al. 1996)

1.4 Chemical composition

The chemical abundance is an important property because it constrains the formation and evolution of the GC. The metallicity depends on the GC age, which means that the metal-poor ones should be older, which is logical since metals are formed in stars and the longer ago a star formed, the lower the initial metallicity at the time of formation was in the universe (see Fig. 1.4). Compared to the field population, stars in GCs show a smaller spread of metallicity, supporting the assumption that the stars formed at the same time. One cluster however, ω Cen, shows a large spread. This cluster has multiple subpopulations, as can be seen in Fig. 1.5, indicating a prolonged star formation. The different MSs of this cluster show different metallicities. Findings suggest that the metallicity also depends on the position of the cluster in the galaxy, with clusters nearer to the center of the Galaxy showing higher metal-abundances. There are also links between the abundances of certain elements. For example, there is a link between the abundances of carbon and nitrogen. The carbon abundance decreases while the star ascends the giant branch and at the same time the abundance of nitrogen increases. Many more correlations between other elements can be found. These correlations are important since they are directly linked to the different origin scenarios for stars, especially for the HB stars.
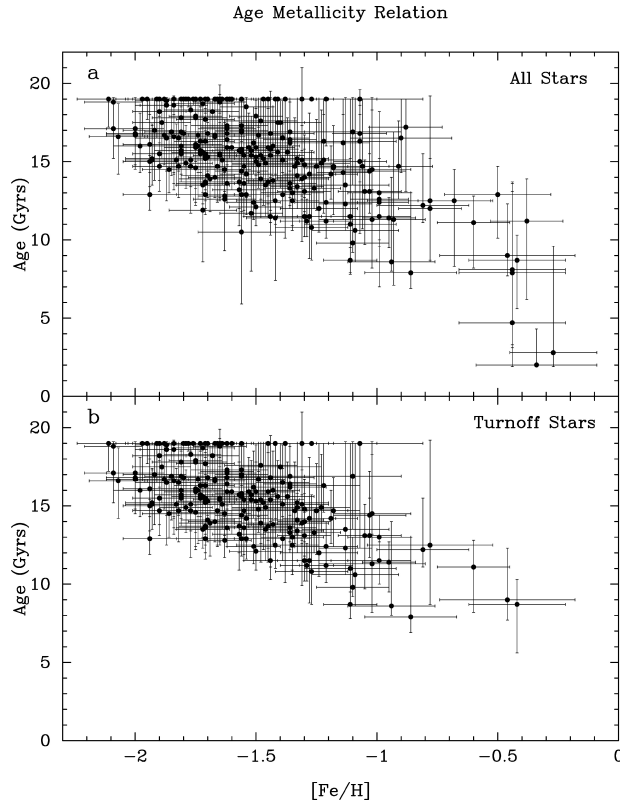
Figure 1.4: Relation between age and metallicity in ω Cen (Gratton et al. 2004)
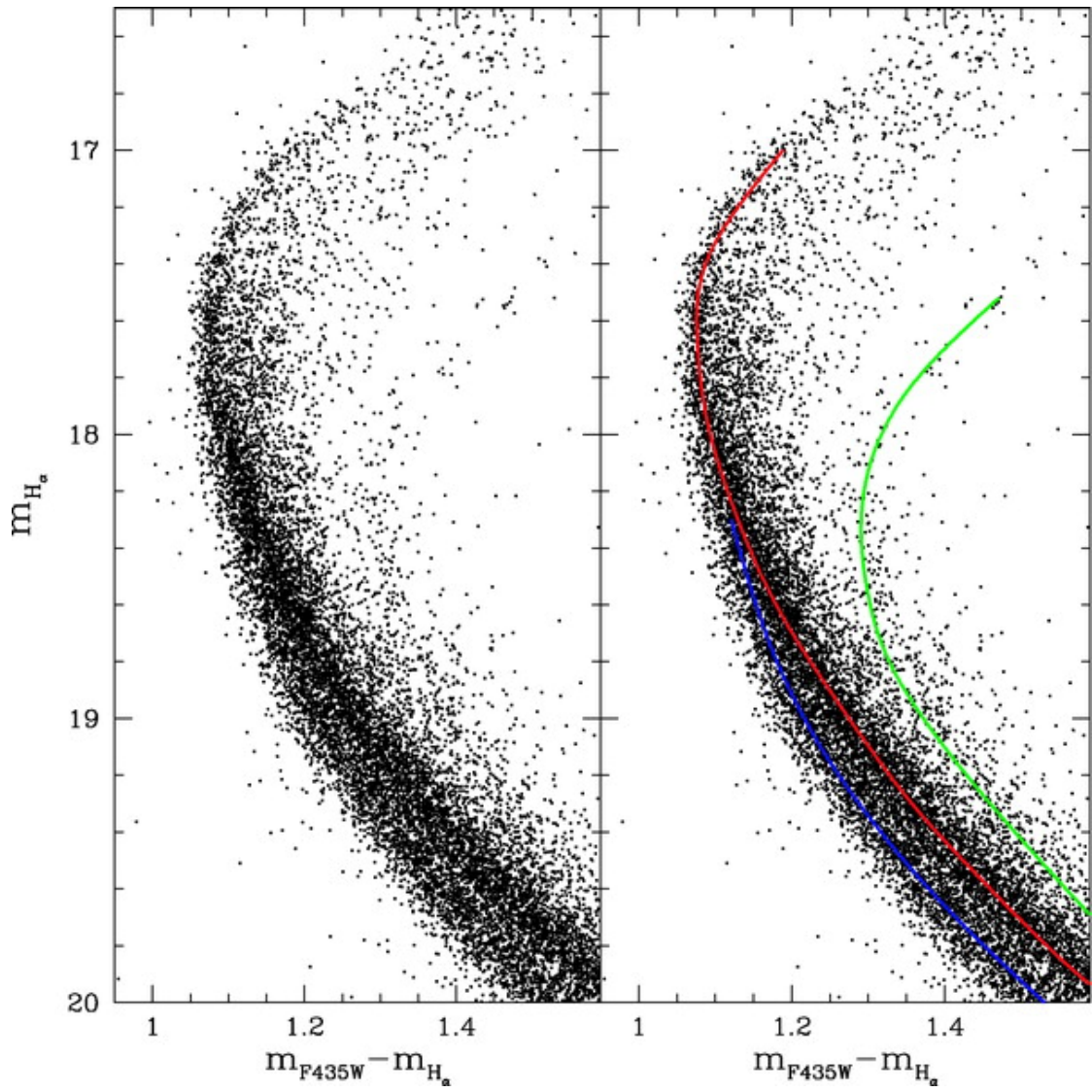
Figure 1.5: Different main sequences in ω Cen with different metallicities (Villanova et al. 2007)

1.5 Dynamics and structure of globular clusters

1.5.1 Shape and structure

GCs have spherical shapes. The apparent ellipticity of a GC defines how round a GC appears to be. Most GCs have an ellipticity of $\epsilon = 0.2$, so they appear to be relatively round. Compared to elliptical galaxies this is a low value. The ellipticity of GCs can be linked to the rotation of the cluster, contrary to elliptical galaxies, where the velocity-dispersion seems to cause the ellipticity. The latter can not explain the ellipticity in GCs, because the relaxation-time in the center region, where most measurements are conducted, is short. The low ellipticity of GCs is found amongst all ages, indicating that the reason for this phenomenon is linked to the formation of GCs.
GCs all share one quite obvious feature, the existence of a core region. A large fraction of the stars is located in this region, meaning the stellar density is quite high although there are large variations of this density among GCs.

1.5.2 Dynamical properties

The dynamics of stars in GCs are a complex subject. In general stars in more massive clusters reach higher velocities than those in less massive ones. The velocity-dispersion increases towards the center of the cluster. Since the stellar density in GCs is high, dynamical encounters between stars occur quite often, causing an even distribution of kinetic energy amongst the stars. This leads to mass segregation. The massive stars are decelerated, while the low mass stars are accelerated during gravitational encounters. One consequence is that the low mass stars occupy the outer region of the cluster and the massive ones the inner.
One interesting question is whether the dynamics in the inner region could be dominated by a black hole. In the past, this option was neglected, but new dynamical analyses of inner regions could possibly be explained by the presence of a central intermediate mass black hole, so it could be that some GCs contain a black hole, but also other scenarios, such as other stellar remnants, could explain the observed velocity-dispersion, as shown in Fig. 1.6.
The overall rotation of GCs is relatively low, but some studies find some GCs to have a strong rotation (van de Ven et al. 2006). There are two possible ways to explain the low rotation. The first option is that GCs are born with low angular momentum, which could be, for example, explained by a collapse scenario. The second option is that GCs somehow lose angular momentum during their evolution. This could be accomplished by the escape of stars that carry away angular momentum from the cluster. This escape could be caused for example by dynamical encounters of stars, in particular during the cluster formation process. This of course would lead to mass segregation. Theoretical calculations show that a cluster would become more spherical if this process was present, which would indicate that GCs become more spherical over time and that, at least in the beginning of their lifetime, GCs could be similar to elliptical galaxies. Some GCs show a so called core collapse, in this process, the density of the core increases over time

because the core shrinks. This shrinking causes the stars to move faster and some to leave the core, which again causes the core to shrink. This process then continues, which, of course, means that the density function of the cluster changes.

Dynamical analysis of the galaxy revealed the presence of dark matter. Current observations can not rule out entirely that GCs do not contain dark matter, but even if they contain dark matter or are impeded in a dark matter halo, the effects of it are very small and the amount is negligible. This conclusion follows from examinations of the mass-luminosity ratio. This reveals a big difference in the presence of dark matter between elliptical galaxies and GCs. (Kamann et al. 2016)
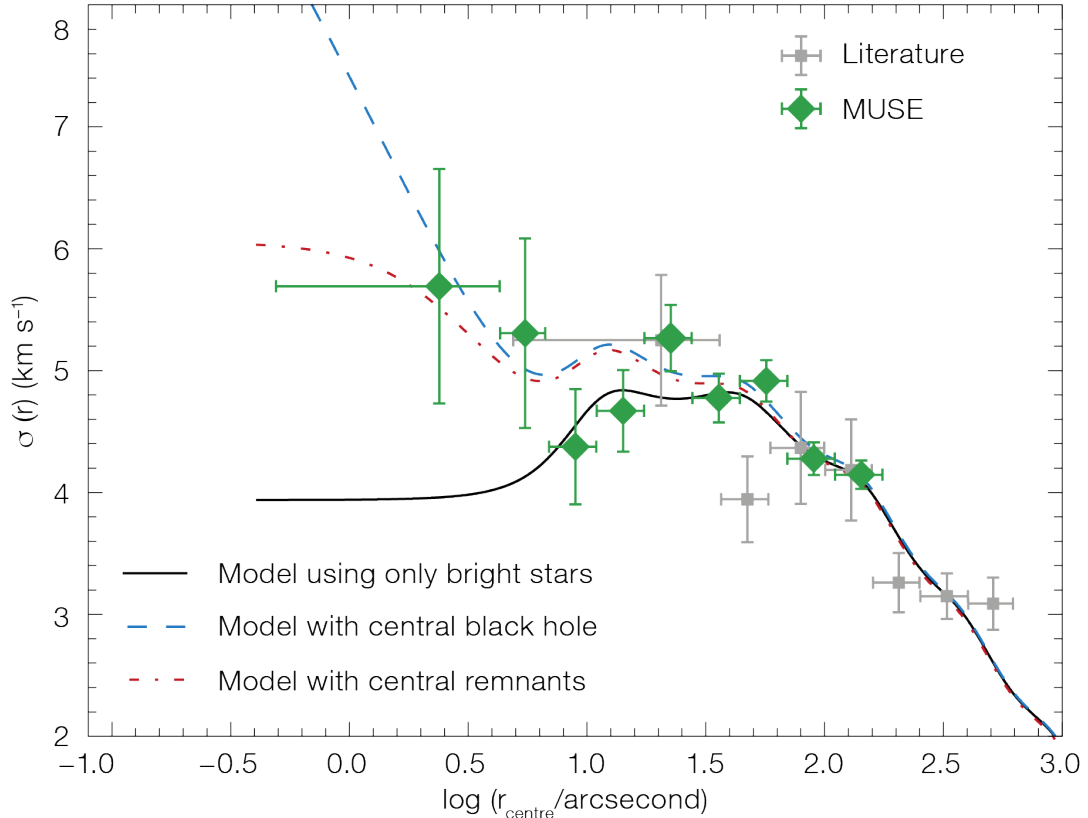
Figure 1.6: Velocity dispersion vs. distance from the center, different models can explain the observed dynamics in NGC 6397 (Kamann et al. 2016)

1.5.3 Binaries in globular clusters

In the field about half of all stars exist in binary systems or even higher order systems. This, of course, influences the evolution of the companion in the system. Since the fraction of binaries is rather high in the field, the influence of binaries on stellar evolution is an important aspect. Binaries are far more affected by dynamical encounters than

single stars. In GCs, the densities of stars are much higher than in the field, meaning that the influence binaries have on cluster dynamics and evolution would be rather strong. In dense regions binaries would be destroyed more often, but on the other hand it is also easier to form a binary. The presence of binaries has a strong influence on the dynamical evolution of GCs. Through the destruction of binaries, also referred to as binary burning, the cluster can be prevented from collapsing while maintaining a constant stellar density and velocity dispersion, or a collapse can come to a halt. The current and initial fraction of binaries is therefore an important parameter to consider for the evolution of clusters. It is necessary to distinguish between wide and close binaries. The wide ones are fairly easy to break up. Thus wide binaries in GCs would be ripped apart pretty fast since the stellar density is so high. Close ones are harder to break up. The breakup of close binaries is also thought to be an important source of energy to prevent the collapse of the cluster, but the close binaries could also be hardend through dynamical interactions. Since binaries are not that easy to observe, simulations were used at first to make predictions about binaries in GCs. Regardless of the models used, the result was that the fraction decreases with the age of the cluster. The current fraction, according to those results, are far below the fraction in the field, even if an initial binary fraction of 100% was assumed. Therefore the models predicted binaries to be less common in GCs. In recent years, these predictions were confirmed by actual observations. Additionally, it was found that the fraction decreases with age as can be seen in Fig. 1.7. Some clusters show binary fractions of about 30%, but the typical fraction in GCs is about 7%, this shows that the fraction of binaries is much lower in clusters. (Ivanova et al. 2005; Ji and Bregman 2015)
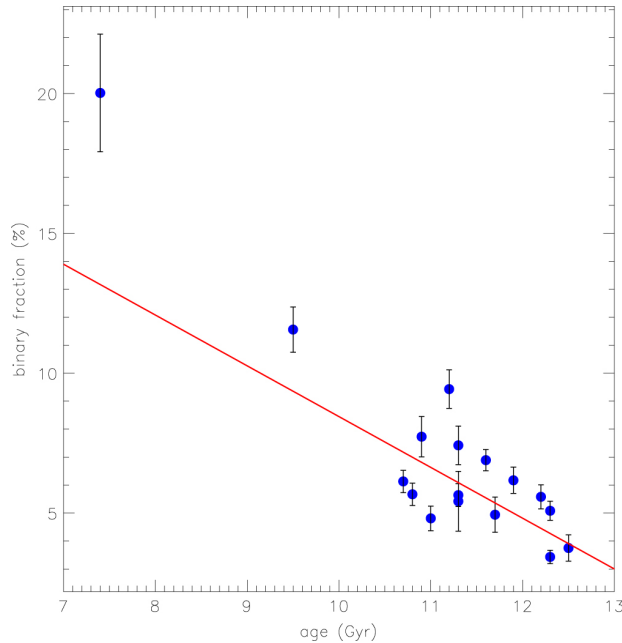
Figure 1.7: Decrease of binary-fraction with time (Ji and Bregman 2015)

1.6 The horizontal branch

1.6.1 Parts of the horizontal branch

The horizontal branch can be divided into different parts. The classic convention only distinguishes between the red and blue horizontal branch, with those two parts being on opposite sites of the RR-Lyrae instability strip. However, this separation is not very detailed. More than these two groups have to be distinguished.

Different gaps and jumps in the CMD separate the groups. The Newell gap 1 or jump 1, often also referred to as Grundahl jump (Grundahl et al. 1998), is located between the RR-Lyrae strip and the BHB. The blue horizontal branch stars have lower temperatures of about 11,500 K and stretches up to about 20,000 K, where the Newell gap 2 is located (also known as Momany jump (Momany et al. 2002)). Stars bluer than the Newell gap 2 are part of the EHB. A third gap, the blue-hook gap, lays between the extreme horizontal branch and the blue-hook. Blue-hook stars are bluer than the extreme horizontal branch, this gap corresponds to temperatures around 35,000 K.

Not all globular clusters show all these groups. Figure 1.8 shows an optical CMD of the GC NGC 2808 and the location of the gaps and jumps in the horizontal branch. This CMD is constructed from the magnitudes observed in different HST filters [2]. The number in the filter name (e.g. F 814 W) is the central wavelength of the filter in nm, the W at the end of the name stands for wide. In the following the catalog by Sarajedini et al. (2010) is used for all the CMDs, this catalog lists the magnitudes for the filters F606W and F814W, so for these CMDs redder colors are used.

However, if UV-fluxes are combined with optical ones the gaps and jumps are more obvious (see Fig. 1.9). The upper panel of Fig. 1.9 shows the HB of NGC 2808 with all the gaps and jumps, with the color combination ($C_{F275W,F336W,F438W} = (m_{F275W} - m_{F336W}) - (m_{F336W} - m_{F438W})$) used, here the groups are even more separated. The lower panel shows the full CMD, also here the different groups can be distinguished from each other.

Depending on the colors used the jumps are stronger or weaker. Brown et al. (2016) suggested that all HBs of GCs follow this scheme (Newell and Graham 1976; Brown et al. 2016; Heber 2016).

---

[2] http://www.stsci.edu/hst/wfc3/ins_performance/ground/components/filters
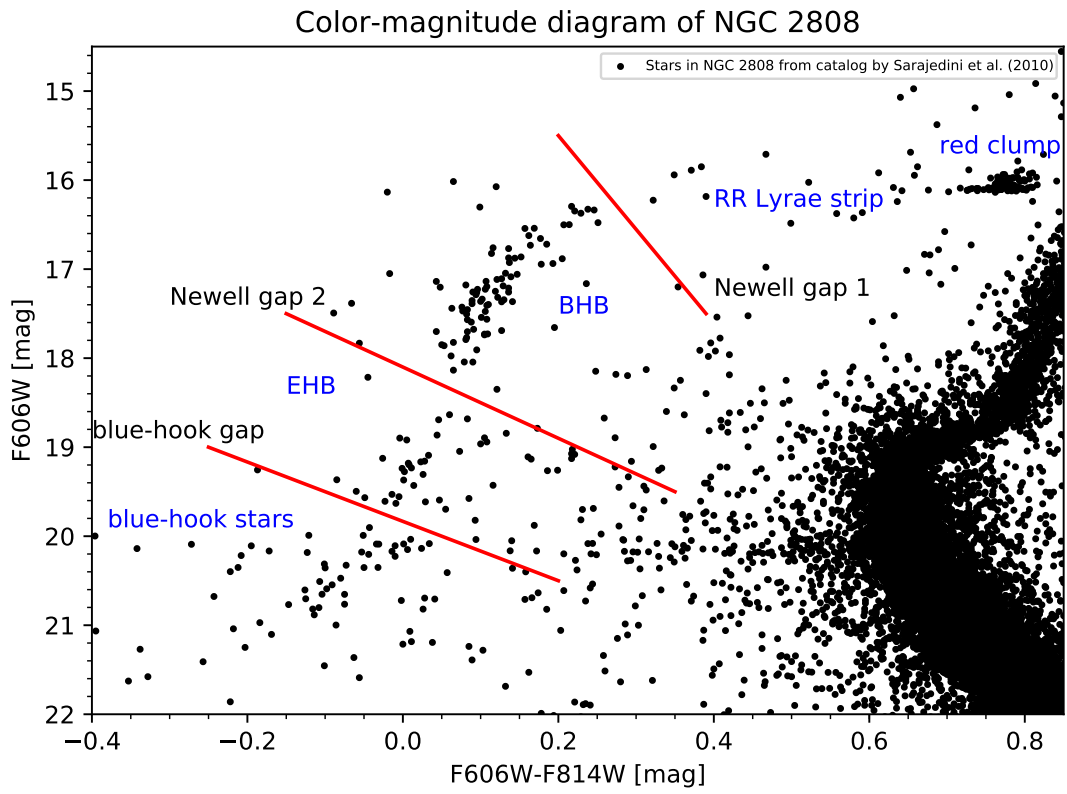
Figure 1.8: CMD of NGC 2808 showing the different gaps and jumps
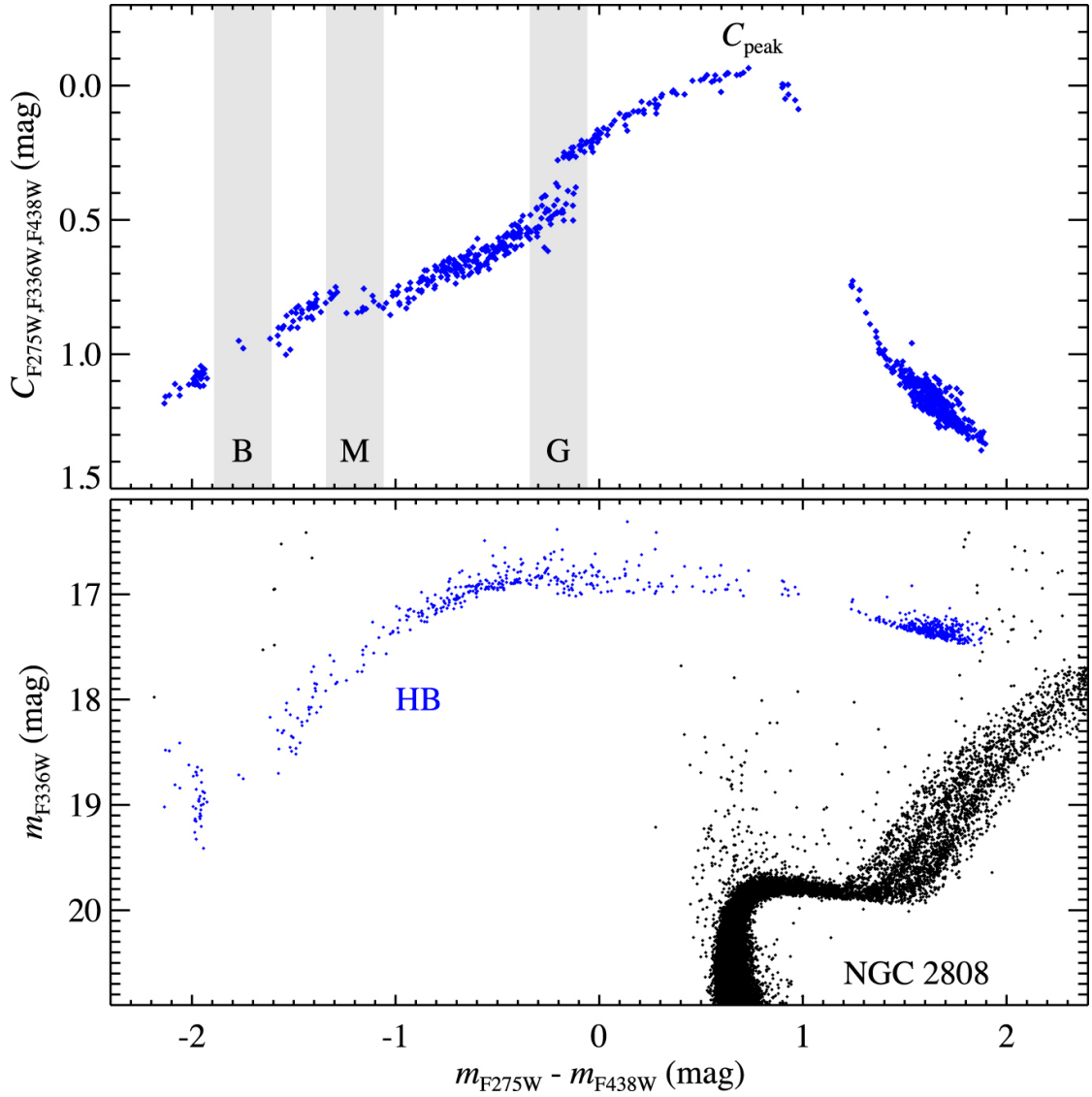
Figure 1.9: CMD with UV/optical-colors of NGC 2808 showing the different gaps and jumps (G: Grundahl jump, M: Momany gap, B: blue-hook gap) (Brown et al. 2016)

1.6.2 Horizontal-branch morphology

The morphology of the HB, and especially of the extreme horizontal branch (EHB), differs from cluster to cluster. Since not all GCs have BHBs, EHBs, and blue-hook stars it is important to know which parameters influence the morphology of the HB.

The most obvious parameter to influence the morphology is the metallicity [3]. Clusters with different metallicities display quite different morphologies. The metal-poor clusters show very blue HBs and, in contrast, the metal-rich clusters have redder HBs. The GC 47 Tuc for example has a higher metallicity (-0.72 dex) than the cluster M 92 (-2.31 dex)[4]. The morphology of their HBs is very different, as can be seen in Fig. 1.10. As expected the HB of M 92 is extended more to the blue than the HB of 47 Tuc, which only consist of the red clump and no parts towards the blue. (Harris 1996)
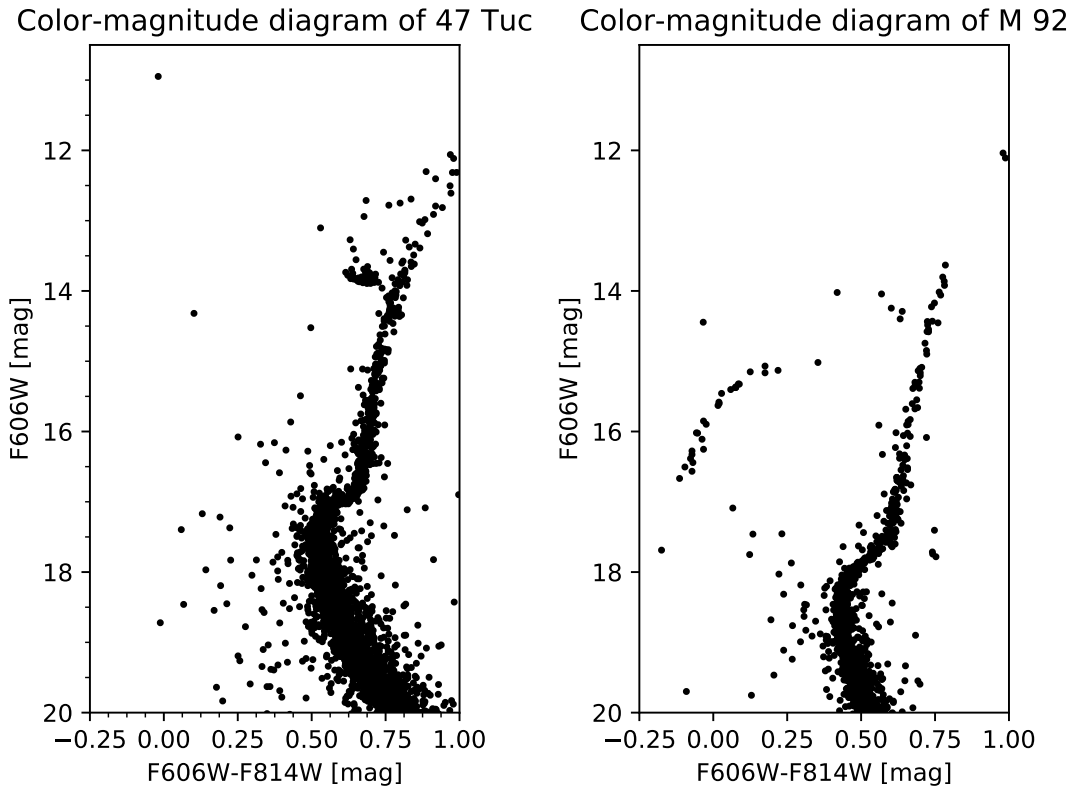
Figure 1.10: CMD of 47 Tuc and M 92, which have different metallicities. The CMDs were made using the catalog of Sarajedini et al. (2010)

---

[3]The iron-to-hydrogen ratio is often used as a proxy to the metalicity. It is usally given with respect to solar: $[Fe/H]=\log(Fe/H)-\log(Fe/H)_\odot$.

[4]http://physwww.mcmaster.ca/~harris/mwgc.dat

However, as one would expect, the metallicity can not be the only parameter influencing the HB morphology. This becomes obvious because some clusters with the same metallicity do not have a similar HB morphology. For example, the GCs M 13 and M 3 have about the same metallicity (-1.50 dex) (Harris 1996) but still very different HBs, as can be seen in Fig. 1.11. At least a second parameter is required to explain this phenomenon, and probably even more than just two parameters influence the morphology.
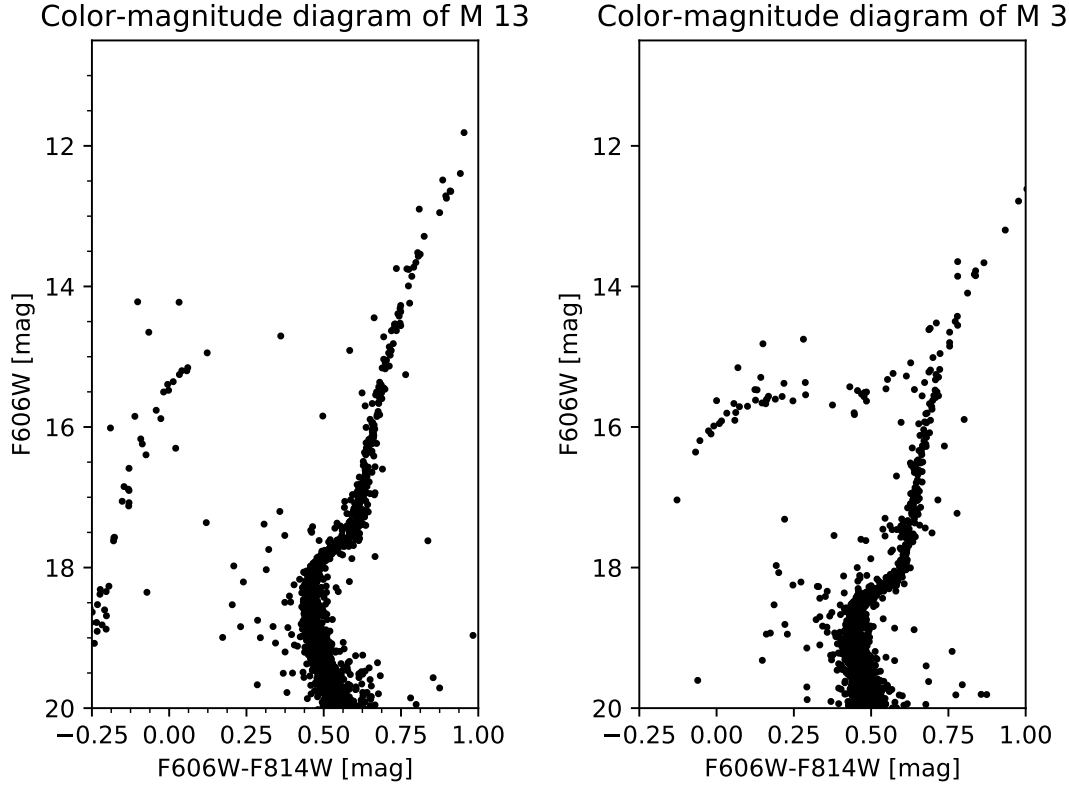
Figure 1.11: CMD of M 13 and M 3, which have the same metallicities. The CMDs were made using the catalog of Sarajedini et al. (2010)

For a long time, the age of GCs was favored as the second parameter but the results are not conclusive. Some clusters with the same metallicity show different morphologies and are assumed to have different ages, but some studies show that clusters with the same metallicity and a similar age also display differences in the morphology of their HBs. Additionally, the uncertainties on the age are quite large, so often it can not be excluded that the clusters actually are of the same age.

Another promising parameter is the helium content. Many clusters, such as for example ω Cen, show different stellar populations that can be distinguished as multiple sequences on the MS and the RGB. This could be explained by multiple episodes of star formation

and the pollution of younger stars by the older population. However, it is not very easy to investigate this issue since it is not always possible to directly observe helium lines in stellar spectra, but simulations which assume different subpopulations with different helium content, succeed to explain the observed morphologies for some clusters. The results for NCG 2808 are shown in Fig. 1.12. In this example, the stars with the highest helium content end up at bluer colors. This makes the helium content a good candidate for the second parameter.

However the list of other potential parameters is long and includes candidates such as core density, helium mixing or the presence of planets. Future research will hopefully shed light on this issue (Heber 2016).
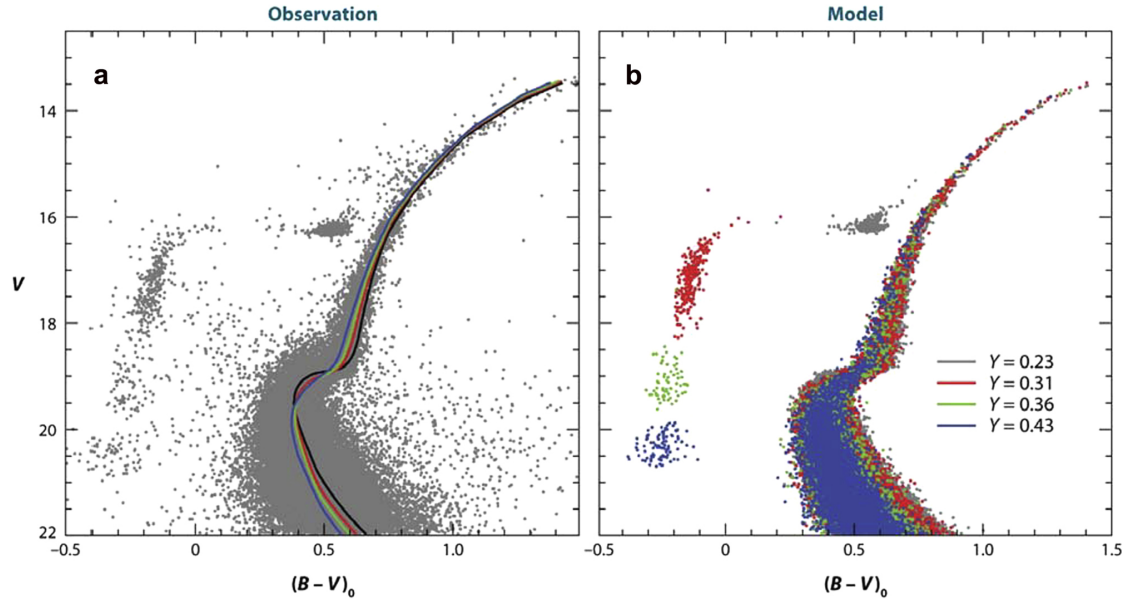
Figure 1.12: Simulation of different subpopulations in GCs in the CMD. Different colors show different helium contents. The observed CMD of NGC 2808 is shown in panel a) and b) shows the simulation (Heber 2016)

2

Hot subluminous stars and blue horizontal branch stars

Hot subluminous stars are found among spectral types O and B. They are also called hot subdwarf O/B-type stars and represent late stages of stellar evolution. The first discovery of such a star dates back to the 1950s. The sample, however, remained small for a long time but from the 1980s on the number of known stars of this type increased significantly, thanks to the modern surveys conducted since then. Still, many questions arise concerning the formation and evolution of these stars. In this section, a brief overview on hot sub-luminous stars and blue horizontal branch stars will be given, starting with their spectral classification followed by an examination of their chemical and atmospheric properties as well as their formation and evolution. The chapter will be concluded by an overview on these stars in GCs and is mainly based on the review from Heber (2016).

2.1 Spectral classification

The RR-Lyrae gap separates the HB in a blue and a red part. The stars at the blue end of the RR-Lyrae are the blue-horizontal branch stars, they can be found below the main-sequence and above the white-dwarf sequence in the Hertzsprung-Russel diagram. They are considered "normal" horizontal branch stars. The blue-horizontal branch connects the extreme-horizontal branch with the giant sequence (see Fig. 2.1). These stars are referred to as extreme-horizontal branch stars since they form a blue-extension of the horizontal branch in the color-magnitude diagram. In the Hertzsprung-Russel diagram they can be found at high temperatures, corresponding to spectral types O and B and at luminosities higher than solar. Hot subluminous stars, meaning they are less luminous than MS stars of similar color, can be found in two spectral types, sdO and sdB. A transition type, sdOB, is also often used in literature. Since they are less luminous than MS stars they are referred to as subdwarfs, which also explains the abbreviation sd. They represent late stages of stellar evolution.

Most HB stars are helium-core burning stars which have evolved away form the giant sequence. In contrast to BHB stars, which have a hydrogen shell massive enough to sustain hydrogen-shell burning, sdBs and sdOs for example, do not have a hydrogen shell massive enough to sustain hydrogen-shell burning.
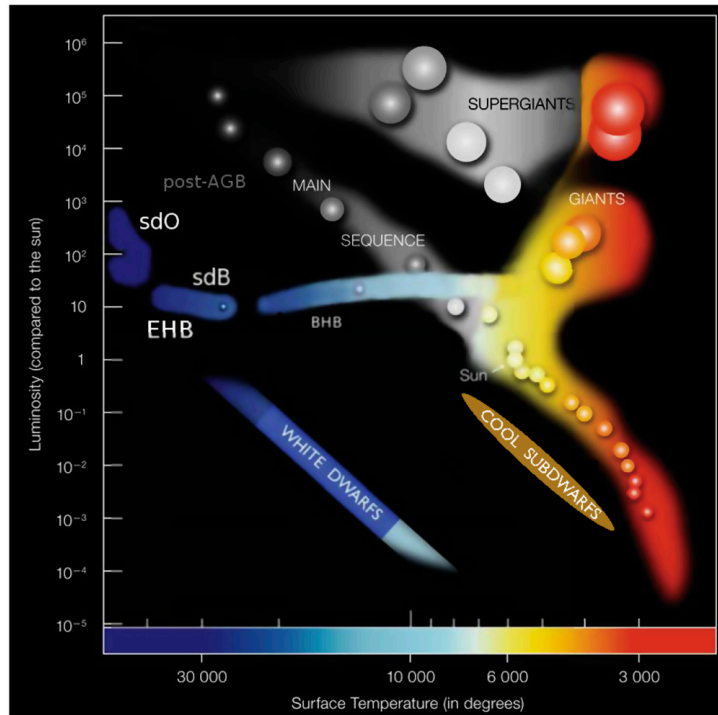
Figure 2.1: Hertzsprung-Russel diagram showing the position of subdwarfs (Heber 2016)

2.2 Atmospheric and chemical properties

2.2.1 Spectral types

The scheme classification of subdwarfs is complex, since it does not fit the MK-classification so it is necessary to introduce another dimension to the scheme to make a classification possible. The more common spectral classification, however, is strongly simplified and distinguishes between O and B type stars among subdwarfs. With increasing T_{eff} , the spectral types go as follows: BHB, sdB, sdOB and sdO. Since some of these stars are helium enhanced and thus show strong helium lines, these stars are separated into the following spectral classes: He-sdB and He-sdO. In general, all stars show Balmer lines, but with increasing temperatures the lines become less prominent, additionally the BHB stars also show Paschen lines. The cooler ones, BHB and sdBs, may show lines from neutral helium (HeI), but at higher temperatures, beginning with sdOBs, the stars may start to show lines from singly ionised helium (HeII). The HeII lines become stronger than the HeI lines at higher temperatures. Figure 2.2 shows example spectra of different types of HB stars. This classification, however, is not very strict. Often different groups in the scheme are fussed together or the terms are used differently in some studies. (Stroeer et al. 2007; Drilling et al. 2013)
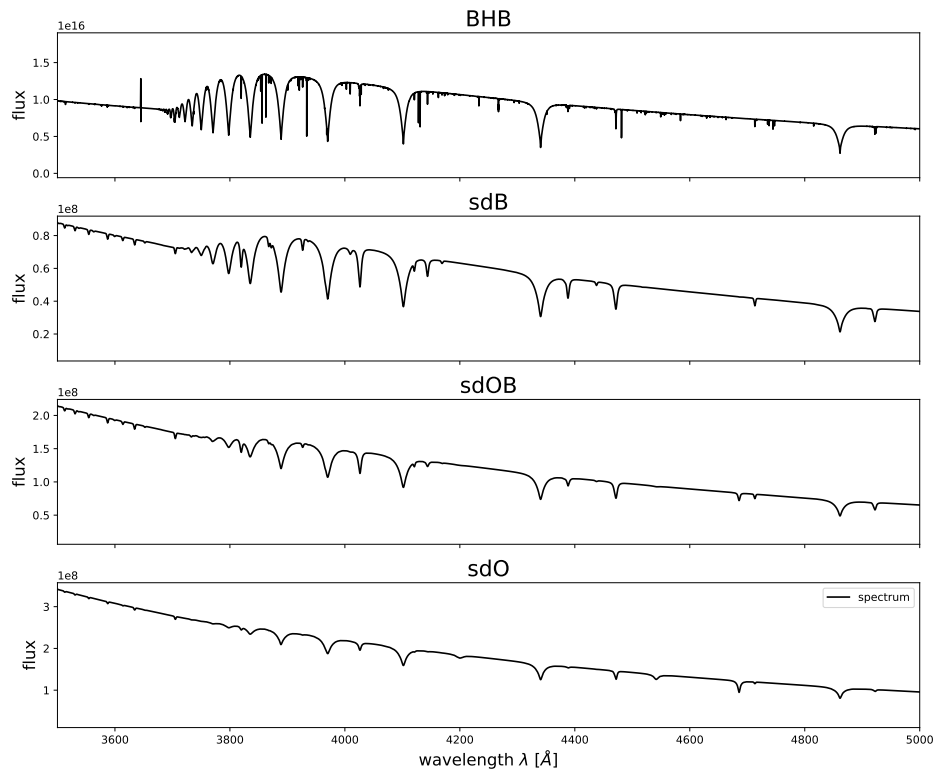
Figure 2.2: Comparison of different spectral types (synthetic spectra used)

2.2.2 Atmospheric properties

The atmosphere of a hot subdwarf is mainly characterized by three parameters: the effective temperature of the surface (T_{eff}), the surface gravity (log g), and the helium abundance often expressed as $\log \frac{\text{N(He)}}{\text{N(H)}}$. These parameters can be derived by comparing synthetic spectra to the observed ones. The observed spectra are fitted with a grid of synthetic spectra calculated from model atmospheres in order to derive these parameters. Different analyzed samples of hot subdwarfs may show some systematic differences depending on how the stars in the sample were selected and which model atmospheres were used to analyze them. Two very important diagrams are the T_{eff}-log g and T_{eff}-helium abundance diagrams, Fig. 2.3 shows these two diagrams for hot subdwarfs, BHB stars are colder than the range covered in this diagrams. Most samples find the subdwarfs to be in a temperature range between 20,000 and 60,000 K and the surface gravity to be between 5 dex and 6.4 dex. A slight increase of surface gravity with temperature can be seen. The helium abundance of sdBs seems to increase with surface temperature. This increase occurs in two different groups of sdBs, with the minority of sdBs having even lower abundances. O-type or OB-type stars, however, have a huge variety of helium abundances, ranging from almost no to almost complete helium in the atmosphere, with 2/3 of the sdOs being helium-rich. Some sdOs, especially He-sdOs, show very high helium abundances. The helium-to-hydrogen ratio can vary from about -4 dex up to 3 dex, which is a very large range. In both diagrams, a clear gap between helium-rich and helium-poor sdOs can be seen. In general, spectral analyses of He-sdOs suffer from larger uncertainties than other subdwarfs.
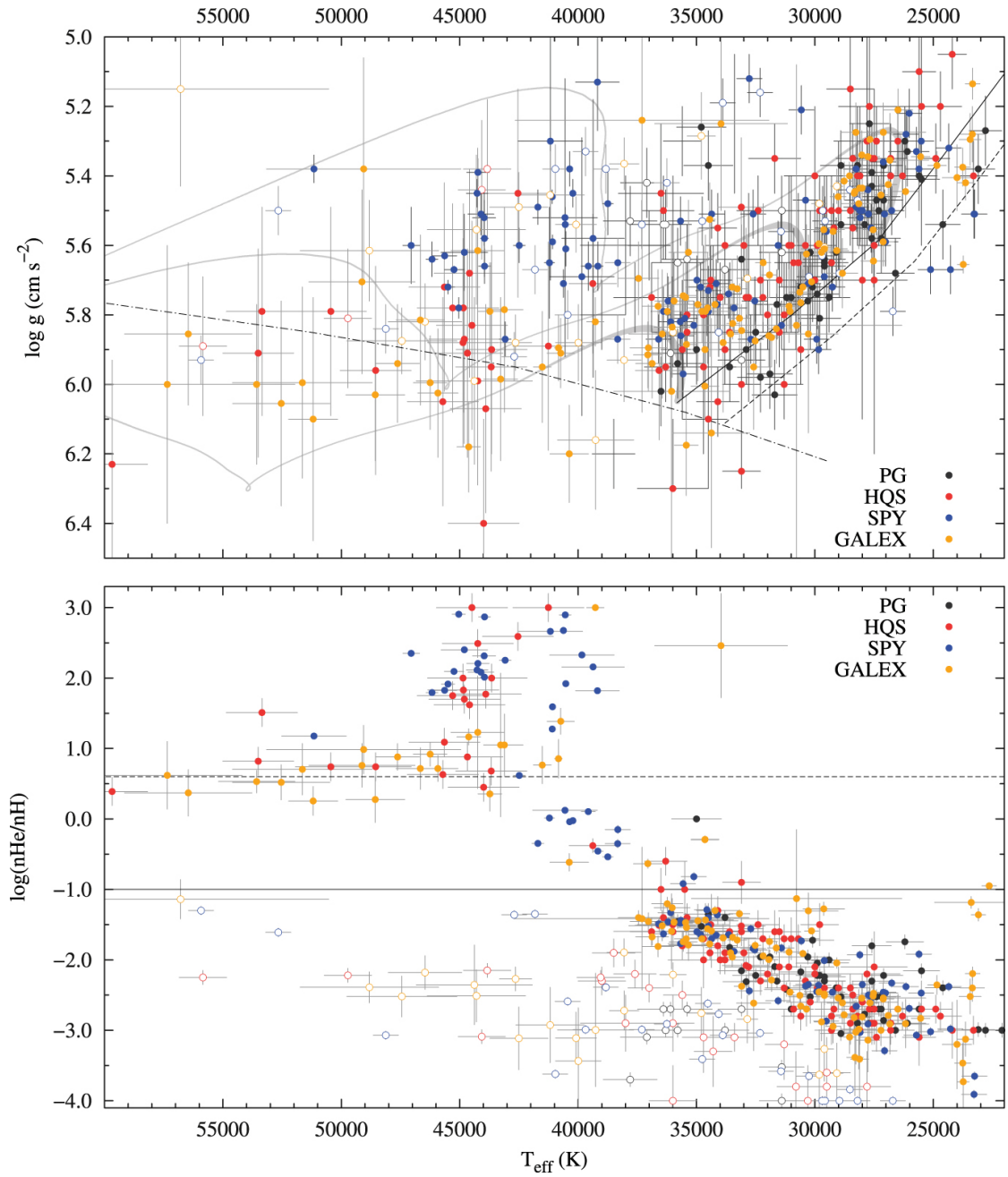
Figure 2.3: Distribution of hot subdwarfs from different samples. Upper panel: T_{eff} -log g diagram, Lower panel: helium abundance vs. T_{eff} (Heber 2016)

2.2.3 Chemical composition

In order to further explore the chemical composition of hot subluminous stars, it is necessary to investigate different spectral ranges, because different ranges display different elements. High resolution optical spectra can be suited to study the abundances of elements such as carbon, magnesium, nitrogen, silicon, sulfur and iron, since these elements can show features in the optical. To detect other elements, however, ultraviolet-spectra have to be used since this range gives access to iron-group and trans-iron-elements. Because abundances of sdBs and sdOs differ from each other they will be discussed separately. BHB stars usually show very few lines of elements other than hydrogen and helium. The abundances are peculiar for all the different types, meaning they are very different from the solar abundance pattern. The abundances varies from star-to-star and are determined by diffusion, however, general trends can be seen.

sdBs are, as already mentioned, divided into two groups with the majority of these stars being helium-poor. The group of helium-rich ones can be subdivided into intermediate and extremely rich ones. The intermediate ones are thought to be transition objects, linking the He-poor sdB stars with the He-rich sdO stars. The sample of stars examined show large star-to-star variations, but some similarities can be found. For all elements heavier than helium, no correlation between abundance and temperature can be found. Due to limits of the analysis many abundances have to be considered as upper or lower limits. The chemical composition of sdB stars is driven by atmospheric diffusion. Effects such as radiative levitation and gravitational settling also influence the chemical composition. Heavier elements have peculiar abundances, for example Nitrogen is sub solar in most stars and the scatter is rather small. Carbon, on the other hand has a much larger spread. The abundance of carbon varies from strongly sub solar to super solar. Links between the helium abundance and other elements can be found.

Little is known about the chemical composition of subluminous O stars, but they can be divided into two groups, helium-poor and helium-rich. The star-to-star scatter of different elements is similar to the one observed amongst the sdBs. Light elements such as carbon are mostly sub solar in helium-poor sdOs, but they can also be heavily depleted.

2.3 Formation and Evolution

In order to explain all the different characteristics shown by hot subdwarfs, a high number of different formation scenarios must be invoked. One of the biggest challenges is to explain the large mass loss required for the formation of EHB stars. There are different theories explaining EHB stars through various processes at the end or after the RGB. Besides, single-star evolution, binary-evolution scenarios are also important since a large fraction of subdwarfs are found in binary systems among the field population. BHB stars are explained by normal evolution following the RGB phase, therefore similar processes apply for those, which is considered a canonical evolution.

Canonical models. Canonical models have been used to explain BHB stars, but are also considered valid for EHB stars if excessive mass-loss occurs. The star starts its helium-core burning as it leaves the RGB. This leads up to the helium-core flash. The distribution of stars along the HB is explained by mass variations of the hydrogen envelope, with the stars undergoing less mass loss ending up as BHB and the ones with a higher mass loss as EHB stars. After helium is exhausted in the core the star evolves towards higher temperatures and higher luminosities moving towards the WD graveyard. Still canonical models can not explain the formation since these models assume ad-hoc mass loss but lack a physical mechanism.

Hot-flasher scenario. Normally the helium flash occurs at the tip of the RGB (Panel (a) of Fig. 2.4), but it is possible that a star leaves the RGB and then undergoes a helium flash. Panels (b) and (c) of Fig. 2.4 show this behavior; in panel (b) the flash occurs relatively close to the RGB, while in panel (c) the flash happens after the star evolved away from the RGB. Panel (d) displays an even later flash. For a delayed flash to happen, though, the star must undergo a significant mass loss on the RGB. The He-enrichment is explained by the convection zone produced by the helium flash. This causes hydrogen from the envelope to be mixed into the core of the star. The properties of the star afterwards are influenced by the phase during which the flash happens. In the early hot-flasher scenario, the flash occurs shortly after the departure from the RGB, resulting in a standard hydrogen-rich subdwarf. The flash can happen latter on the WD-cooling curve. Depending on the position on this curve at which the flash happens, the mixing occurs at different depths. If the flash occurs early on the WD-track the mixing is shallow and because of convection the atmosphere is enriched with helium and nitrogen. If deep mixing occurs, the hydrogen is burned because of the convection caused by the flash, which brings helium and He-burning products (mostly carbon) to the surface. If the flash happens even later than in panel (d), the stars will also enter the HB phase, but the models are not able to compute this, but it is also possible that a star never undergoes a helium-flash, in which both cases it dies as a helium-WD (panels (e) and (f)). The hot-flasher scenario is basically the extension of the canonical models.

Helium mixing. The helium mixing occurs on the RGB. The convection zone is able to penetrate the hydrogen-burning shell, causing helium to be transfered into the envelope of the star. Calculations were made for different penetration depths, which of course influences how strong the mixing is. The mixing causes the tip of the RGB to have a higher luminosity than in the regular case. The higher luminosity will cause an enhanced

mass loss. (Brown et al. 2001; Bono 2010)
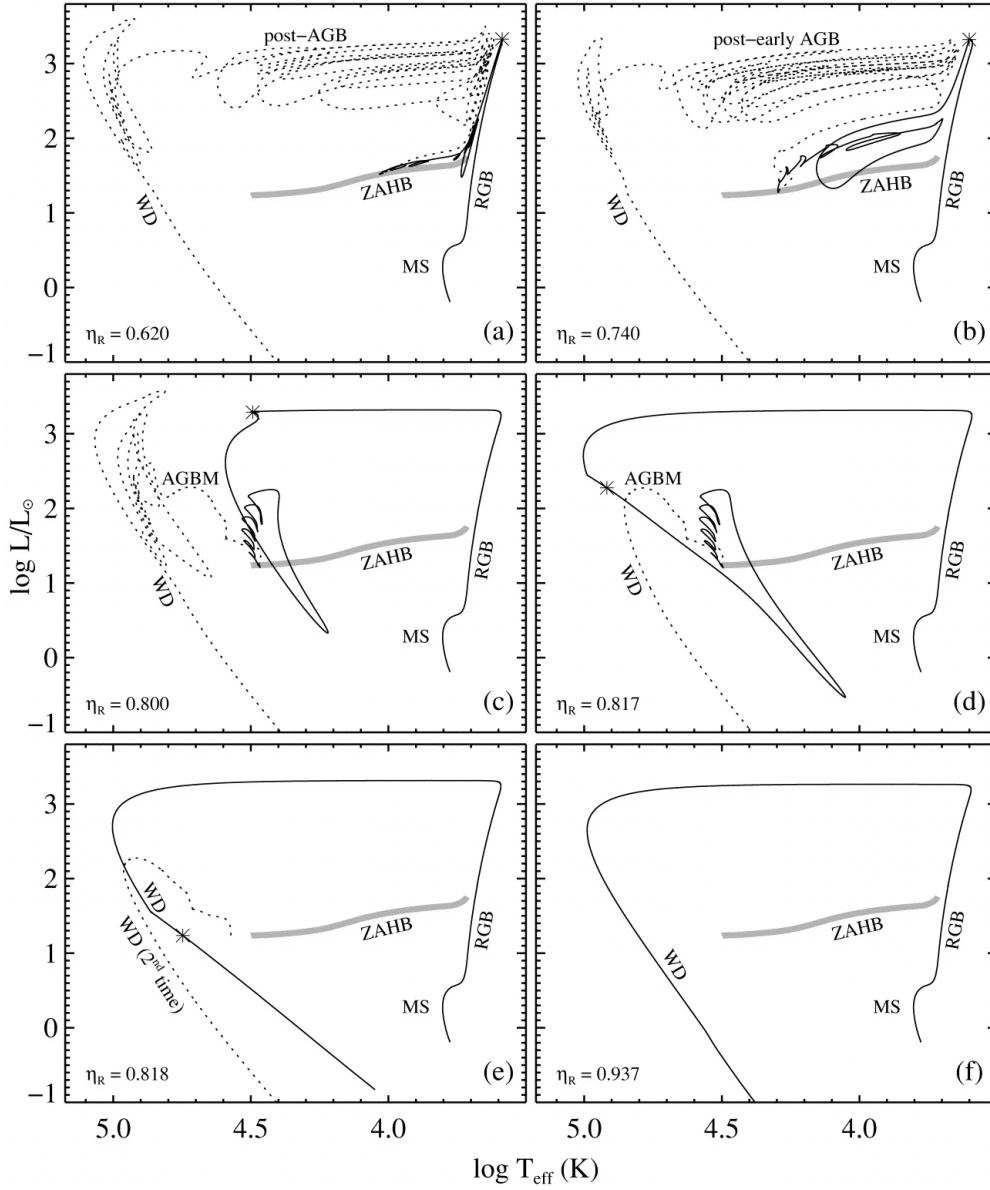
Figure 2.4: Different evolutionary tracks, the star marks the position at which the helium-flash occurs, the full drawn line shows the evolution from the MS to the HB, the dashed line shows the evolution after the HB phase. The difference between the panels is the Reimer factor for mass loss efficiency η_R, this factor is increased from panels a to f. ZAHB= zero-age horizontal branch, AGBM=AGB manque (Brown et al. 2001)

Close-binary evolution. Models involving the evolution through close binary systems can be divided into three groups. In the first scenario, the formation of the EHB star takes place via a common-envelope phase (CE). The primary fills its Roche lobe, but if the companion is significantly less massive than the primary the mass-transfer is way too high for the companion to accrete the mass. This leads to the formation of a common envelope. In this envelope the stars will spiral towards each other, transferring energy to the envelope due to friction. If the energy is high enough, the envelope will be ejected leaving behind a subdwarf and his previous companion. If the primary and secondary masses are almost equal the mass transfer happens at rates that make it possible for the companion to accrete the mass in a stable process without forming a common envelope. In this process, the entire envelope of the primary is transfered to its companion, leaving behind a subdwarf, this scenario is the stable Roche-lobe overflow (RLOF) channel. After this phase a common envelope phase can occur. If both stars are in the giant phase, a so called double-core common envelope evolution could happen. After the common envelope is ejected, two subdwarfs can stay behind. These scenarios are also depicted in Fig. 2.5. The merger of two helium-WD could also produce a subdwarfs. In this case, the two WDs in the binary will be brought closer to each other and in the end, either through RLOF and disk formation or direct mass transfer, or a combination of both, a subdwarf is formed.
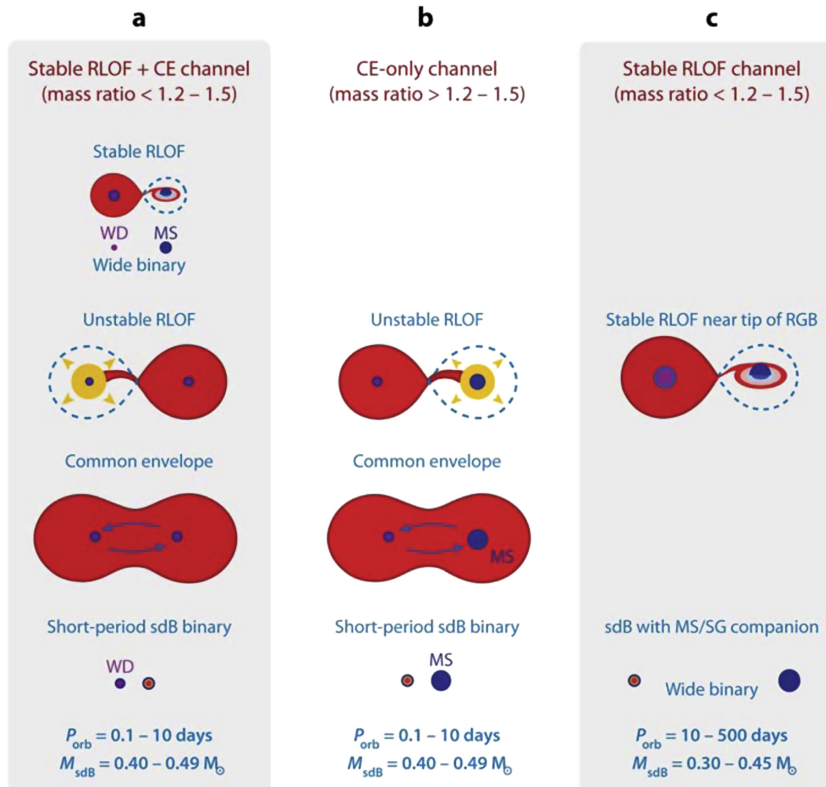
Figure 2.5: CE and RLOF formation of subdwarfs (Heber 2016)

2.4 Hot subdwarfs and BHB stars in globular clusters

Hot subdwarf stars are found only in some GCs, which show very blue horizontal branches, e. g. NGC 6752, NGC 2808 and ω Cen. In this section the differences between the field and GC population of EHB stars will be discussed.

2.4.1 Atmospheric parameters and chemical composition

The field population of EHB stars and the GC population of EHB stars are different in their atmospheric parameters. This of course means that the distribution of the stars in the log g-$T_{\rm eff}$ diagram and log He/H-$T_{\rm eff}$ diagram is different. These differences can be seen in Fig. 2.6. The cooler EHB stars ($T_{\rm eff}$ <35,000 K) in GC are found between the ZAHB (zero age horizontal branch) and the TAHB (terminal age horizontal branch), indicating that these stars are normal helium-core burning stars. This group is also be found in the field. The stars in GCs on the HB band are found at higher surface gravities. The hydrogen-rich stars found at high temperatures and not located within the HB band can be interpreted as post-EHB stars. The He-rich objects in the field cluster around 45,000 K and are not located on the HB band. In GCs however, these objects are found at cooler temperatures than in the field, and they mostly fall within the HB band. There also is a difference in the He-abundance between the field and GCs. In GCs, the He-enhancement is not as strong as in the field, meaning the very helium-rich sdOs are lacking in GCs. The differences in the helium abundance might be explained by the fact that the enrichment in GC is lower than in the field, because the progenitors in GCs are older and more metal-poor than in the field. The relation between temperature and helium abundance is seen in both populations, but it is steeper in the GC population. Not all GCs show HB stars at higher temperatures. In clusters such as NGC 6752, the HB stars end at lower temperatures ($\sim$35,000 K). To the contrary, clusters such as M 54 and NGC 2808 also have hotter stars, which are identified as blue-hook stars. The chemical composition of EHB stars is not that easy to derive. Abundance patterns of GC HB stars are quite similar to those of field stars, hinting that the same processes could be responsible for the surface abundance in the field and in clusters. Diffusion could explain why HB stars in GCs show weaker He-lines. The radiative acceleration of elements is stronger than gravity, pushing elements towards the surface. Turbulence, however, may reduce this effect. Stars below 12,000 K mostly show the general abundance pattern of their host cluster, but stars hotter than that show variations from this pattern, indicating that diffusion is temperature dependent. For example, iron can be enriched with respect to solar, while helium is depleted. Some correlations between the abundance of different elements can be found among HB stars in GCs. (Latour et al. 2014; Moehler 2001; Moni Bidin et al. 2008; Behr et al. 1999)
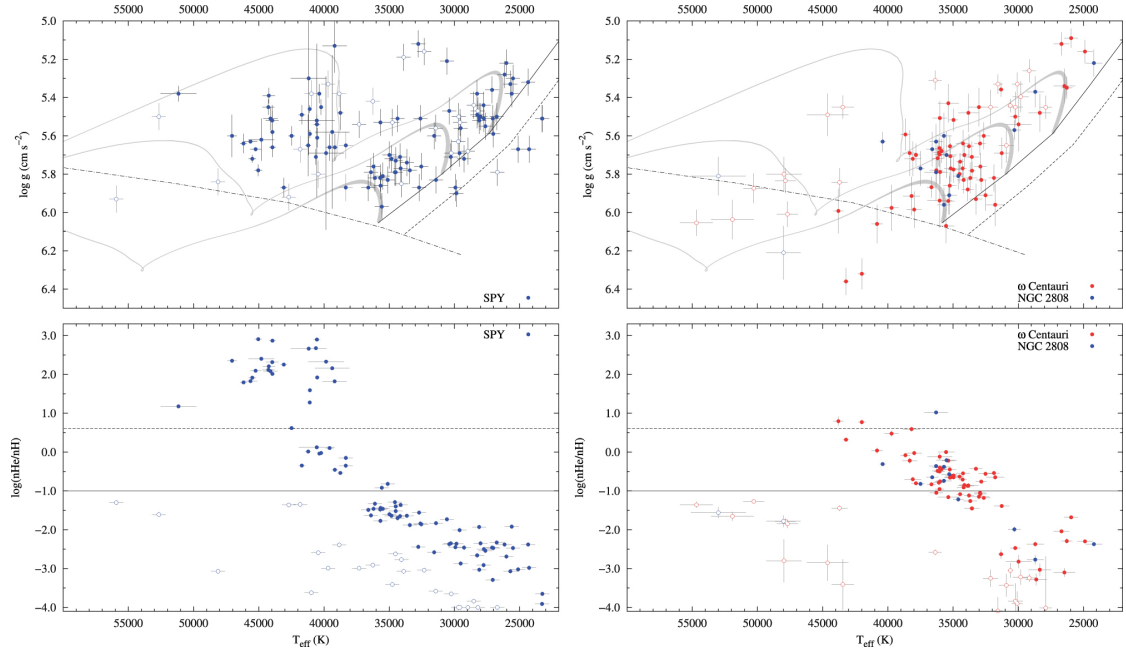
Figure 2.6: Comparison of the atmospheric parameters of EHB stars in the field and in GC. Evolutionary tracks for EHB evolution are shown. The end of core helium burning results in a hook in the respective track. (Heber 2016)

2.4.2 Binarity of HB stars in globular clusters

Another striking difference between the field and GC population of EHB stars is their binary fraction. In the field sdB population, binaries are very common. About 50% of all sdB stars are estimated to reside in close systems. For this reason, binary-formation scenarios are considered to be very viable options for the formation of these stars. The CE-scenario is often thought to be the best option to explain their formation but this is different in GCs. Here the fraction of binaries amongst the EHB is very low (see section 1.5.3). Although quite some effort has been put into finding binary systems, only one of these systems is known to exist and this system is atypical and even lacks field counterparts. The findings point towards a binary fraction among EHB stars in GC as low as 4%, compared to the 50% fraction in the field. This all suggests, that the EHB stars in GCs are very different from the field. No wide binaries are found because they can not be detected. The lack of close binaries, however, is not that easily explained and could be linked to the formation of the stars. Since the interactions in the central region of the GC are stronger and more frequent, and these interactions are often linked to the production of EHB stars, one would expect a gradient in their distribution in the cluster, with more of these stars being in the center region. This distribution, however, is not observed in any GC, which leaves the conclusion that dynamical interactions in GC are not as important as expected for the formation of HB stars in GCs. However, it is worth noting that blue stragglers are also expected to be formed via stellar interactions

and that these stars are actually found more often towards the center of GCs. This, of course, supports the previous assumption (Moni Bidin et al. 2008, 2015).

2.4.3 Evolution and formation in globular clusters

The lack of binary-systems posts challenges to the formation scenarios (see section 2.3) known for EHB stars since multiple scenarios, including the most favored ones, do not seem to be an option for the formation of these stars in GCs. This means that slightly different formation scenarios are required to explain the HB stars.

Helium mixing. Helium mixing is also a possible scenario to explain the HB stars in GCs. Through convection, helium is mixed into the surface layer. This can be accomplished through all kinds of processes, such as fast rotation for example. This option will be discussed separately.

Late Hot-flasher. The late hot-flasher is often favored to explain the formation of HB stars in GCs, because the binary scenarios seem to be less important in GCs. The hot-flasher scenario is able to explain many aspects, but it is not able to explain the formation of EHB stars entirely. For example, this scenario can not reproduce the variety of colors observed among EHB stars.

Helium-enrichment. If the EHB stars observed are part of a second generation of stars, then their formation could be explained by canonical models, assuming that these stars are helium-enriched due to pollution caused by the first generation. Up to now, some GCs are known to host different populations with different helium content, making this scenario a good option to explain the helium-enriched EHB stars.

White-dwarf mergers. According to population synthesis models, the merger scenario would dominate all the other binary scenarios after a time shorter than the age of most GCs. In order for the two helium-white dwarfs to merge it is necessary that the system is hardened over time. This can be accomplished via dynamical interactions, which is possible in the dense environments of GCs, meaning the dynamics of GCs make this a favorable option to explain the formation. Another aspect supporting this scenario is the lack of close binaries in GCs discussed previously.

Mass loss through rapid rotation. The helium enhancement in the atmosphere could also be explained by rapid rotation of the star. Through the rotation, helium could be transported towards the surface. The fast rotation needed for this scenario could be explained by these stars being of the second generation. These stars would form in denser environments than the first generation stars, causing them to lose their disks, which are formed early on during stars formation, which means they can not lose much angular momentum early on. This scenario would require the core to rotate at a constant rate, but asteroseismology, of red giants and pulsating sdB stars suggest that the transfer of angular momentum from the core to the envelope could be more effective than previously assumed, thus challenging this scenario.

Tidally enhanced mass loss. The formation of HB stars requires mass loss, which could be explained by binary interactions. The mass loss can be enhanced by tidal forces in the system. One example for a mass loss process could be stellar winds. These can be tidally enhanced, which could explain the rapid mass loss necessary. This process

could well produce all the HB stars without any other assumptions needed and also the morphology of the HB is well reproduced. However, the number of HB stars predicted is lower than the one observed. (Heber 2016; Z.-X. Lei 2012; Brown et al. 2001, 2012; Moehler et al. 1995)

3

The Program globular clusters: ω Cen and NGC 6752

In this chapter the two GCs observed will be discussed. Each cluster will be introduced separately starting with general information on the individual cluster, followed by a review of the recent work dealing with the HB of these clusters.

The two clusters ω Cen and NGC 6752 were chosen for particular reasons. Both clusters show a large population of HB stars especially on the blue part. ω Cen is the most massive GC, has a very prominent HB, and shows specific features only observed in this particular cluster. NGC 6752 is less massive than ω Cen, but in contrast to similar clusters, it has an especially blue HB, but no blue-hook. In addition both clusters were often observed in the past, since they are amongst the brightest in the sky.

3.1 ω Centauri
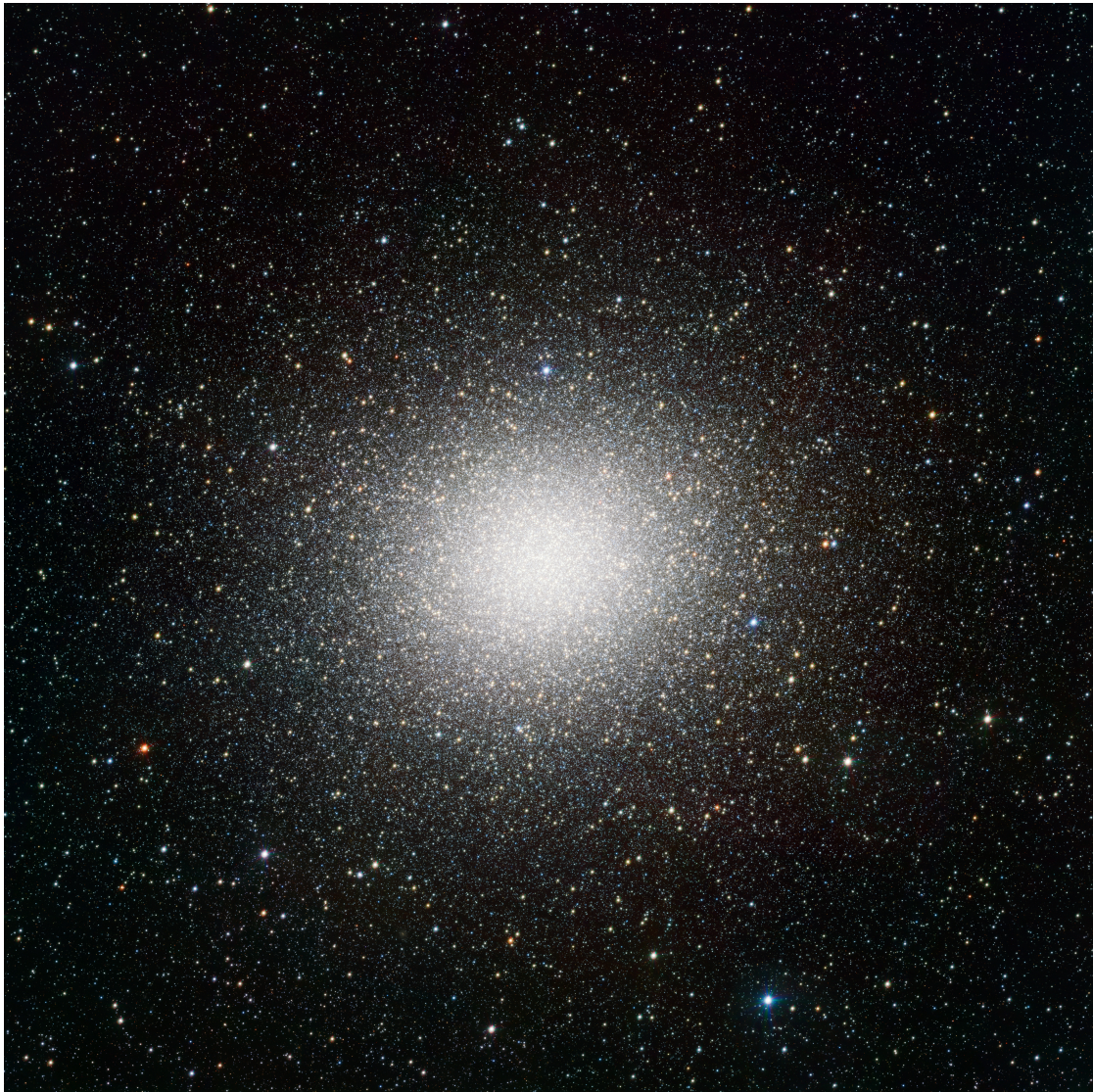
Figure 3.1: Globular cluster ω Cen [1]

---

[1]https://cdn.eso.org/images/publicationjpg/eso1119b.jpg (last accessed: 26.08.2017, 18:45)

ω Cen, or NGC 5139 (Fig. 3.1), is a very special and mysterious globular cluster. It is the most massive GC in our Galaxy, with a mass of $4.05 \pm 0.1 \times 10^6$ M$_\odot$. This GC can be observed in the southern sky in the Centaurus constellation. Although it is a GC and not a star, which was first recognized in 1677 by Hally, it has a Bayer designation for historical reasons. The cluster is located at a distance of about 5.5 ± 0.2 kpc. The estimated diameter of the GC is about 150 ly. In addition to being the most massive cluster, probably consisting of 10 million stars, it is also the largest, but that is not the only property making NGC 5139 a special cluster.

The mean metallicity is -1.35 dex, but ω Cen shows a wide star-to-star spread of metallicity. The abundance variations are larger than in any other GC, also a split MS can be observed, meaning the GC has different subpopulations with different metallicities and helium abundances. At least three different populations are found in ω Cen. This spread is probably related to the mass of the GC. The age of this GC, which is related to the metallicity, is about 11.52 Gyr.

To explain the quite different behavior of ω Cen, many scenarios have been proposed, such as ω Cen being the product of a merger of two GCs or that it is in fact the nucleus of a now dissolved dwarf galaxy. Another scenario suggests that ω Cen is a low mass elliptical dwarf galaxy that underwent self enrichment and was acquired by the Galaxy. The fact that the abundance variations within the GC are very similar to that of spheroidal galaxies and that a wide spread of ages is observed hint at those scenarios. (Gratton et al. 2004; Latour et al. 2014; Moni Bidin et al. 2012; Forbes and Bridges 2010; D'Souza and Rix 2013)

3.1.1 The horizontal branch of ω Cen
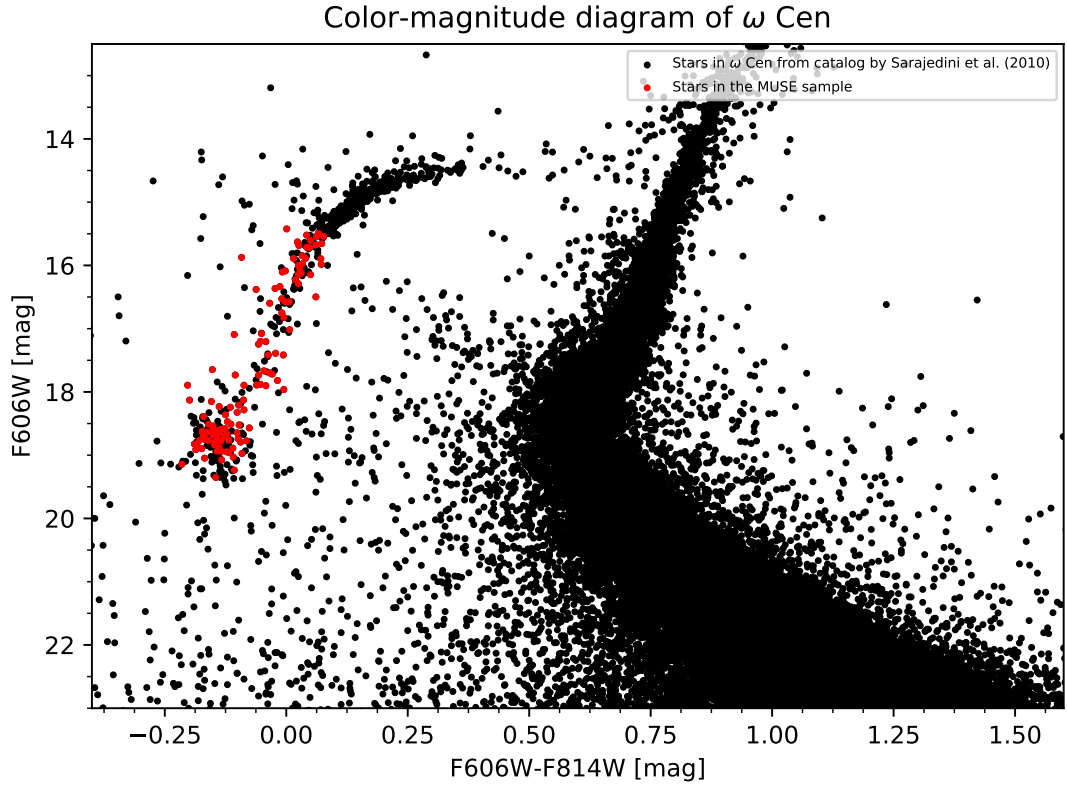
Figure 3.2: CMD of ω Cen

Figure 3.2 shows the CMD of ω Cen. From this CMD it can be seen that ω Cen has a broadened MS and also reveals, with a closer look, variations on the RGB. One interesting part of the CMD is the HB. ω Cen does not just show a horizontal part like many other clusters, but it also has a blue-hook at the blue end of the HB. The blue-hook stars are the most extreme ones on the HB in terms of temperature. The HB of ω Cen is very complex and many observations can not yet be explained. Still ω Cen is one of the most observed GC in our Galaxy, because it is so bright, so in the recent years multiple studies on the HB of this GC have been conducted. For this reason the results of these studies will be shortly reviewed in this section.

3.1.1.1 Spectroscopic analysis of HB stars in ω Cen
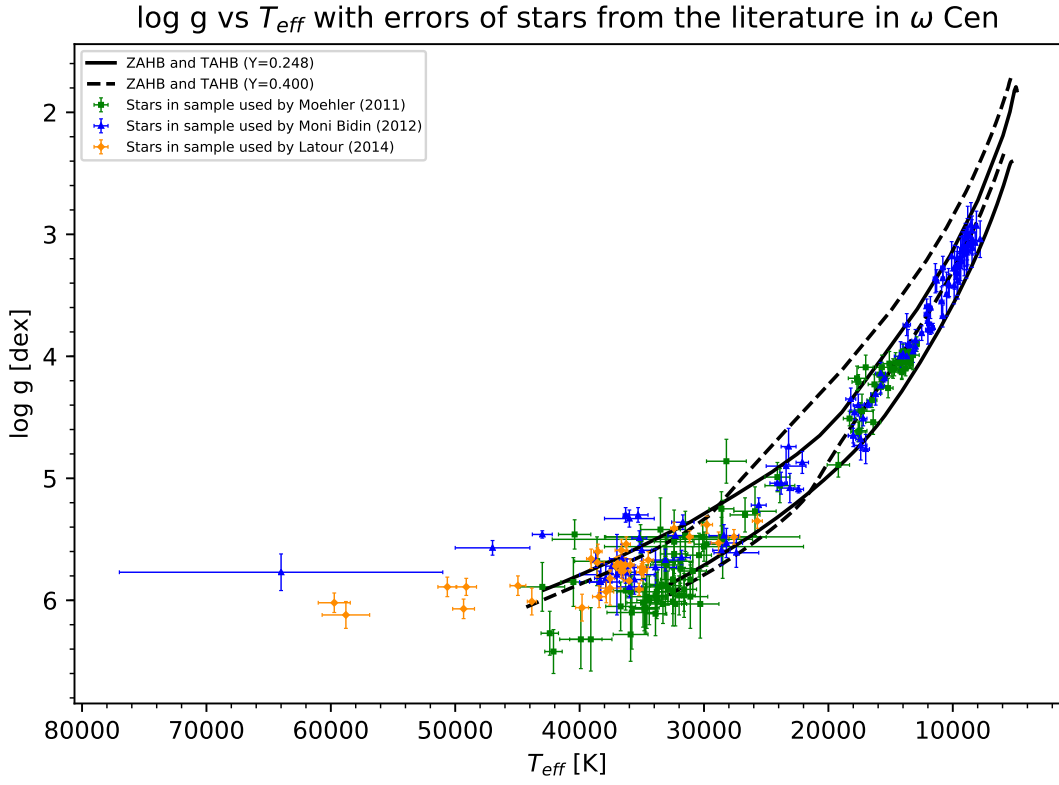
Figure 3.3: T_{eff} -log g diagram containing all the recent results for ω Cen

In 2011, Moehler et al. (2011) conducted a detailed study of 109 BHB, EHB and blue-hook stars. The spectra used had a resolution of R∼ 6400 and were taken in a spectral range from 3964 Å to 4567 Å. The signal-to-noise (S/N) ratio (SNR) of the spectra was not as good as expected, but still sufficient enough for the study. Through cross correlation and fits, the radial velocities were determined in order to confirm a cluster membership, to correct the spectra, and to check for velocity variations between individual spectra, but no binaries were found. The hydrogen and helium lines present the spectra were fitted using a χ^2-method developed by Bergeron and Napiwotzki between 1992 and 1999 with different LTE and non-LTE models. The helium-poor stars show no different behavior than HB stars in other clusters. The helium-rich stars cover a temperature range ranging from the hot end of the ZAHB to a temperature often associated with the hot-flash scenario. Therefore, it was concluded that the hot flasher scenario might be the way to explain the evolution of the He-rich ones. The atmospheric parameters of stars below 20,000 K could hint towards the fact that ω Cen has helium-enriched stars in this temperature range, but the results are not conclusive. Still, the helium-rich stars strongly hint at the hot-flasher scenario, also The higher than expected helium

abundances and the observed carbon abundances support this hypothesis, but it can not be excluded that the observed stars are progeny of a helium-enriched population.

In the study by Moni Bidin et al. (2012, 2011), spectra of 115 HB, EHB and blue-hook stars were obtained using the FORS2 spectrograph at VLT. The targets were chosen from photometric data and were selected to be distributed over the full temperature range of the HB. The range used was between 3450 Å and 5900 Å and the resolution used was about 1600. The spectra all have a SNR over 40. The reduced spectra were fitted to derive the atmospheric parameters. A χ^2-method was used fitting the available hydrogen and helium I and helium II lines. This sample has 11 stars in common with the one from Moehler et al. (2011), so the two samples can be compared with each other. The differences when compared to the results of Moehler et al. (2011) are not that significant and no offset could be detected. The helium abundances found are in good agreement with the results of other GCs. For the cool stars, a relation between helium abundance and temperature can be observed. The helium abundance decreases with temperature reaching a minimum at 15,000 K, and towards higher temperatures the helium abundance again increases. This hints that diffusion-efficiency might be temperature-dependent. The hotter stars show a mild increase in helium abundance up to a temperature of 27,000 K, but for these stars the scatter is much higher. This all hints towards the hypothesis that two families of EHB stars exist that differ in initial helium abundance, but the results are not conclusive, due to observational errors. The EHB stars in the sample can be divided into two groups. One being helium-poor and one exhibiting solar or super solar helium abundances. These results are consistent with previous results, but still the fraction of helium-poor objects is smaller than in other samples. The helium-poor group is consistent with being post-EHB objects evolving towards the WD-cooling sequence. The helium-abundance is assumed to be bimodal, with peaks at -2 dex and -3.2 dex. The gravities of the observed stars do not cluster at the ZAHB for higher temperatures, which is the case for the Moehler et al. (2011) sample. The cooler stars show lower gravities than stars in other GCs, this all could point to intrinsic differences between the HB stars in ω Cen and other GCs.

For the study by Latour et al. (2014) 38 spectra were obtained with the FORS2 spectrograph. The spectral range used was 3400 Å up to 6100 Å using a 2.6 Å resolution. The hydrogen and helium lines in the spectra were fitted with a grid of non-LTE models. The stars can be divided into three groups. Group 1, 7 hydrogen-rich sdBs, is found at lower temperatures. These stars show no metal lines, so their carbon abundance is far below solar level. Group 2 stars, 25 He-sds, are found at higher temperatures than Group 1 stars, but in contrast to Group 1, these stars are He-enriched. These stars show super solar carbon abundances. The third group, containing 7 hydrogen-rich sdOs, has lower helium abundances than the second group, but higher temperatures. These stars show a higher carbon abundance than the first group, but a lower one than the second group. From this a relation between the helium and carbon abundance can be found, which is also observed in the field. This relation supports the hot flasher scenario, but the abundances are lower than expected. The coolest stars are located between the ZAHB and the TAHB, which is expected. The hottest hydrogen-rich stars are consistent with a post-EHB nature. As observed in many GCs, the hydrogen-rich sdOs have higher

log g as their field counterparts. The helium-rich objects cluster at around 38,000 K, at the end of the EHB band, at lower temperatures than in the field. The Groups 2 and 3 could be evolutionary connected and be explained by helium-rich objects, which become hydrogen-rich objects through diffusion. The link between these two groups could possibly explain the higher than expected surface gravities (Latour et al. 2014).

One feature significant to ω Cen is the presence of pulsating EHB stars. These stars are hydrogen-rich and in a temperature range between 48,000 K and 54,000 K. These pulsators are unique and lack field counterparts. The stars are found at a temperature, where no pulsation is expected (Randall et al. 2016).

However, the temperatures were underestimated and are higher. This puts the stars in a temperature range where pulsation is expected (Latour et al. 2017). Figure 3.3 shows all the stars in studies by Moehler et al. (2011); Moni Bidin et al. (2011, 2012); Latour et al. (2014).

3.2 NGC 6752

Figure 3.4: Globular cluster NGC 6752 [2]

NGC 6752, depicted in Fig. 3.4, is a core collapse GC in the constellation of Pavo. It is the third brightest in the night sky and was discovered in 1826 by James Dunlop. The GC is located at a distance of 4.0 kpc. With a mass of about 1.4×10^5 $M_\odot$, NGC 6752 is of intermediate mass. The GC contains about 100,000 stars and has a diameter of about 100 ly[3]. NGC 6752 has a mean metallicity of -1.24 dex, which is considered to be intermediate. With an age of 11.78 Gyr it is about as old as ω Cen.

The MS of NGC 6752 is broadened and asymmetric. This hints at a high fraction of binary systems. The width of the MS can not be explained by observational uncertainties, thus a relatively large fraction of binaries is a very good explanation for that observation. The binary fraction is estimated to be about 15 % - 38 % in the inner region and about 16 % in the outer region. This is a behavior that is actually not expected for GC since the binary fraction is expected to be very low. Although NGC 6752 seems to be a pretty average GC at first glance, it appears to have very distinctive features when compared to other GCs. (Marks and Kroupa 2010; Boyles et al. 2011; Forbes and Bridges 2010; Rubenstein and Bailyn 1997)

3.2.1 The horizontal branch of NGC 6752
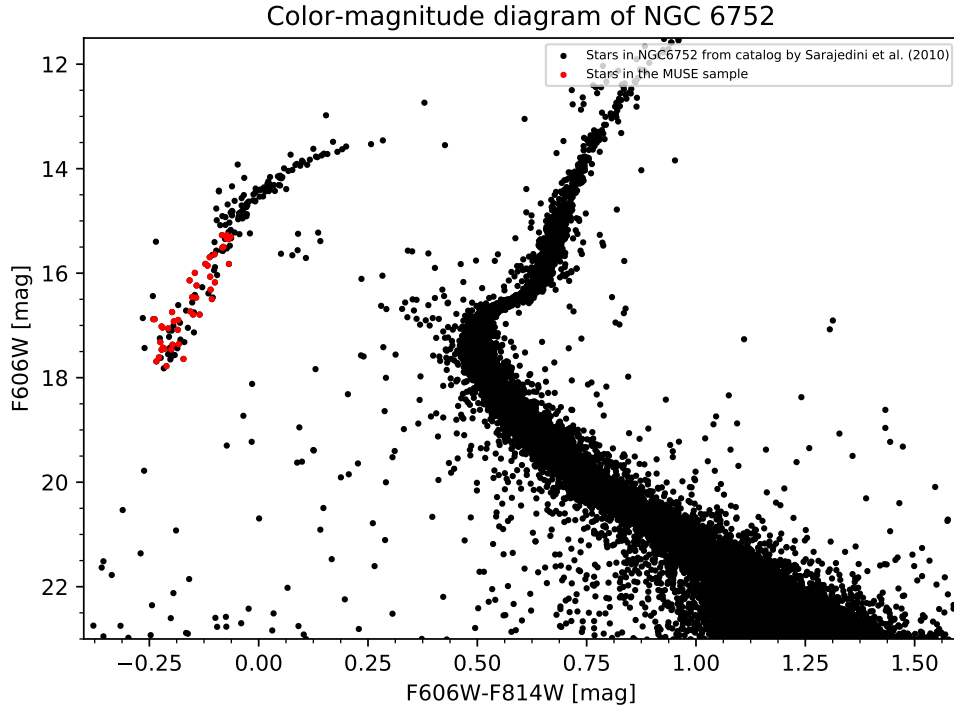
Figure 3.5: CMD of NGC 6752

---

[3]https://apod.nasa.gov/apod/ap130705.html (last accessed: 29.08.2017, 9:50)

The CMD of NGC 6752 is shown in Fig. 3.5. The features mentioned in the previous section can be clearly seen in the CMD. The HB of NGC 6752 has a rather short horizontal part but an extended vertical part in the blue. The cluster has a large population of HB stars. However, the HB has a gap. This gap separates the BHB from the EHB, but there are also stars located within this gap, therefore the gap just has a lower number of stars located within than other parts of the HB. A similar distribution is observed in ω Cen for the BHB and EHB. In contrast to ω Cen NGC 6752 does not show a blue-hook in the CMD. Due to being so bright, the GC is well observed and since it has a large HB population, it is a very well studied GC. The most recent studies will be reviewed shortly. (Moehler et al. 1996)

3.2.1.1 Spectroscopic analysis of HB stars in NGC 6752
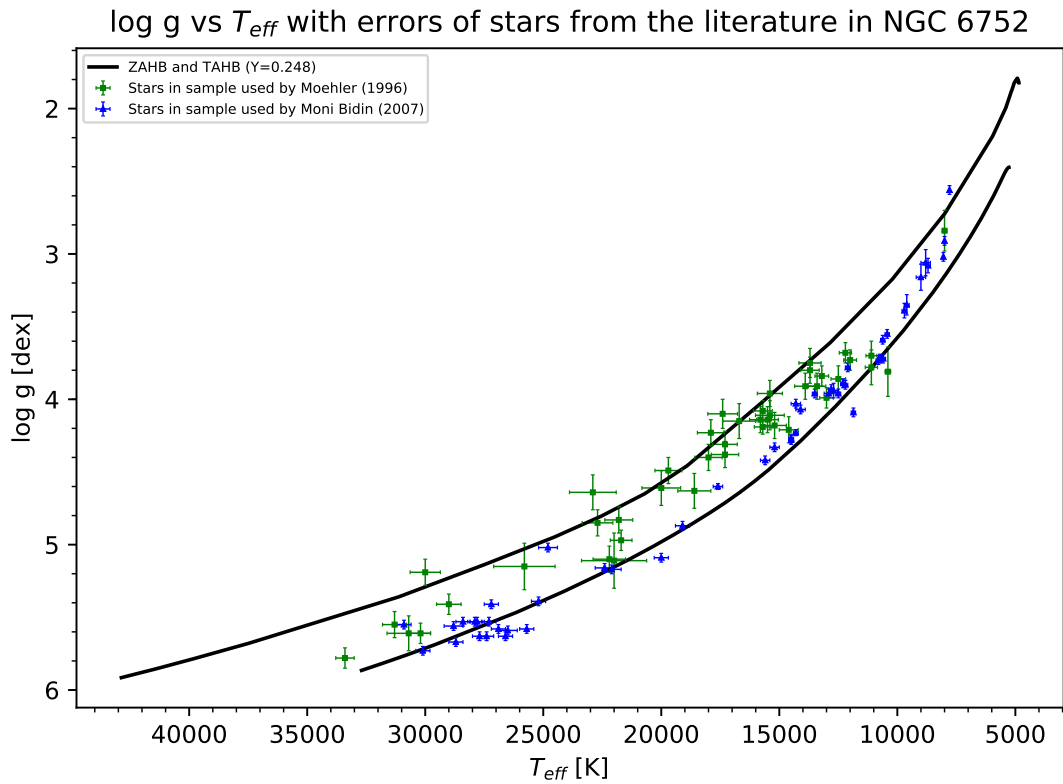
Figure 3.6: T_{eff} -log g diagram containing all the recent results for NGC 6752

Moehler et al. (1996) selected 17 targets from photometric data which were observed with the EFOSC1/2 and EMMI spectrographs in 1992, 1993 and 1995. The spectra were obtained in the optical and UV and had intermediate resolution. The spectra were fitted using blanketed LTE models. The hotter stars were fitted using non-LTE models. The observed stars are divided into multiple groups, namely into BHB, gap stars, EHB

and post-EHB stars. All of these stars are helium-poor and no trend with temperature is observed. The stars with temperatures above 20,000 K all agree well with evolutionary models. The sample also contains post-HB stars. The cooler stars are all found at lower log g than predicted in the log g-T_{eff} diagram. The sample used by Heber et al. (1986) was added to this sample, so the final sample contained 25 HB stars. The stars located below the Newell gap 2 in the CMD are also helium-core burning, except those that have already evolved off the HB. The helium deficiency found in all stars can be explained by diffusion. The comparison with the evolutionary models leads to good agreements, also resulting in the hypothesis, that BHB and EHB stars share the same production processes. Despite this, these models fail to explain the presence of the gap in the HB (Moehler et al. 1996).

Moni Bidin et al. (2007) acquired a sample of 51 HB stars in NGC 6752 in 2002 using the FORS2 spectrograph at VLT. The targets were chosen in a way so that they are distributed over the whole HB. The spectral range used was about 2900 Å wide and the spectra were centered at 4600 Å. The spectra used were reduced and then fitted with a χ^2-method. The models used were LTE solar-abundance models. The hydrogen and helium lines present in the spectra were fitted. Most stars in this sample fall between the ZAHB and TAHB, but at higher temperatures there is a group of stars with higher gravities and at cool temperatures, a few stars can be found laying above the TAHB. Overall, the results of Moehler et al. (1996) and the results of Moni Bidin et al. (2007) show an offset. The helium abundances found are in good agreement with the results of Moehler et al. (1996). One factor influencing the differences between the expectations and observations might be that LTE models were used, which might be inadequate for some stars (Moni Bidin et al. 2007).

One star in the sample used by Moni Bidin et al. (2007) turned out to be a very unique system. The star M5865 is the only known EHB close binary in a GC. What makes it unique is not just the fact that it is the only known binary of that kind in a GC, but also the companion. The companion turns out to be a K-type MS star. A system similar to M5865 has not been observed in the field or in any other GC, and although systems like this are predicted to exist, they should not be that common because low mass companions are preferred by the models (Moni Bidin et al. 2015).

4

The MUSE integral field spectrograph

In astronomy and astrophysics, there are different ways how to gain knowledge about the universe. One is spectroscopy, which is measuring the flux of electro-magnetic radiation of a certain source as a function of wavelength, frequency or energy. These spectra shed light on the dynamics, the chemical composition and many other parameters of a source. It is fairly easy to get the spectrum of a single object in the sky, but often spectra of many sources are needed to see the big picture. Thus over time multi-object spectroscopy was developed to make this possible. One concept to achieve this is integral-field spectroscopy. The MUSE instrument at VLT is one of these units. For GCs the crowding of stars in the inner region complicates spectroscopic observation and even makes observations near the center impossible, but the unique capabilities of MUSE allow to take spectra of stars in the center region of GCs, which was previously only possible from space. Hence it makes sense to observe crowded regions like GCs with MUSE. First an overview of integral-field spectroscopy will be given, followed by an introduction to the instrument MUSE.

4.1 Integral-field spectroscopy

The idea behind integral-field spectroscopy (IFS) is to record the spectrum of every point observed in the field-of-view in one single measurement. Hence a 3-dimensional datacube is recorded with two positional dimensions and one wavelength dimension. The light is fed to classic spectrographs during the exposure. This method is not as sensitive to effects such as seeing, as other spectroscopy concepts, due to the fact that in one single exposure the spectrum of every pixel is measured instantaneously. There are three different concepts of integral field units (IFUs). The concepts mainly differ in the way the field-of-view is observed and analyzed. MUSE uses an image slicer concept, in which the field-of view is sliced in one direction. This is based on classic long-slit spectroscopy, where a single slice of the image is feed to a spectrograph. An IFS, however, can use different concepts to split the field-of-view similar to long-slit spectroscopy, but in an

IFS this is done in a way that several slices can be observed at the same time (see Fig. 4.1). In the image slicer concept, the field-of-view is split up into individual slices using a system of mirrors. These slices are then redirected by mirrors to spectrographs, imitating the concept of long slit spectroscopy. The advantages of this method are the efficiency of the pixel usage and that the spectra are very clean. Old instruments suffered from light loss, but this is solved by advanced image slicers. These slicers use curved instead of flat mirrors and, forming a demagnified image as slicer output, mirrors or lenses are then used to feed the image to the spectrograph.

In another concept a lenslet system is placed in the focal plane, to split the field of view in slices. The single slices can also be directed to the spectrographs using fiber systems. Each method has been successfully applied to instruments. Every method has advantages and disadvantages, hence they all have different areas of application. Usually IFU have a smaller field-of-view than other instruments, but have the big advantage of being able to take spectra of a great number of objects in only one exposure. (Eisenhauer and Raab 2015; Chromey 2010)
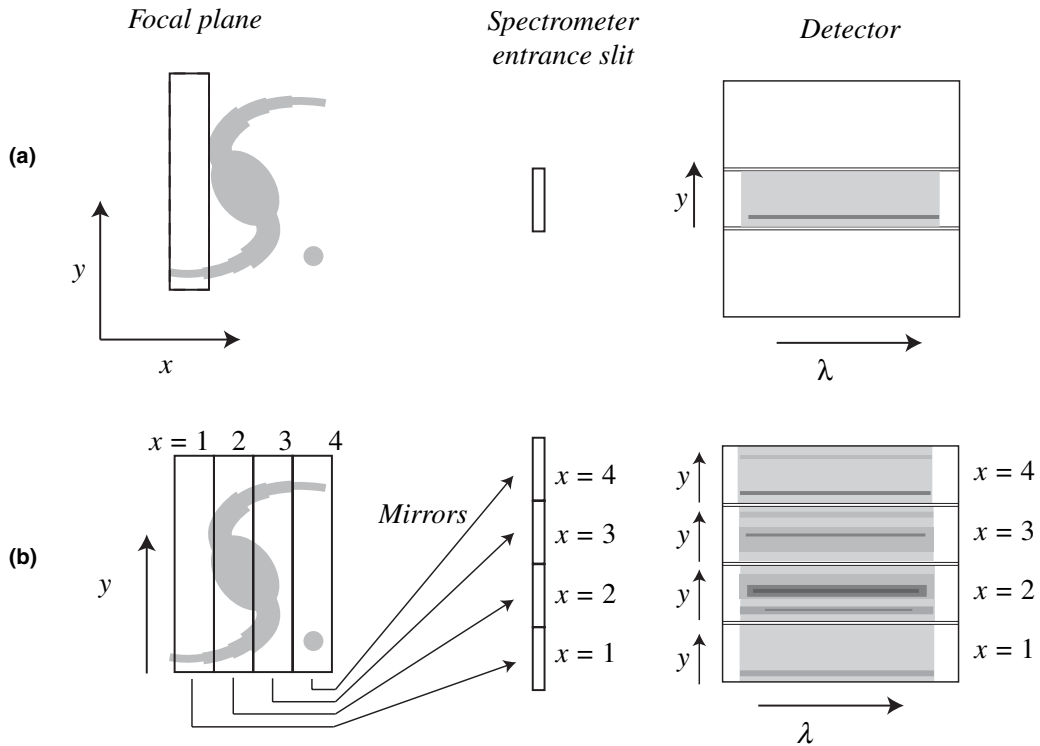
Figure 4.1: Image slicer concept. Panel a) shows a simple long-slit spectrometer input and panel b) shows the principle of the image slicer concept (Chromey 2010)

4.2 The MUSE at the ESO VLT

Figure 4.2: Very large telescope (VLT) at Paranal [1]

The Very Large Telescope (VLT), shown in Fig. 4.2, located at Paranal, Chile, is an ESO facility, where four 8.2 m unit telescopes (UT) are operated, each being equipped with several instruments. The **M**ulti **U**nit **S**pectroscopic **E**xplorer, or short **MUSE**, shown in Fig. 4.3, is an integral-field spectrograph mounted at the Nasmyth focus of UT4 at VLT.

MUSE is a very powerful instrument scanning the sky with an 1×1 arcmin^2 field-of-view. The instrument consists of 24 single IFUs and can be operated in three different modes. A wide field mode, which can be operated with or without adaptive optics and uses the 1×1 arcmin^2 field-of-view, and a narrow field mode with a 7.5×7.5 arcsec^2 field of view. The instrument covers a spectral range between 4650 Å and 9300 Å, with an average resolution of R$\sim$ 3000. MUSE operates as an ideal mixture between a high resolution imaging device and a spectrograph. Due to being constructed from 24 single IFUs a high resolution can be reached. Every IFU consists of a spectrograph with a $(4k)^2$-pixel detector. The single IFUs use the image slicer method. The slicer in the case of MUSE is build from two mirrors, which are easily produced and are cost effective. In total MUSE uses 2304 mirrors, but no movable parts, making it quite stable and easy to

---

[1]`https://cdn.eso.org/images/large/eso-paranal-51.jpg` (last accessed: 24.08.2017, 19:30)

operate. Additionally, the spectrographs are designed to be compact and costefficient, which is accomplished by not using additional optics to correct optical errors. The errors are compensated by slightly tilting the spectrographs. The whole instrument weighs up to 8 t and fills the whole Nasmyth platform at UT4. This corresponds to a volume of about 50 m^3, making it the largest instrument at VLT.
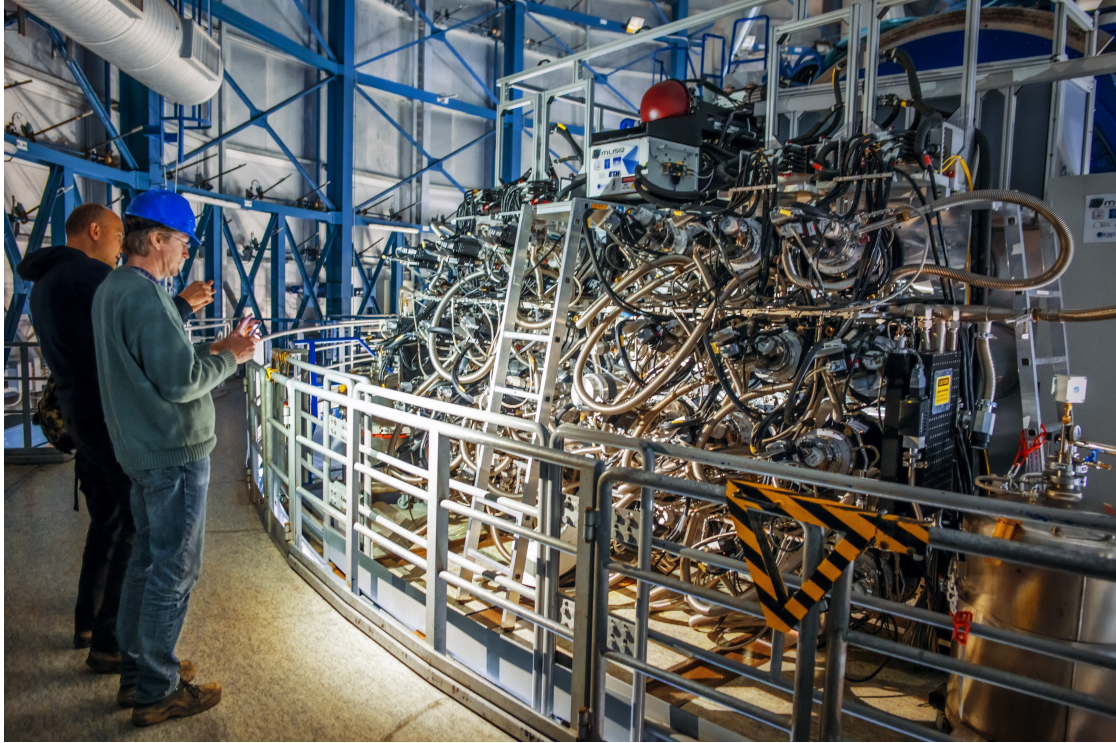
Figure 4.3: The MUSE instrument [2]

---

[2]https://cdn.eso.org/images/large/vlt_atudorica010-cc.jpg (last accessed: 25.08.2017, 17:30)

As already mentioned the field-of-view of MUSE is split using image slicers. The initial field-of-view is split into 24 slices, one for every IFU. This is illustrated in Fig. 4.4. One subfield then has a size of 60"× 2.5". Each subfield is again split into 48 mini-slits with a size of 0.2"×15".
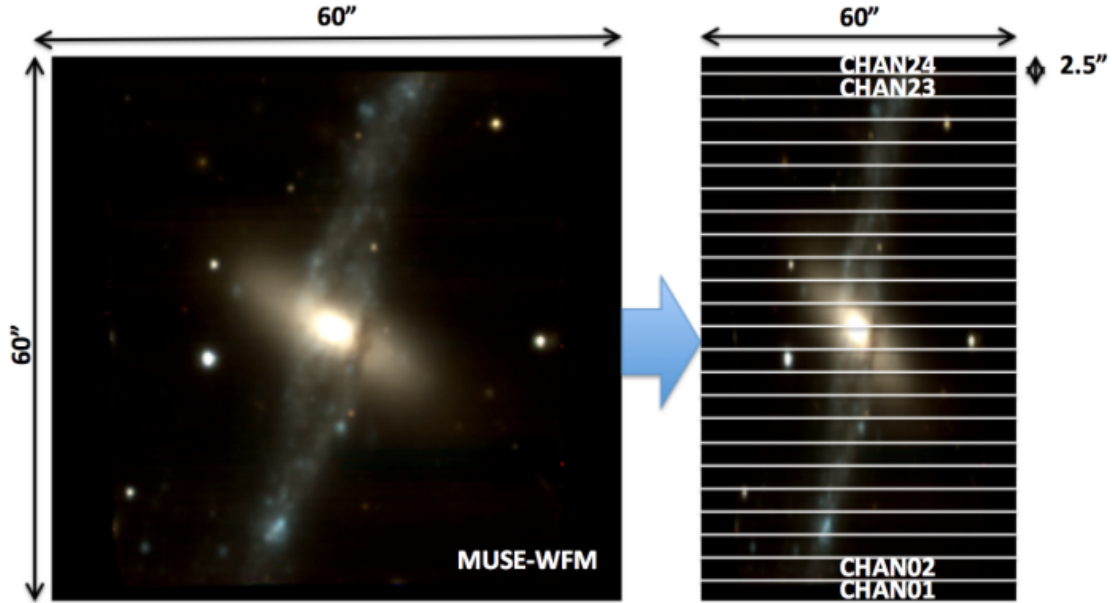
Figure 4.4: How the field-of-view of MUSE is split [3]

The beam is split using slicers and then directed to a spectrograph. This whole unit, slicer and spectrograph, is referred to as IFU. The slicer, as previously mentioned, consists of different mirror systems. The image dissector array slices the field-of-view into 48 parts. The focusing mirror array arranges and aligns the parts for the spectrograph, and finally a slit mask reduces scatter light before the beam enters the spectrograph. The spectrograph then produces the spectra of these split parts by imaging them onto the $(4k)^2$-pixel detector. The spectrograph is built from a collimator, a Volume Phase Holographic Grating, a camera system, and the CCD detector. The scheme of a single IFU is displayed in Fig. 4.5.

---

[3]http://www.eso.org/sci/facilities/paranal/instruments/muse/inst.html (last accessed: 26.08.2017, 15:35)
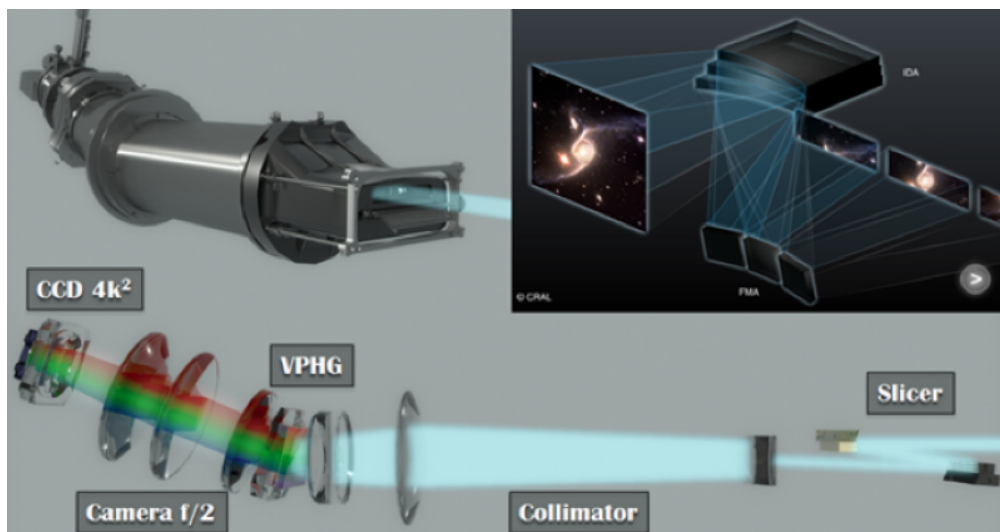
Figure 4.5: IFU of MUSE [4]

The adaptive-optics (AO) system (see Fig. 4.6) used in combination with MUSE is called GALACSI. It will be operational in the near future and it will use four lasers to produce four synthetic guide stars to correct atmospheric turbulences. The system will also use one tip-tilt star to correct the atmospheric tip-tilt. This AO system will allow a better spatial resolution and different operation modes.

Until now MUSE could only be used in the wide field mode without AO. In this mode, the field-of-view is 60"×60" and is spatially sampled in 0.2"×0.2". Without AO, the spatial resolution is 0.65 arcsec, but with AO it can be improved up to 0.46 arcsec. The limiting magnitude for a detection in this mode is 25 mag with full resolution and 80 h integration time. The wide field mode can be used for numerous applications. For example, MUSE can be used to study faint galaxies at high redshifts, detect Lyα emission to study the cosmic web and reionisation, to spectroscopically resolve galaxies, or to study dark matter halos. MUSE can also be used to study nearby objects. At low redshifts, the dynamical structure and stellar populations of GCs or nearby galaxies can be studied, especially the central regions because the extends of those objects are much larger than the field-of-view.

Once GALACSI becomes available, MUSE can also be used in the narrow field mode. This mode offers a higher spatial resolution. The field-of-view will be 7.5"×7.5" at a sampling of 0.025"×0.025" and a spatial resolution of 0.042 arcsec. The limiting magnitude with 1 h integration time will be about 22.3 mag. However, the spectral range will be smaller than in the wide field mode with a range from 6000 Å to 9300 Å. This mode will allow to study smaller objects in detail. It can be used to observe super massive black holes and study the chemical composition and dynamics of the surroundings of a black hole, but also young stellar objects are of interest. Here MUSE

---

[4]http://www.eso.org/sci/facilities/paranal/instruments/muse/inst.html (last accessed: 26.08.2017, 15:35)

can provide insight about formation of jets. However, MUSE is not restricted to extra- or galactic objects. Solar-system objects can be observed as well. This would make it possible to study the atmospheres of the gas planets or to monitor volcanic activities of moons located in the solar system.

In summary, MUSE is a powerful instrument that will be used to make huge progress in several fields of astrophysics. (Bacon et al. 2006; Husser et al. 2016; Eisenhauer and Raab 2015)
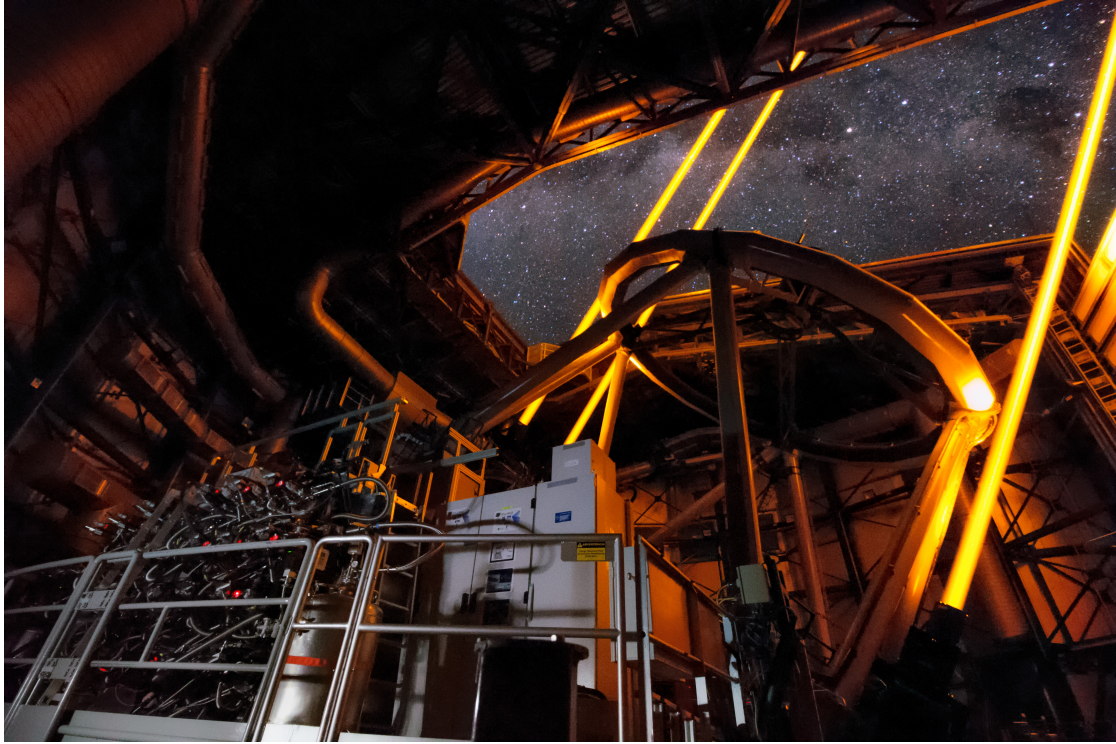
Figure 4.6: MUSE in operation with adaptive optics [5]

---

[5]https://cdn.eso.org/images/large/eso1724d.jpg (last accessed: 25.08.2017, 17:40)

4.2.1 Data reduction

The data reduction for MUSE data is very complex, since one single exposure will produce 1.6 GB of data and the data has a 3D structure. If AO is included, the data reduction becomes slightly more complex.

The data reduction generally is done in two steps. In the first step basic reductions are performed, such as bias correction, flat fielding and wavelength calibration. This step is performed on an IFU-basis, therefore individually for every IFU. After this process the CCD raw data is converted to pixel table data. In the second step, further procedures are performed such as sky subtractions, flux calibration and after that a coordinate calibration. The final output of the MUSE pipeline then is a FITS-file containing information on flux, wavelength, the uncertainties and the spatial position.

In order to extract single-object spectra from the data further data-reduction procedures are required. Of special interest for studying GCs is the reduction method to extract single-stellar spectra. Here an existing catalog of photometric data is used. In the beginning, a guess for the point-spread function (PSF) of the MUSE data is used to start the procedure. Analytic fit functions for parameters of the PSF and a mock-MUSE image from the catalog are used to obtain an initial guess for the coordinate transformation. Via signal-to-noise estimate and the density of sources, sources are identified for which a meaningful extraction can be performed. All this information is used as initial guesses for a flux fit to every layer. After every step, the sources that can not be singled out are subtracted and the fit is performed again with the results of the previous one as initial guesses. This is performed until convergence is reached. From this procedure a final PSF model is derived, which is then used to fit the parameters of the PSF with polynomial functions. The use of polynomial functions is justified by the fact that variations between the layers are smooth. This estimate and the coordinates of the different sources are then used to perform the final flux fit of every source to every layer of the datacube. The results of this final step are single-stellar spectra.

Through this method it is possible to extract a large number of single-stellar spectra from the MUSE data. With this extraction method the largest sample of single spectra for a GC was obtained by Husser et al. (2016), containing spectra of 12,307 individual stars in the GC NGC 6397.

It is also possible to combine spectra of a single stars from different exposures, resulting in a higher signal-to-noise for the final spectra. (Kamann et al. 2016; Weilbacher et al. 2014; Kamann, S. et al. 2013)

The reduction and the combination of the spectra used for the analysis were performed by the MUSE team in Göttingen.

4.3 Stars observed with MUSE in ω Cen

The red stars in the CMD shown in Fig. 3.2 are the stars in the sample. The spectra were all obtained between 2015 and 2017, in multiple pointings with MUSE and spectra of the same star were combined together later, to increase the signal-to-noise (S/N) ratio (SNR). The exposure time for a single spectrum was between 450 s and 1000 s. The data were reduced with the previously described procedure. The final fits-files include the ID-number, the SNR, the magnitude, the number of spectra that were combined (nspec), the coordinates of the target, and the spectrum. The observational data can be seen in the appendix in Table 1. In comparison to the previously analyzed samples, the stars observed with MUSE are not limited to the outer region of the GC. With MUSE it is possible to observe the center region of ω Cen and for the first time obtain a large sample of BHB/EHB stars in the central region. Figure 4.7 shows the position of the stars in the cluster. The sample, referred to as MUSE sample, includes 121 HB stars. The stars were selected from the CMD of the stars observed with MUSE. The stars were selected to include the BHB and EHB, so there is a upper magnitude cut for the targets. The fainter objects, in general, display a lower S/N.
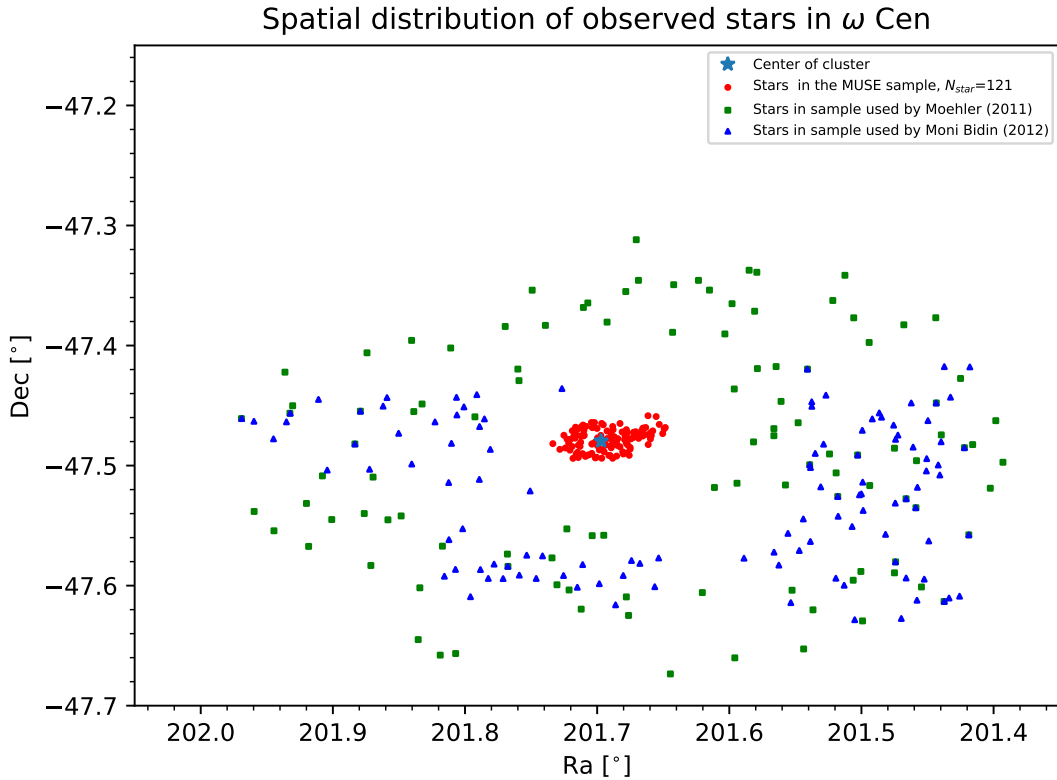
Figure 4.7: Spatial distribution of observed stars in ω Cen

4.4 Stars observed with MUSE in NGC 6752

The MUSE sample of NGC 6752 contains 43 HB stars. The spectra were all gathered between 2015 and 2017. Similar to ω Cen multiple pointings were made with MUSE, but with an exposure time of 1200 s for a single spectrum. The spectra of stars that were observed multiple times were also combined. As can be seen in Fig. 3.5, the stars are located on the BHB and EHB. Again the red stars in the CMD mark the stars included in the MUSE sample. Table 2 in the appendix displays the observational data for the MUSE sample in ω Cen. The parameters included in the table are the same as for Table 1 The position of the stars in NGC 6752 is shown in Fig. 4.8. The stars included in the other samples of NGC 6752 are restricted to the outer region, but with MUSE, it is possible to obtain a large sample of spectra from stars located in the center.
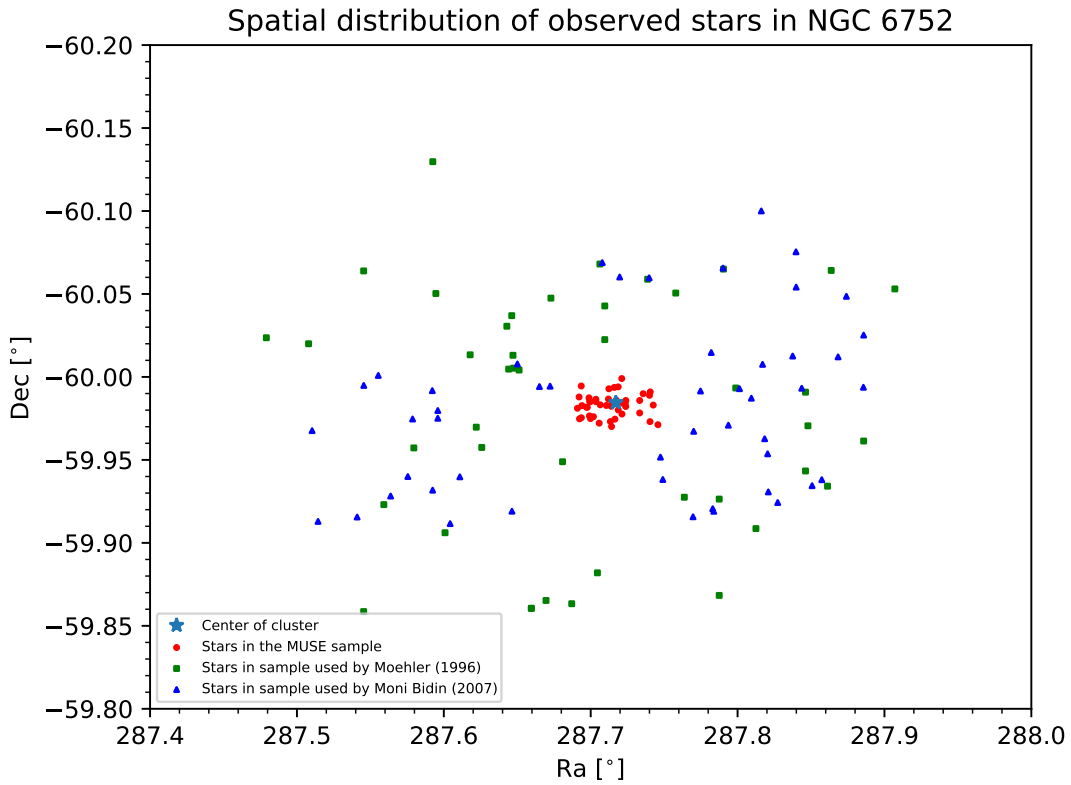
Figure 4.8: Spatial distribution of observed stars in NGC 6752

5

Spectroscopic analysis

Both samples of MUSE spectra were analyzed and the atmospheric parameters, T_{eff} log g and helium abundance, were determined using a fitting routine. In this chapter, the analysis will be described. In addition, the method used to determine the atmospheric parameters will be reviewed briefly.

5.1 MUSE spectroscopy of horizontal branch stars

In the past HB objects have been mostly investigated using the optical range between about 3600 Åand 6000 Å. MUSE uses a range between 4650 Å and 9300 Å, a range that is redder than the one usually used for the analysis of HB stars. This, of course, means that other lines are visible in the spectra than the ones usually used. In the MUSE range BHB stars are identified by the presence of two Balmer lines, H_{α} and H_{β}, rather prominent Paschen lines and a few helium I lines. As the temperature increases, the Paschen lines become less prominent. sdBs hardly show Paschen lines, but they have strong Balmer lines and also show helium lines, but of course this depends on the helium abundance. The hotter stars, sdOBs, start to show a weak helium II line, while on the other hand, the helium I lines become less dominant. These stars show Balmer lines but no Paschen lines. The helium I lines, if present, are very weak. The Balmer lines become less prominent with increasing temperature. Figure 5.1 shows the different spectral types displayed in the MUSE spectral range.
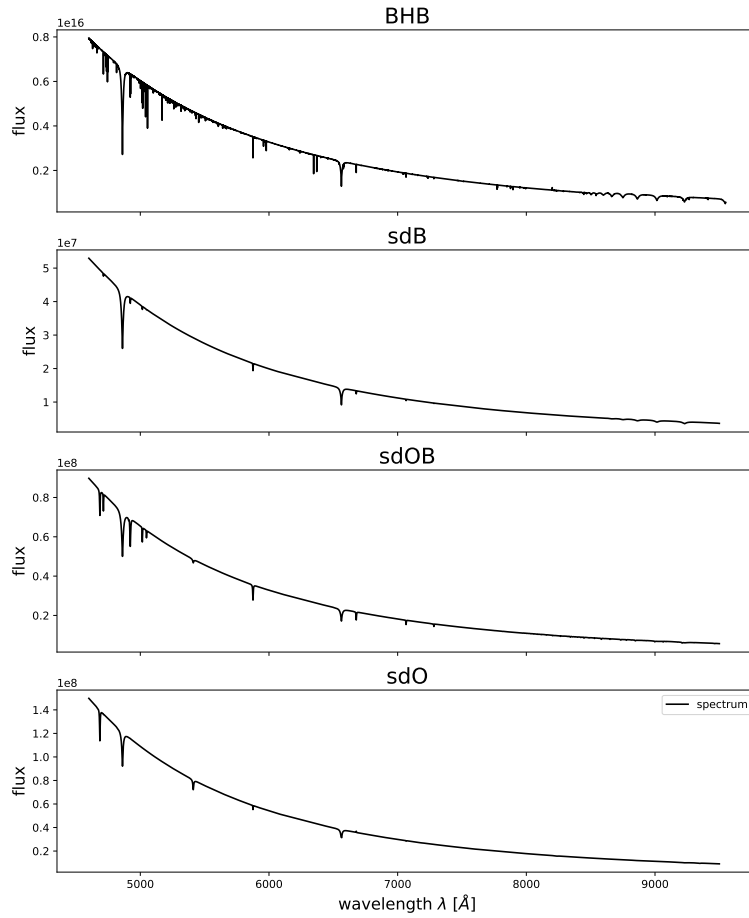
Figure 5.1: Comparison of different spectral types in the range offered by MUSE (theoretical spectra used)

5.2 The analysis procedure

In general all available hydrogen and helium lines in the spectral range offered by MUSE were fitted during the fitting routine. A list of all these lines can be found in Table 5.1. Since several lines are very weak, especially the helium lines in the helium-poor stars, these areas were also used in the fit when the line was not really visible. Unfortunately, it was not possible to use the exact same ranges for every line in the fits since the fitting routine sometimes had problems with a certain range for a few spectra. In the following section, the used models and routine will be discussed.

5.2.1 Model atmospheres

The model atmospheres used were computed by Heber et al. (2000). The models are LTE models computed using an improved version of the Linfor code by Lemke (1997).

Table 5.1: Hydrogen and helium lines in the MUSE spectral range [1]

Line	wavelength [Å]	Line	wavelength [Å]
H_α	6562.79	H_β	4861.35
Paschen 3-9	9229.70	Paschen 3-10	9015.30
Paschen 3-11	8862.89	Paschen 3-12	8750.46
Paschen 3-13	8665.02	Paschen 3-14	8598.39
Paschen 3-15	8545.38	Paschen 3-16	8502.49
Paschen 3-17	8467.26	Paschen 3-18	8437.95
Paschen 3-19	8413.32	Paschen 3-20	8392.40
Paschen 3-21	8374.48	Paschen 3-22	8359.00
Paschen 3-23	8345.54	Helium I	4921.93
Helium I	5015.68	Helium I	5047.74
Helium I	5875.62	Helium I	6678.15
Helium I	7065.19	Helium I	7065.71
Helium I	7281.35	Helium I	9210.34
Helium II	5412.00	Helium II	6560.20

For the models opacity distribution functions were used in order to take care of line blanketing and a plane-parallel geometry and hydrostatic equilibrium were assumed. To include the spectral lines in the models, the Kurucz line list was used. The models have a mean metallicity of -1.0 dex. They cover a temperature range between 12,000 K and 50,000 K. In total, the models cover a log g range from 3.6 dex to 6.4 dex, but this range is not available for the full temperature range. The subrange between 12,000 K and 19,000 K has the full log g range, but the range from 19,000 K to 50,000 K only has a minimum log g of 4.8 dex available. This is not a problem since stars with a higher T_{eff} are expected to have a higher log g. In the lower temperature subrange the temperature is increased in 1,000 K steps. In the higher temperature range the steps are 2,000 K. The log g is always used in 0.2 dex steps. The models cover a helium abundance between $\log(N(\text{He})/N(\text{H}))$=-4.0 dex and $\log(N(\text{He})/N(\text{H}))$=-1.0 dex, in 0.5 dex steps. If a fit yielded a higher or lower helium abundance than covered by the grid, the fit was repeated with the helium abundance fixed to the upper or lower limit covered by the grid. (Heber et al. 2000; Lemke 1997)

5.2.2 SPAS

The program used to perform the fits is called SPAS. The **S**pectrum **P**lotting and **A**nalysis **S**uite was developed by Heiko Hirsch in 2009 and is based on the fitting procedure established by Napiwotzki in 2004. The code by Napiwotzki is called FITSB2. This routine uses a χ^2-method to determine the best fit for a spectrum by interpolating between a three-dimensional grid of model spectra. Not the whole spectrum is fitted, but only preselected ranges, with the fit being done in all of these ranges simultaneously.

---

[1] https://physics.nist.gov/PhysRefData/ASD/lines_form.html

Those ranges are normalized by SPAS before the actual fit is performed. SPAS uses a downhill simplex algorithm to determine the best fit parameters. This method is rather slow but reliable. The χ^2-function is used to evaluate the goodness of every vertex of the simplex. The worst vertex is replaced, with the consequence that the simplex is changed. This is repeated until the difference between the χ^2-function at every vertex is below a certain value or until the maximum number of iterations is reached. The vertices of the simplex are computed by interpolating in the grid of model spectra. The interpolation first is performed on the abundance-value, then on the log g and in the end, on the temperature. Then the spectra are rebinned by interpolation to match the original data. For minimizing the χ^2, the flux of the model spectra is scaled to the one of the spectrum that is fitted. This happens by dividing the model by the observed spectra and performing a linear fit. This fit is then used to scale the fluxes to the same level. The radial velocity is calculated by fitting a Voigt function to the lines and using the Doppler formula. The determination of the radial velocity can also be performed without model spectra.

SPAS uses a bootstrapping method to determine the uncertainties. Therefore, the results are randomly replaced and a fit is performed. This is done several times. The standard deviation of the parameter from the iterations is the standard error. This requires long computation time, but the errors are considerably low. For the analysis of the spectra, 500 bootstrapping iterations were performed to determine the uncertainties. (Hirsch 2009; Napiwotzki 1999)

An example fit to the spectrum shown in Fig. 5.2 can be seen in Figures 5.3 and 5.4. Figure 1 in appendix A3 shows the spectrum of an EHB star.
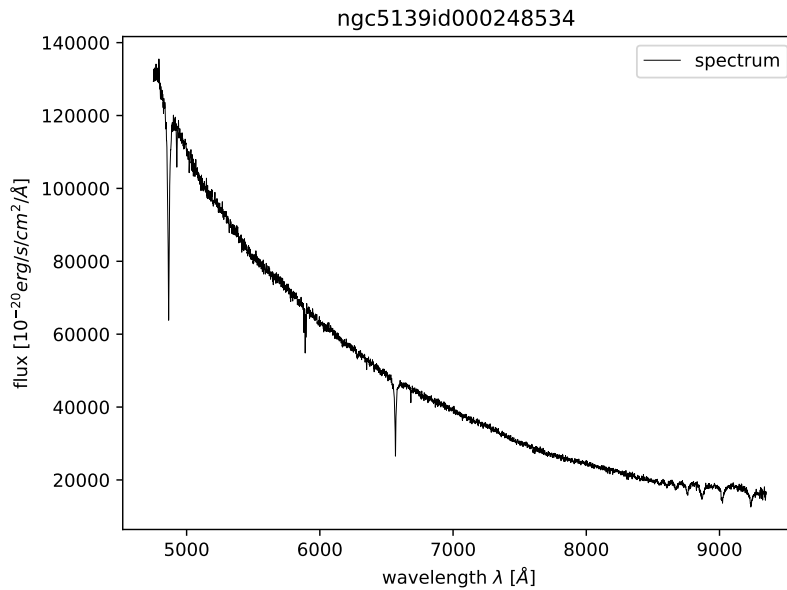
Figure 5.2: Spectrum of the star 248534, a BHB star, in ω Cen observed with MUSE
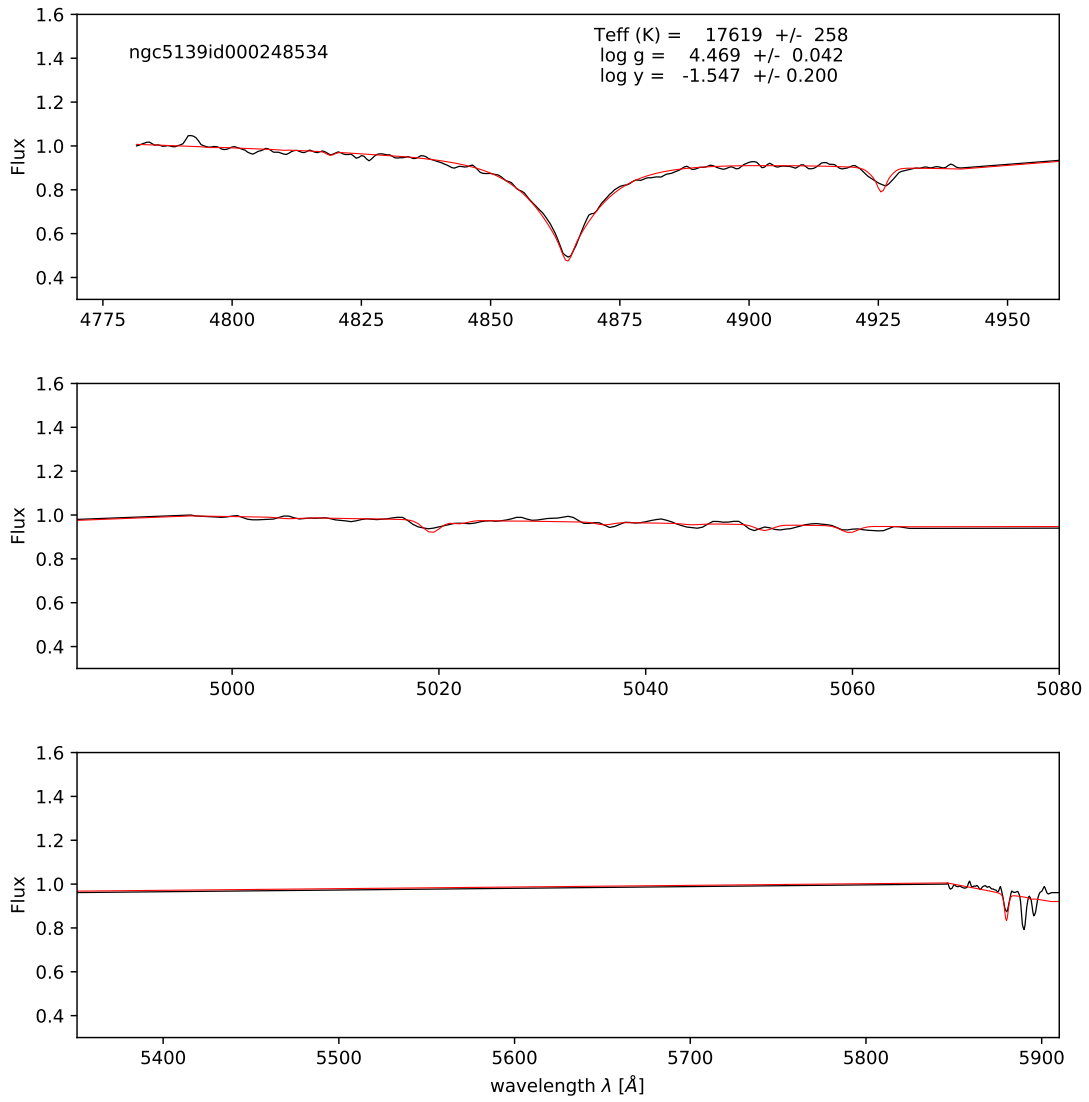
Figure 5.3: Fit of the spectrum of the star 248534 in ω Cen (part a)
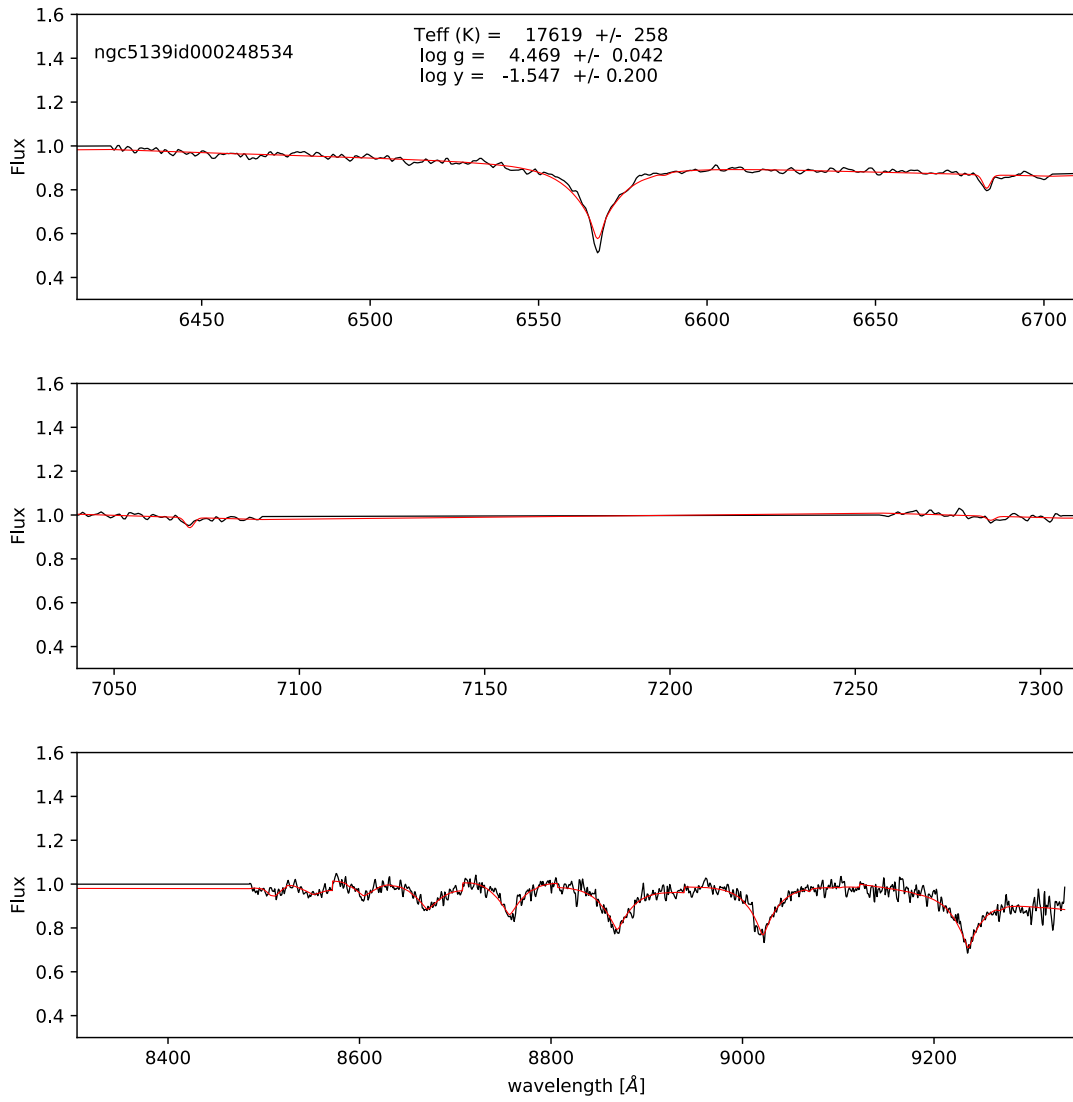
Figure 5.4: Fit of the spectrum of the star 248534 in ω Cen (part b)

6

Results

In this chapter the results will be presented. First, it will be discussed which signal-to-noise ratio (SNR) is needed in order to yield reasonable results. Afterwards, the results from the spectral fits and the comparison to previous studies will be discussed.

6.1 Influence of signal to noise on spectra

Since the quality of the spectra is different, it is important to sort out the spectra with a quality too low to yield reasonable results. One quantity that describes the quality of an astrophysical measurement is the so called signal-to-noise ratio. Since the spectra obtained have different SNR, it is necessary to find out at which lower limit this quantity can be in order to still deliver good results. For this reason, the influence of the SNR on the fit and the results was investigated. This procedure is also used to see how good the fitting routine works and to find a reasonable SNR cut.

For this purpose a set of model atmospheres, that were computed using the codes TLUSTY[1] and SYNSPEC (Lanz and Hubeny 2003) were taken from the model grid presented by Brassard et al. (2010). Similar models were used by Latour et al. (2014). In contrast to the models used in the fitting routine, these models are non-LTE (NLTE) models. They cover a temperature range from 20,000 K to 50,000 K, going in 2,000 K steps, a log g range from 4.6 dex up to 6.4 dex in 0.2 dex steps and the helium abundance range covers abundances from -4.0 dex to 0.0 dex in 0.5 dex steps. The models include different elements, all based on the abundances found in sdB stars. The elements S, Fe and N were considered with a solar abundance and the elements O, C and Si were included with 1/10 of the solar value (Blanchette et al. 2008). This set of models was used as models in the fitting routine for this evaluation. The same spectra were also used as "observational" spectra. A set of spectra with different atmospheric parameters, covering the whole range of parameters available, were selected. Since these synthetic spectra have no noise at all, it is necessary to apply different levels of noise to these

---

[1] http://nova.astro.umd.edu/

pre-selected spectra. This was accomplished by writing a python program that had a synthetic spectrum as an input and added noise to this spectrum. The selected atmospheric configurations used are listed in Table 6.1. The SNRs tested were: 4, 10, 40, 60, 80, 100, 120 and 300, so these spectra cover about the same SNRs present in the actual data.

These mock observed spectra were then fitted with the fitting routine used for the spectral analysis. The resulting fit parameters were then compared with the actual, real spectra parameters. For high SNRs, the differences between the real and the resulting parameters were very small. Within the errors the difference can be considered to be zero. For very low SNRs, the differences become more obvious. Although the error range also includes the possibility that the difference is zero, the errors are so huge, that the results from spectra with these ratios are not meaningful. The mean differences between real and derived parameters at these ratios are far from zero. Figure 6.1 shows the differences between the real parameters and the fit results for one atmospheric configuration. Judging from these results, the fit-routine handles the different SNRs pretty well. The results were also used to apply a S/N-cut to the MUSE data, therefore all spectra with a SNR below 20 were excluded from the analysis, since according to the results MUSE spectra having a SNR above 20 should give reasonable results.

Table 6.1: Parameter combinations used to investigate the SNR influence on the fit

T_{eff} [K]	log g [dex]	log N(He)/N(H) [dex]
22,000	4.6	-3.0
26,000	6.0	-4.0
30,000	5.2	-1.0
34,000	5.6	-1.0
40,000	6.4	-1.5
44,000	5.0	-2.0
46,000	5.8	-2.0
48,000	6.2	0.0
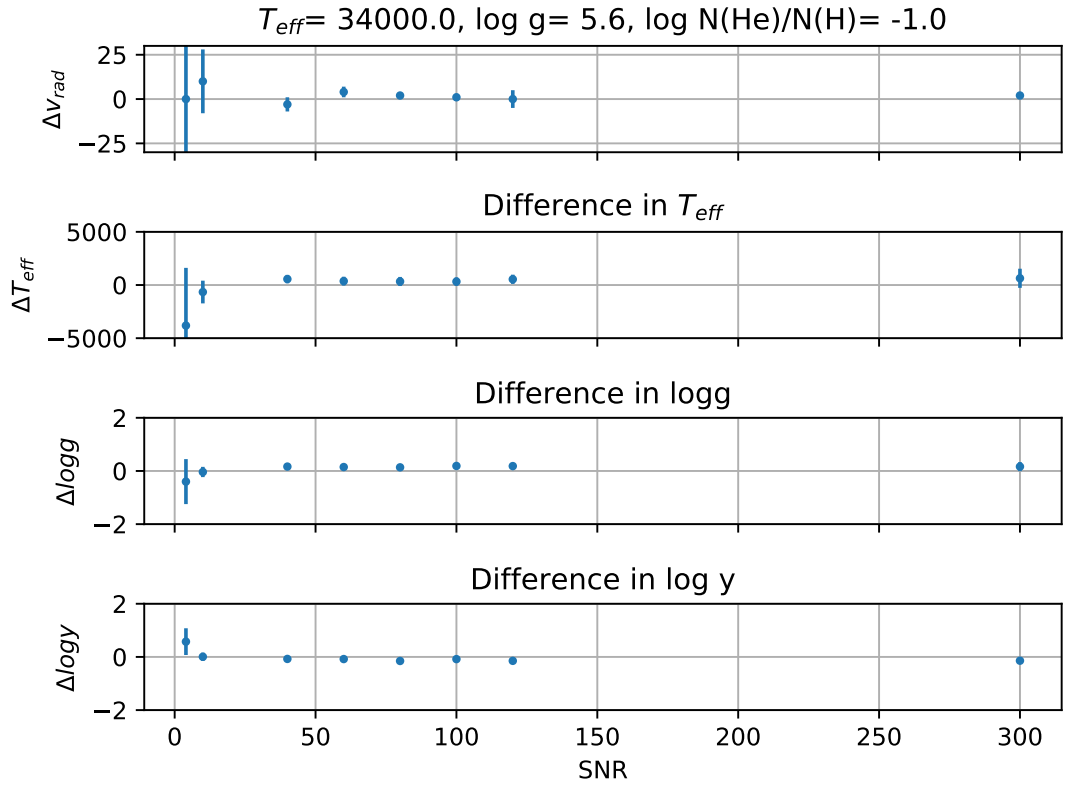
Figure 6.1: Differences between the real parameters and the results of the fit for different SNRs. Real parameters: T_{eff} =34,000 K, log g=5.6 dex and log N(He)/N(H)=-1.0 dex

6.2 ω Cen

After removing the spectra with a SNR below 20, 103 stars remained in the sample. These stars were analyzed using the previously described fitting routine. The results for ω Cen and NGC 6752 will be presented in the following order: first the dynamical analysis will be discussed, followed by the atmospheric parameters. The results will be concluded by a comparison to literature ones.

6.2.1 Cluster-dynamics

The dynamical characteristics of the stars in a GC are of great importance. These properties can be used to uncover the structure of the cluster. For example it can be used to see if there might be a heavy central object, such as a black hole, but they can also be used to simply confirm the cluster membership of the star. During the fitting routine the radial velocity was determined. The radial velocity distribution of the ω Cen sample is depicted in Fig. 6.2. The mean velocity of the stars is $231.14 \pm 15.20 \frac{km}{s}$. This value was determined by fitting a Gaussian distribution to the histogram of the radial velocities. The mean velocity is in good agreement with the clusters radial velocity, which is $232.1 \frac{km}{s}$ (Moni Bidin et al. 2012). The determined dispersion is $22.87 \pm 4.78 \frac{km}{s}$, which is higher than the cluster dispersion of about $13 \frac{km}{s}$ (Moni Bidin et al. 2012), but this is not surprising since this is the value for the entire cluster and the velocity dispersion in the center is expected to be higher. The comparison to the central dispersion of $21.9 \pm 3.9 \frac{km}{s}$ derived from stars located in the central arcminute (Meylan et al. 1995), however, yields an excellent agreement. From these results all stars seem to be cluster members.
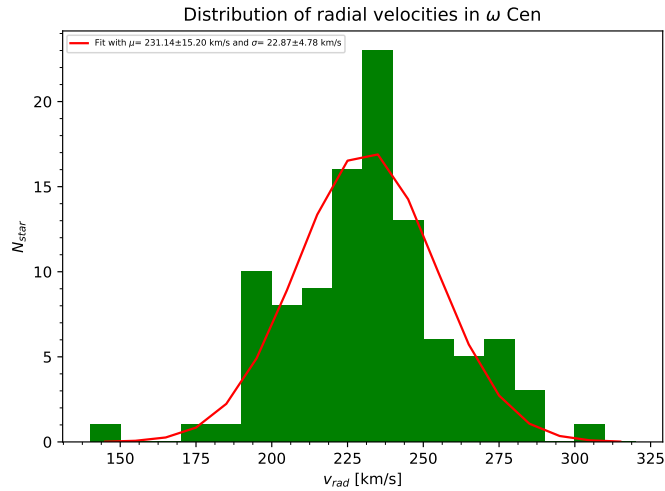
Figure 6.2: Radial velocity distribution of ω Cen sample with the Gaussian fit

For the dynamics of the whole GC, also the dispersion of stars with different distances from the center is interesting since it can give insight, for example, about a potential central object. Because the objects in the sample cover a variety of distances from the cluster center, the dynamics can be further investigated. Generally, it is expected that the dispersion decreases with the distance from the center. This behavior can be seen in the data as well, as shown in Fig. 6.3. The stars were binned into bins containing an equal number of stars, and for each bin the dispersion was determined. The dispersion decreases with the distance from the center, but the uncertainties are quite high due to a low number of stars in the sample. For a more detailed and reliable dynamical study more stars would be needed, for example, to confirm or exclude a black hole in the center. Nevertheless, the sample displays the expected behavior. This analysis in particular is therefore a qualitative analysis only.
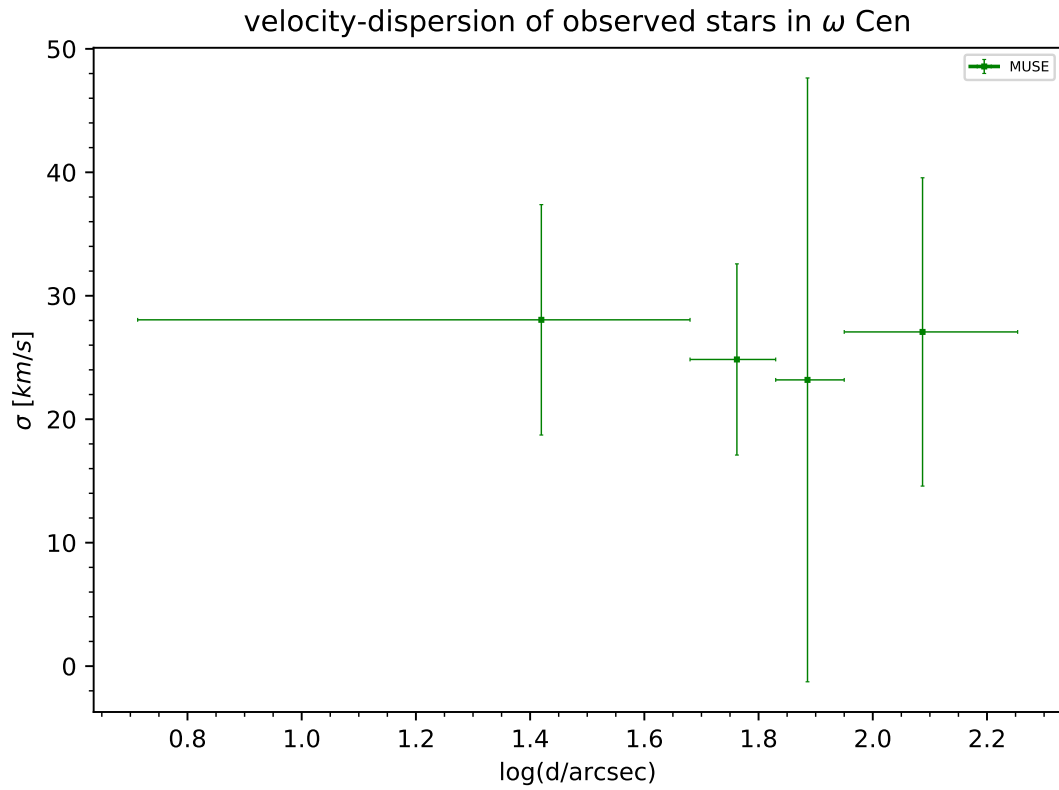
Figure 6.3: Velocity-dispersion of stars in a certain distance from the center

6.2.2 Atmospheric parameters

The temperatures observed in the sample range from 12,000 K up to about 42,000 K. The distribution of T_{eff} can be seen in Fig. 6.4. From the distribution it is quite obvious that the stars can be divided into at least two groups. The cooler stars, the BHB stars, display temperatures between 12,000 K and 20,000 K, with maxima at about 15,000 K and 20,000 K. The hotter stars have a maximum at about 35,000 K. From this sample it can be seen that ω Cen has a great variety of different HB stars. The sample contains
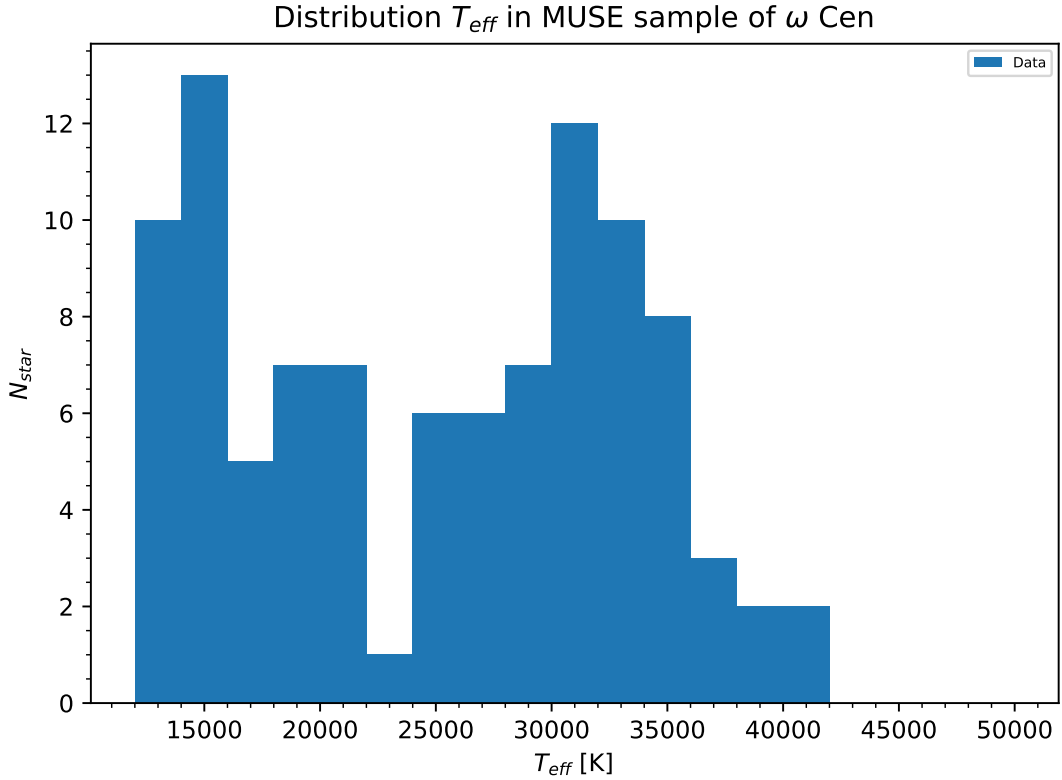
Figure 6.4: Distribution of observed T_{eff} in ω Cen

a large number of BHB stars which seem to be, at least judging from the distribution, separated from the EHB stars by a gap at about 23,000K. This gap is expected, but it should actually be at a slightly lower temperature. The absence of very hot objects, however, could be due to the fact that these objects are the faintest ones and therefore, have lower SNRs than the cooler objects.
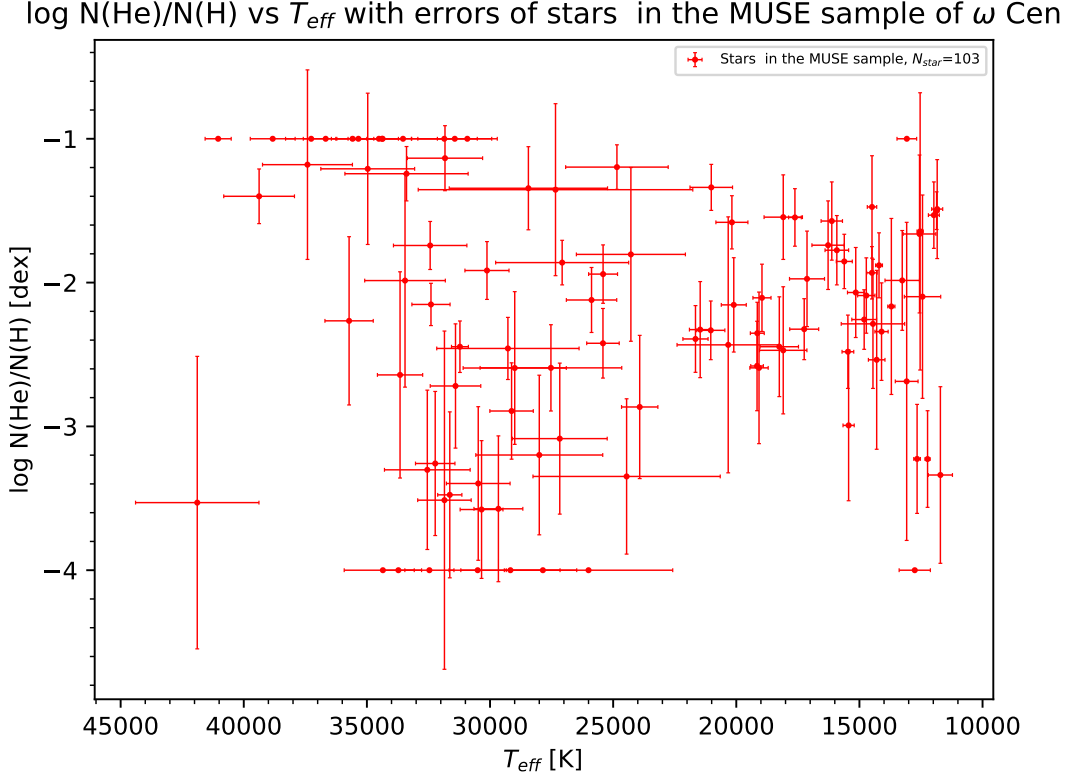
Figure 6.5: Helium abundance as function of T_{eff} in ω Cen

Since the models used unfortunately only cover a helium abundance between -4.0 dex and -1.0 dex, the stars showing an abundance higher than solar are fixed to the upper limit of the grid. The helium-poor stars are sometimes fixed to -4.0 dex, since due to the absence of helium lines the characterization of the helium abundance is limited. Therefore helium-rich objects, if they are present in this sample, will return a lower limit of -1.0 dex, but stars that hit the upper limit of the gird are most likely helium-rich. Still the measured abundances can be reasonably interpreted.

The helium abundance of the BHB stars in the sample clearly show a trend with T_{eff}. As known from literature (see Moni Bidin et al. (2012)), the helium abundance in this temperature range first decreases and then, after reaching a minimum, increases again. This trend can be seen in Fig. 6.5 among the BHB stars. This is probably due to diffusion. Through this effect the helium abundance will decrease. As the trend shows, the efficiency of diffusion seems to be linked to the temperature, with the efficiency first increasing and then again decreasing. However, a group of helium-poor BHB stars is still seen in the sample. There seem to be two families of EHB stars, with one being helium-poor and one being around or possibly above solar level. The helium abundance of the EHB stars might increase with temperature, but this is not really clear.

log g vs T_{eff} with errors of stars in the MUSE sample of ω Cen
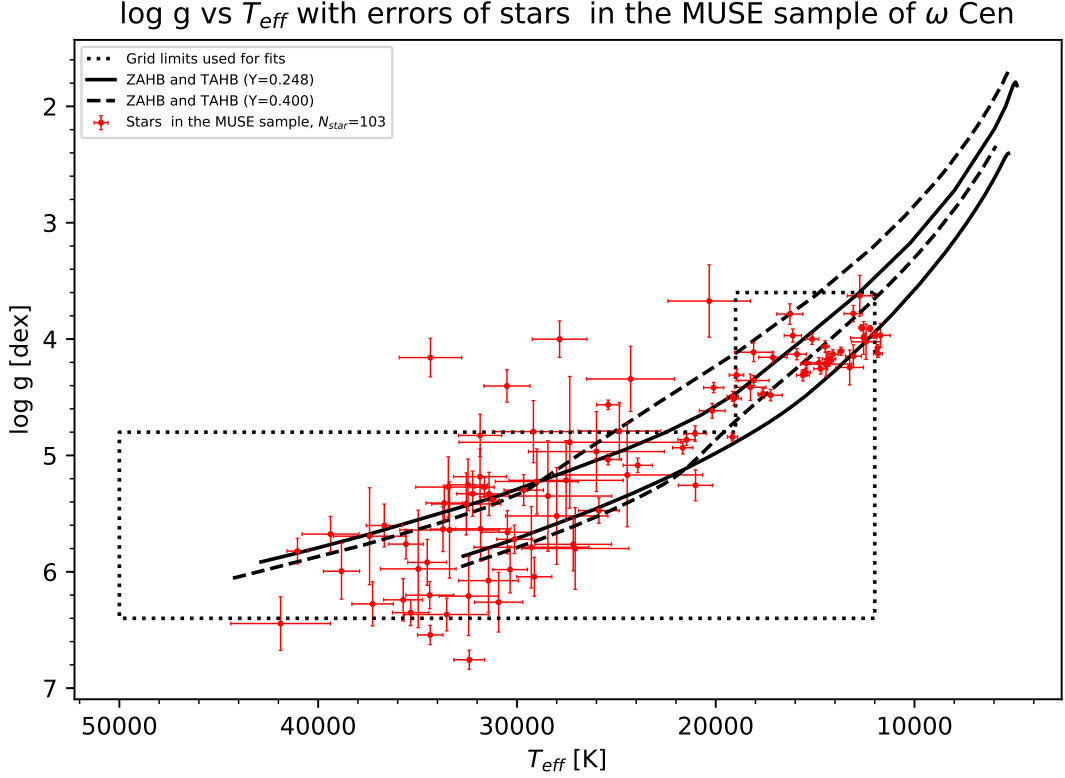
Figure 6.6: log g-T_{eff} diagram of stars in ω Cen

The log g-T_{eff} diagram is a powerful instrument to investigate not just the atmospheric parameters, but also the evolutionary status of the stars observed. Since it is known that ω Cen hosts different subpopulations, the log g-T_{eff} diagram in Fig. 6.6 shows two theoretical HB bands with different initial helium abundances. The solid lines represents an initial helium abundance of Y=0.248 and the dashed lines shows the HB band for stars born with a higher helium content (Y=0.400). Since a second helium-enriched population in ω Cen is often discussed as a possible explanation for the atmospheric parameters derived for some HB stars in ω Cen, it is worth to compare the results to this scenario. Most stars in the sample fall between the ZAHB and TAHB, which puts them into their helium-core burning phase and identifies them as HB objects. A few stars, that do not fall in the HB band for the canonical helium abundance, fall on the band for a higher initial helium abundance. This of course would also identify them as HB stars and could be understood as a hint that these stars could belong to the He-enriched subpopulation. Along the different HB bands, stars cluster especially at higher temperatures. Within the errors these stars could be HB stars. The stars clustering at the TAHB could be evolving away from the HB. Since the uncertainties are quite large, both explanations could be possible. Another possible explanation could be the fixing of the helium abundances to the limits of the grid. The fixing could result in a slightly

wrong log g. For the ones at high log g's, this would mean that the log g derived is too high and, vice versa, for the stars above the TAHB, a log g that is too low is derived. On the other hand the temperatures could be underestimated due to the usage of LTE models. The stars far away from the TAHB, those found at lower log g's above the TAHB, could be post-EHB objects currently evolving towards the WD-cooling sequence. Figure 6.7 combines all the atmospheric parameters in one plot and, as already suspected, a non-negligible number of stars clustering around the ZAHB at high temperatures in fact show a solar helium abundance. This, of course, would hint that the reason for the stars not being on the HB band is in fact the fitting with a fixed helium abundance.

All the fit results are shown in Table 3 in the appendix A2 and additional plots can be found in the appendix (A3). Judging from these results, they seem to be in agreement with theoretical expectations within the uncertainties.
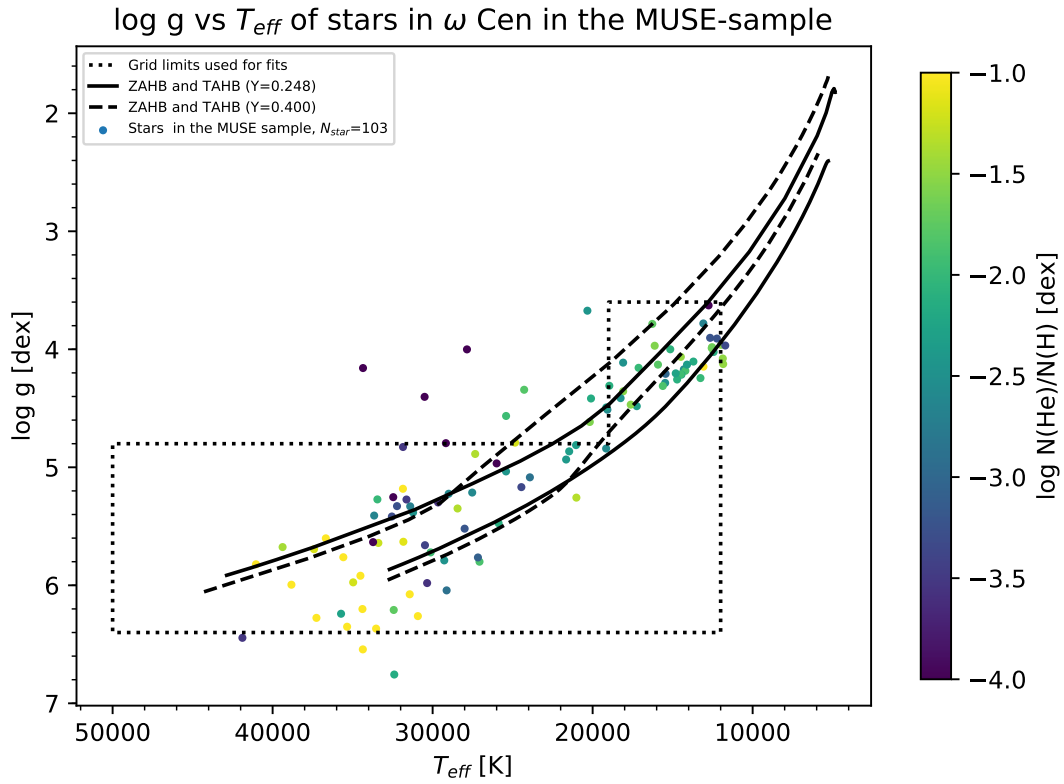
Figure 6.7: log g-T_{eff} diagram of stars in ω Cen color coded with the helium abundance

6.2.3 Comparison to literature results
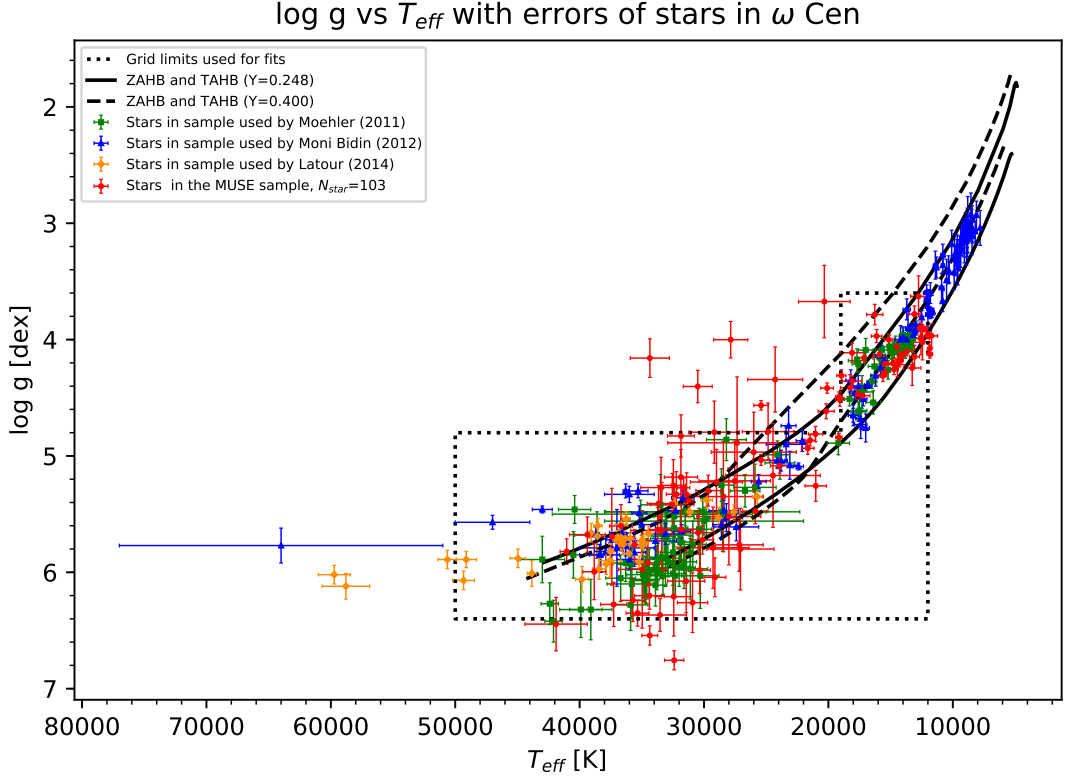
Figure 6.8: $\log g$-T_{eff} diagram of stars in ω Cen from recent studies

Looking at Fig. 6.8, it can be seen that overall the parameters derived from the MUSE data and the previous results are in good agreement, since the stars mostly occupy the same areas in the $\log g$-T_{eff} diagram. As already proposed by Moehler et al. (2011), some of the stars might come from a second helium-enriched population in ω Cen. Since most stars actually fall into the areas predicted for HB stars in both models, the helium enrichment scenario seems plausible. The lower gravities near to the ZAHB found by Moni Bidin et al. (2012) at lower temperatures on the BHB can also be observed in the MUSE sample since, at least at the hotter end of the BHB, the stars in the MUSE sample show even lower gravities than the ones found by Moni Bidin et al. (2012). However, these similarities seem to become less important if one looks at the cool end of the BHB, where the MUSE stars show higher gravities than the ones in the Moni Bidin et al. (2012) sample. Still, this can not exclude that the lower gravities observed by Moni Bidin are in fact true and the ω Cen HB stars are intrinsically different from those in other clusters. In contrast, at higher temperatures the MUSE stars cluster around the ZAHB more often than the stars from the Moni Bidin et al. (2012) sample. The behavior observed amongst the MUSE stars is the same one the stars in the Moehler

et al. (2011) sample exhibit. As the sample by Latour et al. (2014) suggests, the EHB stars cluster at a temperature slightly below 40,000 K. This behavior is seen in all the samples, suggesting that this is the actual behavior EHB stars follow in ω Cen. The cooler stars are all located on the HB band, which is a behavior seen in every sample, except for the sample used by Latour et al. (2014) since this sample only contains the hot stars. The gap between the BHB and EHB is seen in every sample.
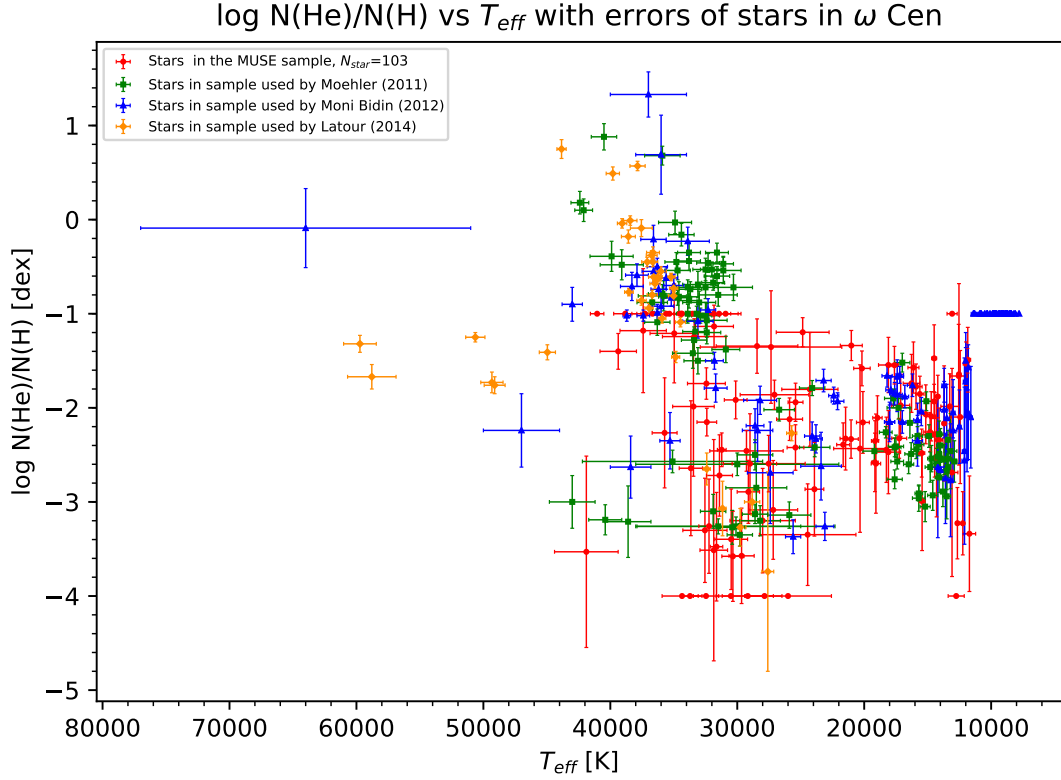
Figure 6.9: Helium abundance T_{eff} diagram of stars in ω Cen from all recent studies

As can be seen in Fig. 6.9, the derived helium abundances are in good agreement with the abundances of the previous results. With regard to the BHB stars, every sample displays a similar behavior. The helium abundance decreases at first and reaches a minimum at about 15,000 K. From there the abundance increases again. The stars near the gap all seem to have a similar helium abundance. The EHB stars, however, seem to cluster in two groups. The helium-poor stars have a wide scatter in temperature, while the helium-rich ones, those that exhibit solar or super solar abundance, have a far more narrow clustering at a temperature of about 35,000 K. The helium abundance, at least for the EHB stars, slightly increases with temperature, which seems to be observed in every sample (see Fig. 6.10). There also seems to be a third group of EHB stars. These

stars are at the hot end of the observed objects and display a helium abundance below solar. This group however is not observed in every sample likely due to selection effects. All the results are in good agreement with each other. Therefore, the MUSE results could support the suspicions that the evolutionary scenarios previously proposed, such as late hot flasher, could be in fact in place in ω Cen.

Since all the samples are in good agreement for ω Cen, this means, that the results of the MUSE sample are very valid. Since the overall sample becomes bigger, the previous results seem even more reliable. Of course, every sample might have certain shortcomings and also outliers, but within the uncertainties, all samples show consistent parameters and are compatible with each other.
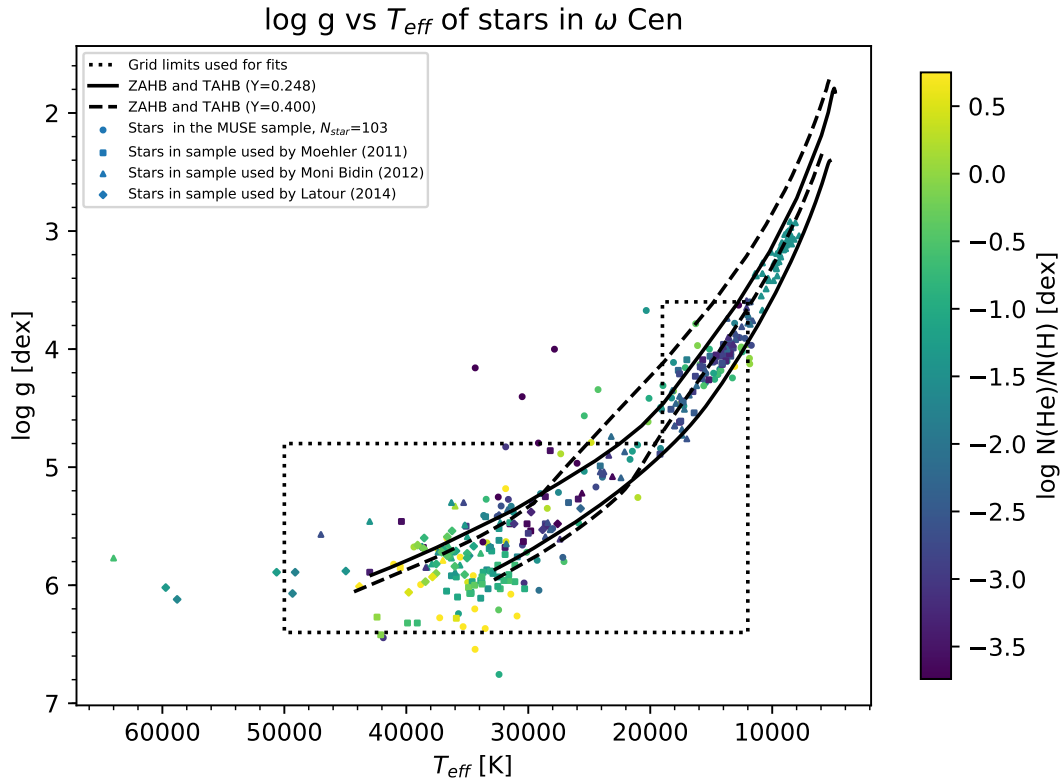
Figure 6.10: log g-T_{eff} diagram of stars from every sample in ω Cen color coded with the helium abundance

6.3 NGC 6752

All 43 stars from the MUSE sample of NGC 6752 had a SNR larger than 20. This is not all too surprising since, although being the smaller sample, the HB of NGC 6752 is not as faint as the one of ω Cen.

6.3.1 Cluster-dynamics

The radial velocity of every star was also determined during the fitting routine for NGC 6752. The dynamics of the GC was investigated in the same way as for ω Cen. As Fig. 6.11 shows, the measured mean radial velocity is $-30.43\pm5.52 \frac{km}{s}$, which is in agreement with the literature value of $-27.7\pm0.2 \frac{km}{s}$ (Harris 1996)[2]. The velocity dispersion of the stars in NGC 6752 was measured to be $8.42 \pm 2.90 \frac{km}{s}$. Again, this value is higher than the literature value of $4.9 \pm 0.4 \frac{km}{s}$ (Harris 1996) for the whole cluster. The dispersion is in excellent agreement with the literature central velocity dispersion of $8.2 \pm 0.6 \frac{km}{s}$ derived from the velocity dispersion profile (Lardo et al. 2015). Again, as for ω Cen, the dynamic properties derived from the MUSE data are in good agreement with the literature values. Due to the low number of stars in this sample, an analysis of the dispersion at a certain distance from the center, similar to the one presented for ω Cen, would not make much sense (however, the plot can be found in the appendix A3 Fig.8).
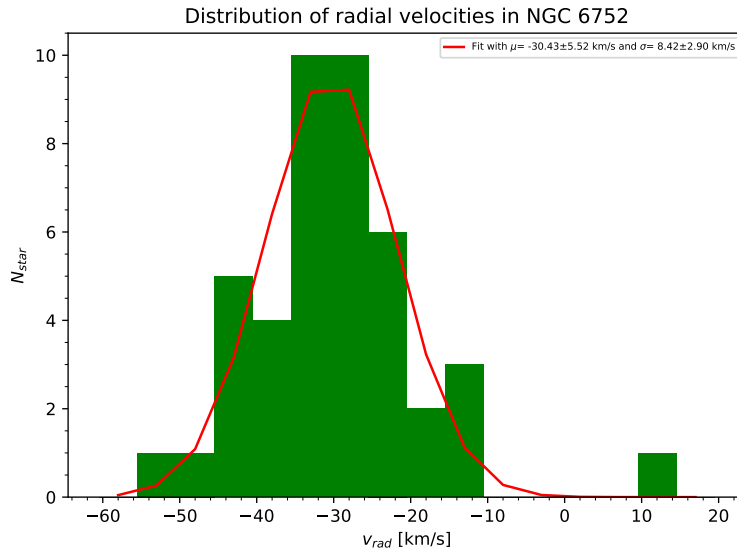
Figure 6.11: Radial velocity distribution of NGC 6752 sample with the Gaussian fit

---

[2] http://physwww.mcmaster.ca/~harris/mwgc.dat

6.3.2 Atmospheric parameters

The distribution of the T_{eff} observed in NGC 6752 can be seen in Fig. 6.12. Again, a gap between the BHB and EHB stars at about 25,000 K is obvious. In NGC 6752, the T_{eff} ranges between 12,000 K and 33,000 K. The BHB stars seem to have two peak temperatures at about 15,000 K and 20,000 K. Due to the relatively low number of objects, it is hard to say if this is a real effect, but on the other hand, the same peaks can be seen in the ω Cen data, which would point towards a real effect. The EHB stars peak slightly below 30,000 K, and a similar but not as prominent peak can be observed in ω Cen. In contrast to ω Cen, the hotter stars are not observed in NGC 6752, with the highest temperature being around 33,000 K. This seems to be a real effect, since, even though the number of stars is smaller than in ω Cen, ω Cen shows quite some stars in this temperature range, so they should, also with the smaller sample being observed in NGC 6752, be observed, if they existed in the cluster. This points to the conclusion that the stars in both clusters behave very differently.
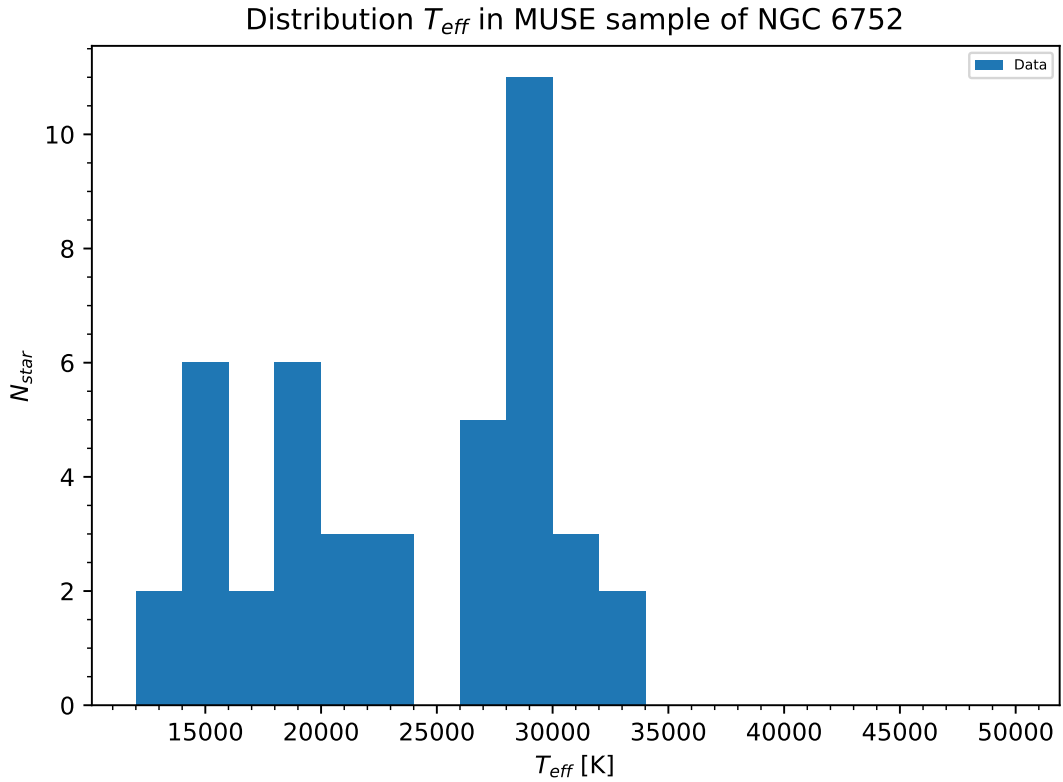
Figure 6.12: Distribution of observed T_{eff} in NGC 6752
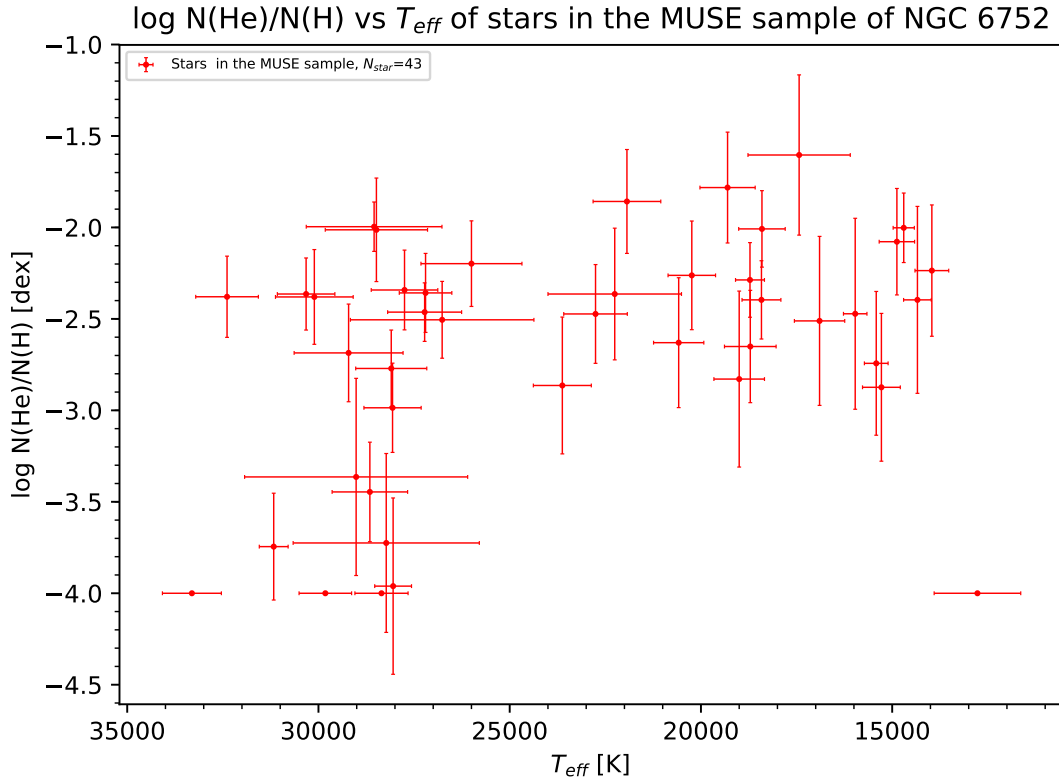
Figure 6.13: Helium abundance as function of T_{eff} in NGC 6752

In NCG 6752 the HB stars are all helium-poor. No star exhibits a helium abundance higher than -1.5 dex. The number of stars that had to be fixed to the lower limit of the grid, is rather low. Therefore, the helium abundance does not have a wide spread in NGC 6752 and the actual abundances are well covered by the models.

A trend with temperature for the BHB stars could be present (see Fig. 6.13). This effect is, as already mentioned, due to diffusion. The BHB stars seem to be scattered between an abundance of -3.0 dex and -1.5 dex.

Compared to the BHB stars, the EHB stars have a wider spread in helium abundance. In general they can be separated into two different groups: one at about -3.5 dex, and one at about -2.5 dex. Most stars in these two groups cluster at a temperature of 28,000 K. No trend with temperature is evident. Judging from the distribution of the stars in the helium-temperature plane, the HB stars in NGC 6752 are cooler on average than those in ω Cen, again making differences between the clusters obvious.

The log g-T_{eff} diagram of NGC 6752 is shown in Fig. 6.14. The BHB stars all fall on the HB band computed with a normal initial helium abundance. Since all the stars are on the HB band of normal initial helium content, the helium-enriched model can be excluded for NGC 6752. The cluster does not seem to harbor a population of He-
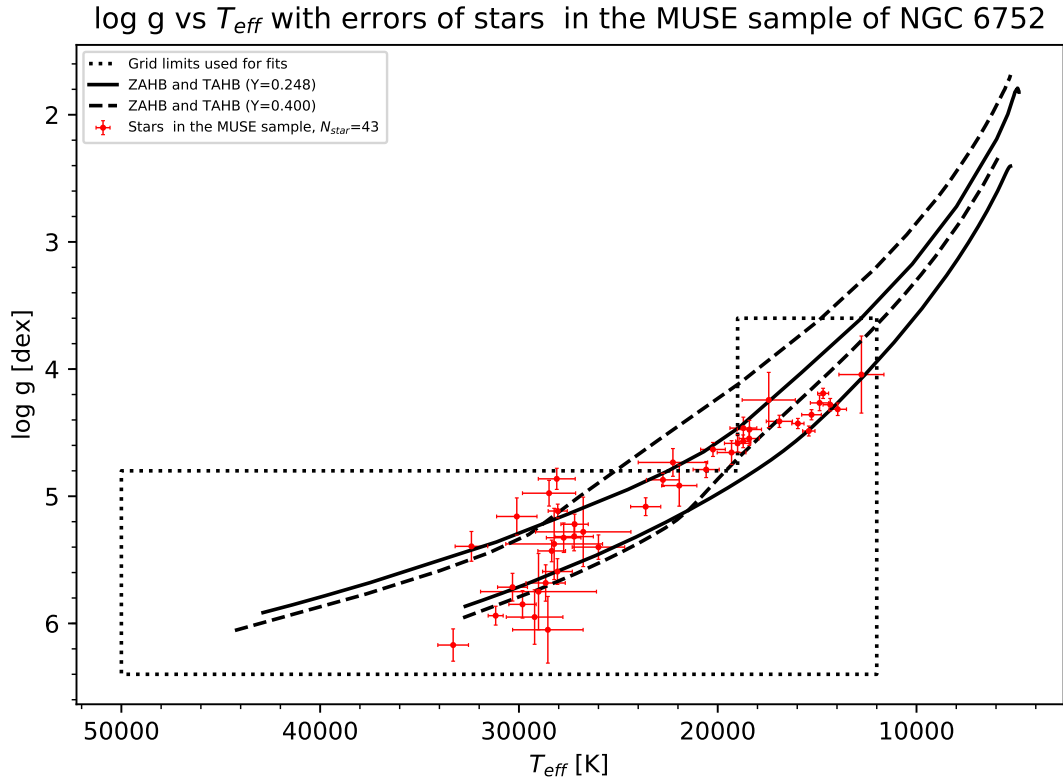
Figure 6.14: log g-T_{eff} diagram of stars in NGC 6752

enriched stars.

A large part of the EHB stars also fall on the HB band, which means they are normal helium-core burning objects. The stars above the TAHB could be explained by these evolving away from the HB, but since the uncertainties could also place them on the HB band, their post-EHB nature is not the only option to explain these stars. The stars beneath the ZAHB, however, could be explained the same way as they were explained for ω Cen. As Fig. 6.15 shows, the stars beneath the ZAHB are mostly helium-poor. Since the helium-poor stars are the only ones that were fixed in the fitting procedure for NGC 6752, the position of the stars beneath the ZAHB can not be explained by the fitting routine.

log g vs T_{eff} of stars in ω Cen in the MUSE-sample of NGC 6752
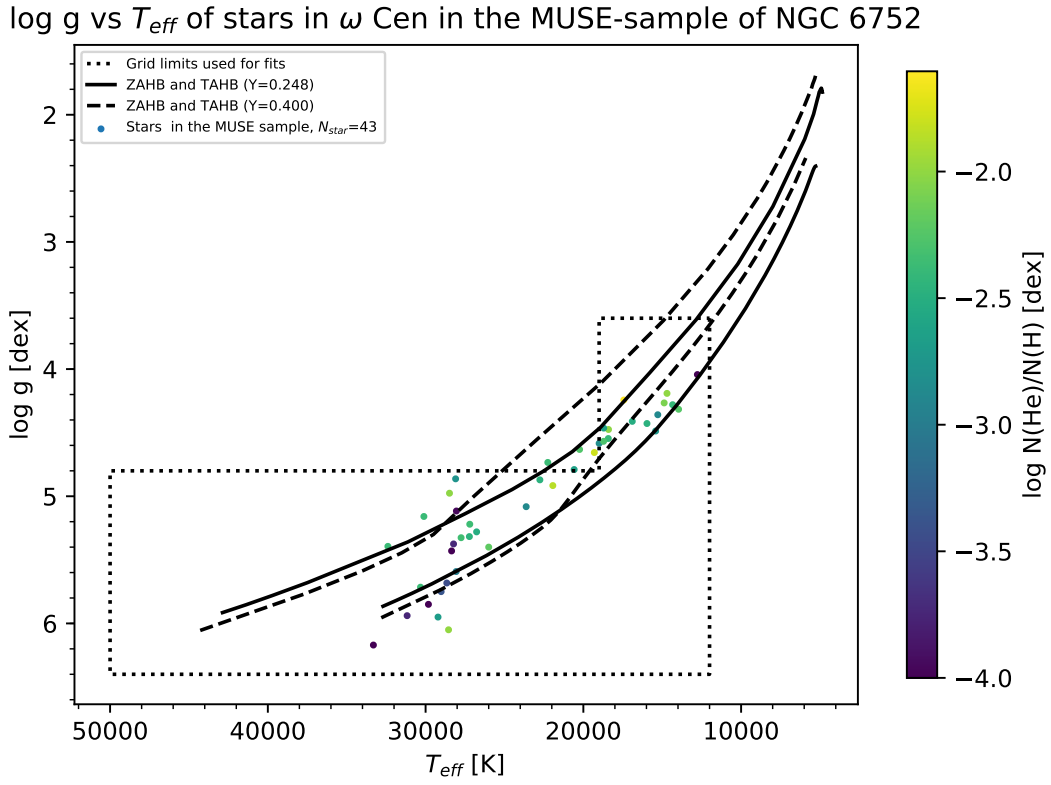
Figure 6.15: log g-T_{eff} diagram of stars in NGC 6752 color coded with the helium abundance

In ω Cen, some stars have helium abundances higher than in NGC 6752. As can be seen from these results, the two clusters investigated show quite some differences among their HB populations. Again, the parameters derived from the NGC 6752 sample are in good agreement with the theoretical expectations. The results are summarized in Table 4 and additional plots can be found in the appendix (A3).

6.3.3 Comparison to literature results
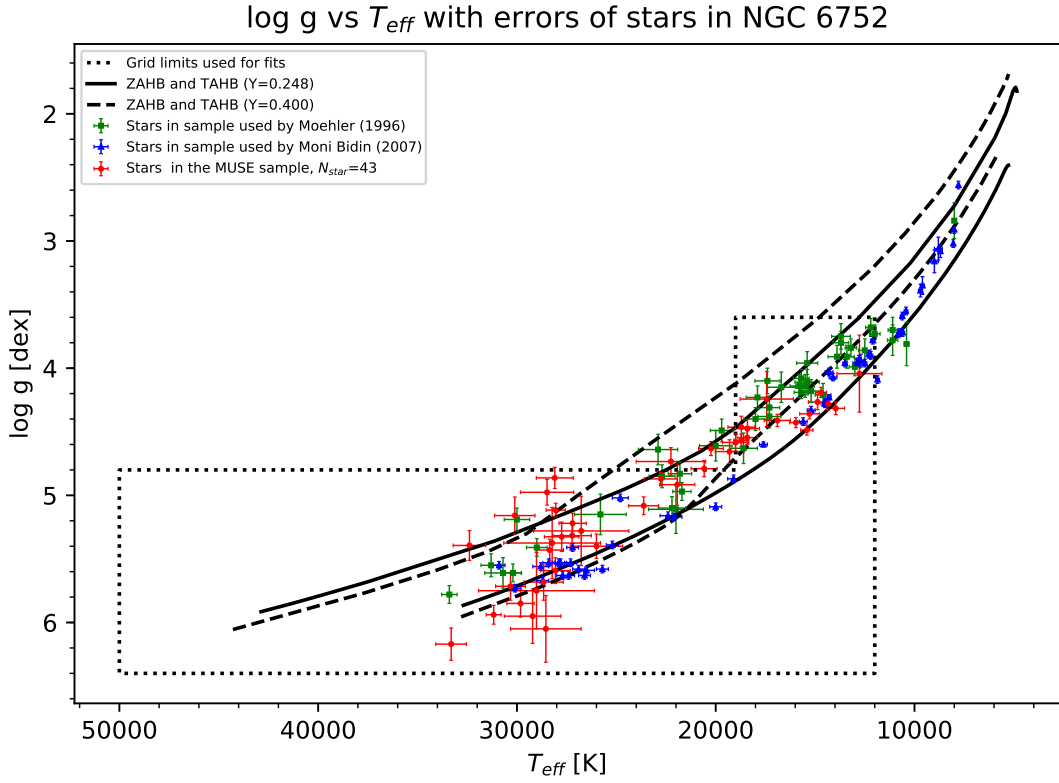
Figure 6.16: log g-T_{eff} diagram of stars in NGC 6752 from recent studies

Figure 6.16 depicts all the stars included in the recent surveys of the HB population of NGC 6752 in the log g-T_{eff} plane. Again the stars from all the samples occupy the same regions in the log g-T_{eff} diagram. The stars mostly fall on the HB band. The atmospheric parameters of the BHB stars from the samples are in good agreement, and although the sample by Moehler et al. (1996) mostly displays lower gravities among the BHB, they are still mostly on the HB band. The gap between the BHB and EHB is observed in every sample. The parameters of the different samples are also in good agreement for the EHB stars, as most stars in all the samples are between the ZAHB and TAHB. All the samples include possible post-EHB objects. As the Moni Bidin et al. (2007) sample, the MUSE sample includes a group of stars, at slightly lower temperatures, with higher gravities than expected. Additionally, in every sample stars hotter than about 33,000 K are non-existent, which is expected based on the CMD of NGC 6752.
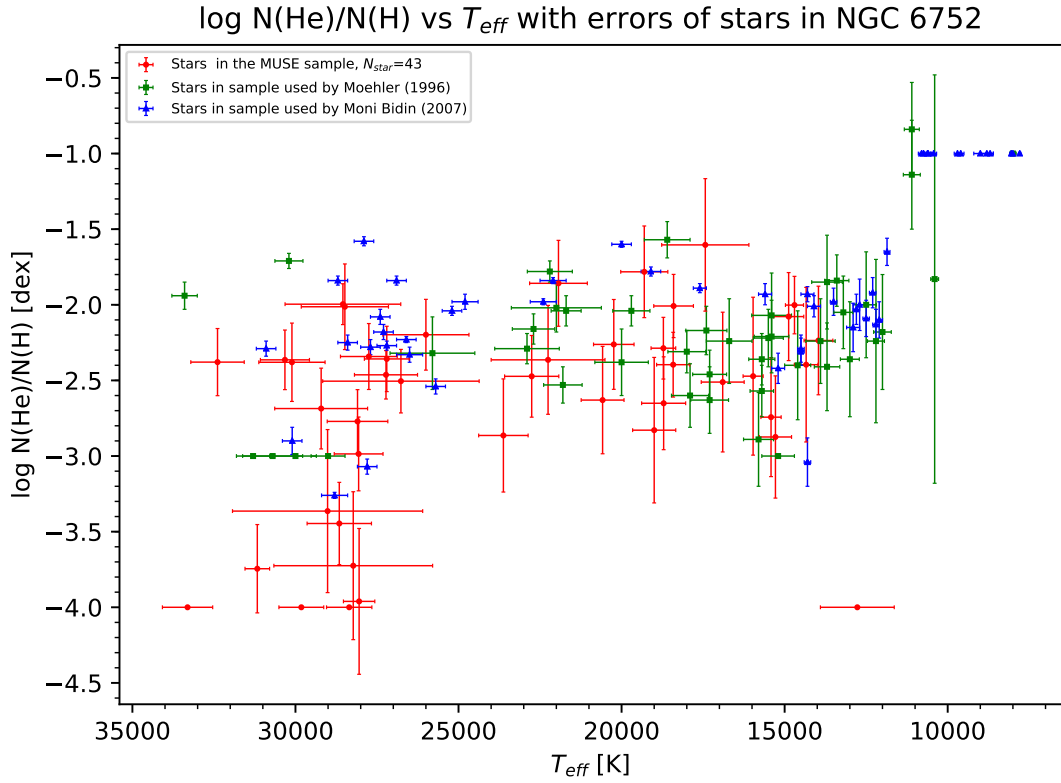
Figure 6.17: helium abundance T_{eff} diagram of stars in NGC 6752 from all recent studies

The samples by Moehler et al. (1996) and Moni Bidin et al. (2007) both show stars with higher helium abundances than the MUSE sample (see Fig. 6.17, 6.18), but these stars are all in a temperature range not included in the MUSE sample. All samples show the same behavior when it comes to the helium abundance. For the BHB, a dip at 15,000 K can be seen and after that an increase of the helium abundance up to the gap, where stars all scatter between a helium abundances of -3 dex and -1.5 dex. Stars beyond the gap all divide into two groups, a helium-poor at about -3.5 dex and group with a higher helium abundance at about -2.0 dex, but only the MUSE sample really shows the first group of objects. All the abundances derived are well below solar.
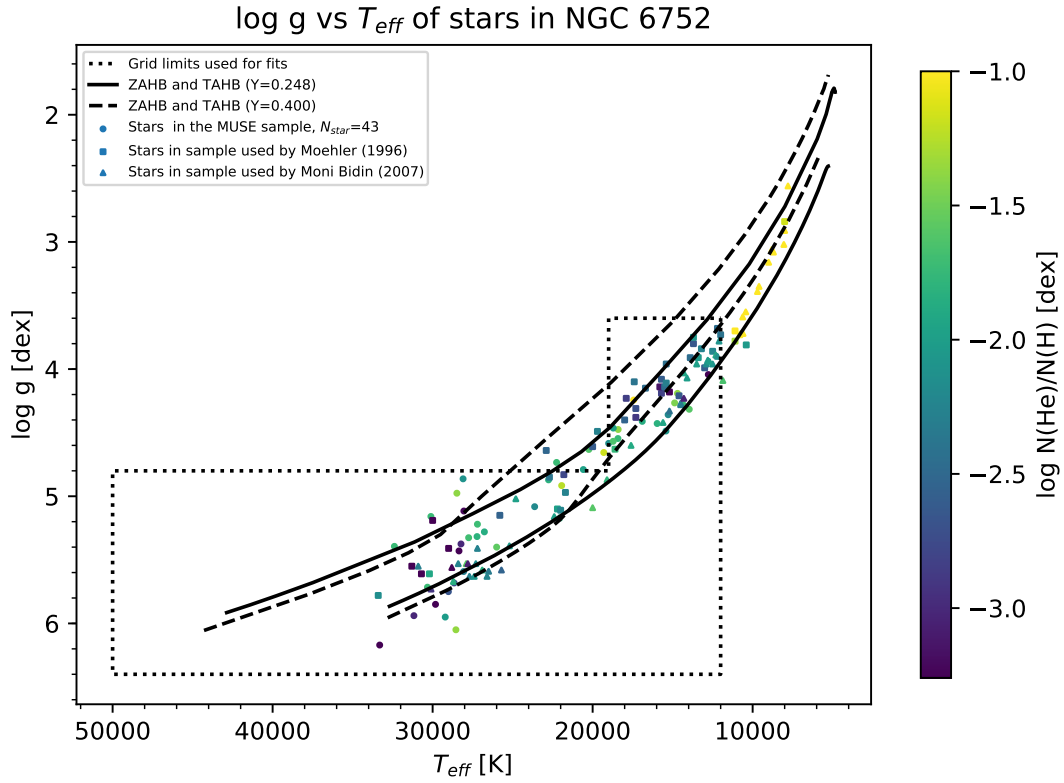
Figure 6.18: log g-T_{eff} diagram of stars from every sample in NGC 6752 color coded with the helium abundance

The cooler stars observed in NGC 6752 have a higher helium abundance than those at higher temperatures. All objects observed are helium poor. Again, the atmospheric parameters of all the samples are in good agreement with each other and mostly agree with the theoretical predictions.

6.4 Influence of synthetic spectra used

As already mentioned, the stars at high T_{eff} below the ZAHB could be explained by the fact that the helium abundance occasionally had to be fixed during the fits. This could explain the seemingly too high gravities derived for those stars. This could be a good way to explain this judging from Fig. 6.10. Another option to explain this part of the results are the synthetic spectra used. As pointed out by Moni Bidin et al. (2007), LTE models may be inadequate for the hot stars. The differences between LTE and non-LTE models is strongest for the effective temperature. An option to explain the stars with the too high gravities might actually be that their temperatures are underestimated by the LTE-models and also the other parameters are in fact slightly different. To investigate this effect a few stars from the ω Cen MUSE sample were chosen randomly and fitted with the NLTE models calculated with TLUSTY/SYNSPEC described in Sect.6.1. The stars were distributed over the entire temperature range, beginning at 20,000 K since this is the lower limit of this grid. The effects on the log g and helium abundance were rather small and, within the errors, the parameters derived were essentially the same. However, effective temperatures from NLTE models are systematically higher than those from LTE models for the hottest stars (see Fig.6.19). Due to the stronger line blanketing of LTE models, the offset is small for temperatures below 35,000 K. From this it can be concluded, even though the highest temperatures are extrapolated since the grid ends at 50,000 K, that for effective temperatures exceeding 35,000 K, NLTE models should be used. Judging from these findings the effect of the models causing the high log g's might be small. Besides, the spectral range offered by MUSE might not be the ideal range to investigate the hottest EHB stars, since the blue part would offer more lines, so probably a combination of a few factors has to be considered to explain the observed behavior of the stars displaying too high gravities.
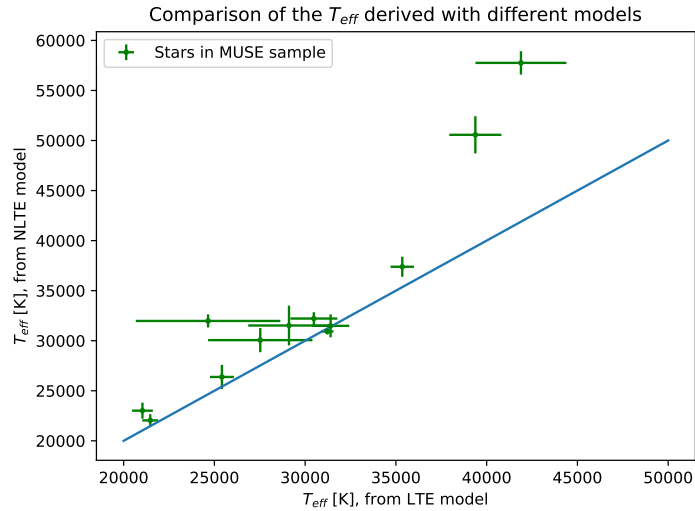
Figure 6.19: Comparison of LTE and non-LTE models

7

Conclusion and outlook

Since globular clusters (GCs) are old objects they are ideal to study stellar populations and evolution. One very diverse population is the horizontal branch (HB). The morphology of the HB in color-magnitude diagrams (CMDs) can be very different. Some clusters only show a red clump, for example 47 Tuc, while other clusters have horizontal branches that are extended into the blue, with the degree of extension also being different from cluster to cluster. For example, ω Cen and NGC 2808 have very extended HBs that, in addition to the blue-horizontal branch (BHB) and the extreme-horizontal branch (EHB), include the so called blue-hook at the very bluest colors. Other clusters such as NGC 6752 also display the BHB and EHB, but do not have a blue-hook. One parameter known to influence the morphology is the metallicity, but it can not be the only parameter. At least one additional parameter is needed to explain this phenomenon, since clusters with similar metallicities can show very different morphologies. Other parameters often proposed as second parameter include age, helium content, core density, the presence of planets, so environmental factors, and many more. This is known as the second parameter problem. By analyzing blue HB stars more insight on this issue can be gained.

The optical spectra of BHB, EHB, and blue-hook stars in the two globular clusters ω Cen and NGC 6752 obtained with the integral field spectrograph MUSE were analyzed. The sample included 121 and 43 stars in the globular clusters ω Cen and NGC 6752, respectively, and were preselected from the CMDs. The regions in the CMDs were chosen to cover the bluest part of the HB. The program stars are all located in the central region of the globular clusters. All previous studies only targeted stars in the outer regions, but with MUSE it is possible to obtain spectra from this crowded region. This is also the first time that spectra of hot HB stars located in the center regions of ω Cen and NGC 6752 were analyzed. The atmospheric parameters, effective temperature, surface gravity, and helium abundance, were derived by fitting metal-line blanketed LTE synthetic spectra to the observed ones. Additionally, the radial velocities of the stars were determined.

In NGC 6752, the stars are found to have temperatures between 12,000 K and 33,000 K, with the EHB stars showing a peak at about 30,000 K. Most stars are located on the HB

band. The trends observed for the helium abundance are the same ones as observed in the field, and the BHB and EHB stars are helium-deficient since no star shows a helium abundance exceeding -1.5 dex which is below the solar level. The helium abundance on the BHB and EHB show the typically expected behavior due to the efficiency of diffusion.

The derived effective temperatures for ω Cen start at 12,000 K and range up to even higher effective temperatures than in NGC 6752. This is not suprising since ω Cen shows a blue-hook in the CMD whereas NGC 6752 does not. As in NGC 6752, most stars are on the HB band. The BHB shows the expected behavior for the helium abundance. The EHB stars in ω Cen, in this sample, group into mainly two groups, a helium-poor one and one around solar values, meaning at slightly higher abundances as in NGC 6752. However, due to the limits of the model grid used, the helium content of some stars, likely the blue-hook stars in ω Cen, could not be quantified, but it can be concluded that they are most likely helium-rich, so compared to NGC 6752, ω Cen has an additional population of helium-rich blue-hook stars. Since some BHB stars in ω Cen are well explained by the helium-enriched scenario, these stars could be part of a helium-enriched subpopulation. This, of course, is a further hint that a helium-enriched population could be present in ω Cen, but additional observations are needed to further investigate this. This scenario does not apply to NGC 6752. The derived mean radial velocities and velocity dispersions are in excellent agreement with the published values for both clusters.

The derived atmospheric parameters are quite similar to the literature values derived from stars in the outer region of the two clusters. Most stars are located on the HB band, as expected. Since the stars in this analysis are located in the central region of their GCs and the literature values are derived from stars in the outer regions, the outer and inner region populations can be compared with each other and although the previous studies used spectra of higher quality and a bluer and wider spectral range, the results are suited for a detailed comparison. Within the uncertainties, no significant differences between the inner and outer region of GCs can be detected, since the stars in the MUSE sample fall into the same regions in the parameter spaces as stars in the outer regions studied earlier in other samples. Therefore, it can be concluded that the HB stars in the inner and outer region of GCs have the same properties. The two regions are very different from each other. The center is much more crowded, so the stellar density is higher and also the dynamic properties are more extreme in the centers than in the outer regions, but since the atmospheric properties are the same for both regions, it can be concluded that environmental factors do not play an important role for the formation of HB stars in GCs.

Since the environment does not seem to influence the formation of HB stars, it can also be concluded that environmental factors are not a parameter influencing the morphology of the HB. Therefore, the environment can be excluded as the second parameter. However, a more sophisticated analysis is needed to clarify this issue.

Since ω Cen is a special cluster because it shows very unique characteristics, and many questions are still unanswered, ω Cen will remain at the focus of research activities. An instrument ideal for this task is MUSE. This instrument is capable of increasing the spectroscopic sample of HB stars in GCs by a large number, hence, the results for these

samples will be more significant than this study. This large number of stars will help to answer many open questions. With several additional GCs observed by MUSE, also the different morphologies of the HBs and the evolution and formation of HB stars will be studied. The spectra MUSE provides are not suited for detailed abundance studies, but, as shown by this analysis, the atmospheric parameters of a very large number of HB stars can be investigated. Once multiple epochs of MUSE spectra become available, the spectra can also be used to look for velocity variations, hence, close binaries containing a HB star could be detected. Again, this could answer questions on the formation of these stars. In addition, observations from other instruments could be used to investigate the stars observed by MUSE in greater detail. Existing and upcoming photometric data, such as light curves, can also be used to search for close binaries and for pulsating HB stars, which are known to exist in some GCs.

Essentially, this analysis shows the great scientific potential of MUSE for the investigation of the HB stars. Therefore, with this unique and powerful instrument, HB research enters a golden age. The future with MUSE promises many new and exciting findings about horizontal branches and globular clusters in general.

References

Ashman, K. M. and Zepf, S. E. (1998). *Globular Cluster Systems*. Cambridge Univ. Press, Cambridge [u.a.].

Bacon, R., Bauer, S., Böhm, P., Boudon, D., Brau-Nogue, S., Caillier, P., Capoani, L., Carollo, C. M., Champavert, N., Contini, T., Daguise, E., Dalle, D., Delabre, B., Devriendt, J., Dreizler, S., Dubois, J.-P., Dupieux, M., Dupin, J.-P., Emsellem, E., Ferruit, P., Franx, M., Gallou, G., Gerssen, J., Guiderdoni, B., Hahn, T., Hofmann, D., Jarno, A., Kelz, A., Koehler, C., Kollatschny, W., Kosmalski, J., Laurent, F., Lilly, S. J., Lizon, J.-L., Loupias, M., Lynn, S., Manescau, A., McDermid, R. M., Monstein, C., Nicklas, H., Perès, L., Pasquini, L., Pécontal, E., Pécontal-Rousset, A., Pello, R., Petit, C., Picat, J.-P., Popow, E., Quirrenbach, A., Reiss, R., Renault, E., Roth, M., Schaye, J., Soucail, G., Steinmetz, M., Ströbele, S., Stuik, R., Weilbacher, P., Wozniak, H., and de Zeeuw, P. T. (2006). Probing unexplored territories with muse: a second-generation instrument for the vlt. *The Messenger*, 124.

Behr, B. B., Cohen, J. G., McCarthy, J. K., and Djorgovski, S. G. (1999). Striking Photospheric Abundance Anomalies in Blue Horizontal-Branch Stars in Globular Cluster M13. *APJ*, 517:L135–L138.

Blanchette, J.-P., Chayer, P., Wesemael, F., Fontaine, G., Fontaine, M., Dupuis, J., Kruk, J. W., and Green, E. M. (2008). FUSE Determination of Abundances in Long-Period Pulsating V1093 Her (PG 1716+426) Stars. *apj*, 678:1329–1341.

Bono, G. (2010). Advanced evolutionary phases in globular clusters. . Empirical and theoretical constraints. *memsai*, 81:863.

Boyles, J., Lorimer, D. R., Turk, P. J., Mnatsakanov, R., Lynch, R. S., Ransom, S. M., Freire, P. C., and Belczynski, K. (2011). Young radio pulsars in galactic globular clusters. *The Astrophysical Journal*, 742(1):51.

Brassard, P., Fontaine, G., Chayer, P., and Green, E. M. (2010). Computations of NLTE Model Atmospheres and Synthetic Spectra at Université de Montréal: Applications to sdB Stars and AM CVn Systems. In Werner, K. and Rauch, T., editors, *American Institute of Physics Conference Series*, volume 1273 of *American Institute of Physics Conference Series*, pages 259–262.

References

Brown, T. M., Cassisi, S., D'Antona, F., Salaris, M., Milone, A. P., Dalessandro, E., Piotto, G., Renzini, A., Sweigart, A. V., Bellini, A., Ortolani, S., Sarajedini, A., Aparicio, A., Bedin, L. R., Anderson, J., Pietrinferni, A., and Nardiello, D. (2016). The Hubble Space Telescope UV Legacy Survey of Galactic Globular Clusters. VII. Implications from the Nearly Universal Nature of Horizontal Branch Discontinuities. *APJ*, 822:44.

Brown, T. M., Lanz, T., Sweigart, A. V., Cracraft, M., Hubeny, I., and Landsman, W. B. (2012). New observational evidence of flash mixing on the white dwarf cooling curve. *arXiv preprint arXiv:1201.4204*.

Brown, T. M., Sweigart, A. V., Lanz, T., Landsman, W. B., and Hubeny, I. (2001). Flash mixing on the white dwarf cooling curve: understanding hot horizontal branch anomalies in ngc 2808. *The Astrophysical Journal*, 562(1):368.

Chromey, F. R. (2010). *To measure the sky*. Cambridge Univ. Press, Cambridge [u.a.].

Drilling, J. S., Jeffery, C. S., Heber, U., Moehler, S., and Napiwotzki, R. (2013). An MK-like system of spectral classification for hot subdwarfs. *AAP*, 551:A31.

D'Souza, R. and Rix, H.-W. (2013). Mass estimates from stellar proper motions: the mass of ω Centauri. *MNRAS*, 429:1887–1901.

Eisenhauer, F. and Raab, W. (2015). Visible/infrared imaging spectroscopy and energy-resolving detectors. *araa*, 53:155–197.

Forbes, D. A. and Bridges, T. (2010). Accreted versus in situ Milky Way globular clusters. *MNRAS*, 404:1203–1214.

Freeman, K. C. and Norris, J. (1981). The chemical composition, structure, and dynamics of globular clusters. *araa*, 19:319–356.

Gratton, R., Sneden, C., and Carretta, E. (2004). Abundance variations within globular clusters. *araa*, 42:385–440.

Grundahl, F., VandenBerg, D. A., and Andersen, M. I. (1998). Strömgren Photometry of Globular Clusters: The Distance and Age of M13, Evidence for Two Populations of Horizontal-Branch Stars. *apjl*, 500:L179–L182.

Harris, W. E. (1996). A Catalog of Parameters for Globular Clusters in the Milky Way. *aj*, 112:1487.

Harris, W. E. and Racine, R. (1979). Globular clusters in galaxies. *araa*, 17:241–274.

Heber, U. (2016). Hot subluminous stars. *pasp*, 128(8):082001.

Heber, U., Kudritzki, R. P., Caloi, V., Castellani, V., and Danziger, J. (1986). A spectroscopic study of HB stars in the galactic globular cluster NGC 6752. *aap*, 162:171–179.

References

Heber, U., Reid, I. N., and Werner, K. (2000). Spectral analysis of multi mode pulsating sdB stars. II. Feige 48, KPD 2109+4401 and PG 1219+534. *aap*, 363:198–207.

Hirsch, H. A. (2009). *Hot subluminous stars: On the Search for Chemical Signatures of their Genesis*. PhD thesis, Friedrich-Alexander University Erlangen-Nürnberg.

Husser, T.-O., Kamann, S., Dreizler, S., Wendt, M., Wulff, N., Bacon, R., Wisotzki, L., Brinchmann, J., Weilbacher, P. M., Roth, M. M., and Monreal-Ibero, A. (2016). Muse crowded field 3d spectroscopy of over 12,000 stars in the globular cluster ngc 6397 - i. the first comprehensive spectroscopic hrd of a globular cluster. *A&A*.

Ivanova, N., Belczynski, K., Fregeau, J. M., and Rasio, F. A. (2005). The evolution of binary fractions in globular clusters. *Monthly Notices of the Royal Astronomical Society*, 358(2):572–584.

Ji, J. and Bregman, J. N. (2015). Binary frequencies in a sample of globular clusters. ii. sample analysis and comparison to models. *The Astrophysical Journal*, 807(1):32.

Kamann, S., Husser, T.-O., Wendt, M., Bacon, R., Brinchmann, J., Dreizler, S., Emsellem, E., Krajnović, D., Monreal-Ibero, A., Roth, M. M., Weilbacher, P. M., and Wisotzki, L. (2016). A stellar census in ngc 6397 with muse. *The Messenger*, 164:18–22.

Kamann, S., Wisotzki, L., and Roth, M. M. (2013). Resolving stellar populations with crowded field 3d spectroscopy . *A&A*, 549:A71.

Krauss, L. M. and Chaboyer, B. (2003). Age estimates of globular clusters in the milky way: Constraints on cosmology. *Science*, 299(5603):65–69.

Lanz, T. and Hubeny, I. (2003). A Grid of Non-LTE Line-blanketed Model Atmospheres of O-Type Stars. *apjs*, 146:417–441.

Lardo, C., Pancino, E., Bellazzini, M., Bragaglia, A., Donati, P., Gilmore, G., Randich, S., Feltzing, S., Jeffries, R. D., Vallenari, A., Alfaro, E. J., Allende Prieto, C., Flaccomio, E., Koposov, S. E., Recio-Blanco, A., Bergemann, M., Carraro, G., Costado, M. T., Damiani, F., Hourihane, A., Jofré, P., de Laverny, P., Marconi, G., Masseron, T., Morbidelli, L., Sacco, G. G., and Worley, C. C. (2015). The Gaia-ESO Survey: Kinematics of seven Galactic globular clusters. *aap*, 573:A115.

Latour, M., Fontaine, G., Green, E. M., Brassard, P., and Chayer, P. (2014). Improved Determination of the Atmospheric Parameters of the Pulsating sdB Star Feige 48. *apj*, 788:65.

Latour, M., Randall, S. K., Chayer, P., Fontaine, G., Calamida, A., Ely, J., Brown, T. M., and Landsman, W. (2017). Just how hot are the ω centauri extreme horizontal branch pulsators? *A&A*.

Latour, M., Randall, S. K., Fontaine, G., Bono, G., Calamida, A., and Brassard, P. (2014). A helium-carbon correlation on the extreme horizontal branch in ω centauri. *The Astrophysical Journal*.

References

Lemke, M. (1997). Extended VCS Stark broadening tables for hydrogen – Lyman to Brackett series. *aaps*, 122.

Marks, M. and Kroupa, P. (2010). Initial conditions for globular clusters and assembly of the old globular cluster population of the milky way. *Monthly Notices of the Royal Astronomical Society*, 406(3):2000–2012.

Meylan, G., Mayor, M., Duquennoy, A., and Dubath, P. (1995). Central velocity dispersion in the globular cluster ω Centauri. *aap*, 303:761.

Moehler, S. (2001). Hot stars in globular clusters: A spectroscopist's view. *Publications of the Astronomical Society of the Pacific*, 113(788):1162.

Moehler, S., Dreizler, S., Lanz, T., Bono, G., Sweigart, A., Calamida, A., and Nonino, M. (2011). The hot horizontal-branch stars in ω centauri. *Astronomy & Astrophysics*, 526:A136.

Moehler, S., Heber, U., and De Boer, K. (1995). Hot hb stars in globular clusters: physical parameters and consequences for theory. i. m 15 and its blue faint horizontal branch with gap. *Astronomy and Astrophysics*, 294:65–79.

Moehler, S., Heber, U., and Rupprecht, G. (1996). Hot hb stars in globular clusters-physical parameters and consequences for theory. iii. ngc 6752 and its long blue vertical branch. *arXiv preprint astro-ph/9607151*.

Momany, Y., Piotto, G., Recio-Blanco, A., Bedin, L. R., Cassisi, S., and Bono, G. (2002). A New Feature along the Extended Blue Horizontal Branch of NGC 6752. *apjl*, 576:L65–L68.

Moni Bidin, C., Catelan, M., Villanova, S., Piotto, G., Altmann, M., Momany, Y., and Moehler, S. (2008). Binaries among extreme horizontal branch stars in globular clusters. In *Hot Subdwarf Stars and Related Objects*, volume 392, page 27.

Moni Bidin, C., Moehler, S., Piotto, G., Momany, Y., and Recio-Blanco, A. (2007). Spectroscopy of horizontal branch stars in ngc 6752-anomalous results on atmospheric parameters and masses. *Astronomy & Astrophysics*, 474(2):505–514.

Moni Bidin, C., Momany, Y., Montalto, M., Catelan, M., Villanova, S., Piotto, G., and Geisler, D. (2015). A hot horizontal branch star with a close k-type main-sequence companion. *The Astrophysical Journal Letters*, 812(2):L31.

Moni Bidin, C., Villanova, S., Piotto, G., Moehler, S., Cassisi, S., and Momany, Y. (2012). Spectroscopy of horizontal branch stars in ω centauri. *Astronomy & Astrophysics*, 547:A109.

Moni Bidin, C., Villanova, S., Piotto, G., Moehler, S., and D'Antona, F. (2011). The peculiar properties of horizontal branch stars in omega centauri. *The Astrophysical Journal*.

References

Napiwotzki, R. (1999). Spectroscopic investigation of old planetaries. IV. Model atmosphere analysis. *aap*, 350:101–119.

Newell, B. and Graham, J. A. (1976). Gaps in the blue horizontal branch. *APJ*, 204:804–809.

Randall, S. K., Calamida, A., Fontaine, G., Monelli, M., Bono, G., Alonso, M. L., Grootel, V. V., Brassard, P., Chayer, P., Catelan, M., Littlefair, S., Dhillon, V. S., and Marsh, T. R. (2016). Pulsating hot o subdwarfs in omega cen: mapping a unique instability strip on the extreme horizontal branch. *A&A*.

Rubenstein, E. P. and Bailyn, C. D. (1997). Hubble space telescope observations of the post-core-collapse globular cluster ngc 6752. ii. a large main-sequence binary population. *The Astrophysical Journal*, 474(2):701.

Sarajedini, A., Anderson, J., Aparicio, A., Bedin, L., Chaboyer, B., Dotter, A., Hempel, M., King, I. R., Majewski, S. R., Marin-Franch, A., Milone, A., Paust, N. E., Piotto, G., Reid, I. N., Rosenberg, A., and Siegel, M. (2010). The HST/ACS Treasury Survey of Galactic Globular Clusters. In *From Stars to Galaxies: Connecting our Understanding of Star and Galaxy Formation*.

Stroeer, A., Heber, U., Lisker, T., Napiwotzki, R., Dreizler, S., Christlieb, N., and Reimers, D. (2007). Hot subdwarfs from the ESO supernova Ia progenitor survey. II. Atmospheric parameters of subdwarf O stars. *Astronomy & Astrophysics*, 462:269–280.

van de Ven, G., van den Bosch, R. C. E., Verolme, E. K., and de Zeeuw, P. T. (2006). The dynamical distance and intrinsic structure of the globular cluster ω Centauri. *aap*, 445:513–543.

Vandenberg, D. A., Bolte, M., and Stetson, P. B. (1996). The age of the galactic globular cluster system. *araa*, 34:461–510.

Villanova, S., Piotto, G., King, I. R., Anderson, J., Bedin, L. R., Gratton, R. G., Cassisi, S., Momany, Y., Bellini, A., Cool, A. M., Recio-Blanco, A., and Renzini, A. (2007). The Multiplicity of the Subgiant Branch of ω Centauri: Evidence for Prolonged Star Formation. *apj*, 663:296–314.

Weilbacher, P. M., Streicher, O., Urrutia, T., Pécontal-Rousset, A., Jarno, A., and Bacon, R. (2014). The MUSE Data Reduction Pipeline: Status after Preliminary Acceptance Europe. In Manset, N. and Forshay, P., editors, *Astronomical Data Analysis Software and Systems XXIII*, volume 485 of *Astronomical Society of the Pacific Conference Series*, page 451.

Z.-X. Lei, X.-F. Chen, Z. H. (2012). Effects of tidally enhanced wind on the horizontal branch morphology of globular clusters. *Astronomy & Astrophysics*, 549.

Acknowledgments

Acknowledgments

Appendices

Appendix A1

Observational data

Table 1: Observational data of stars in the MUSE sample of ω Cen

ID-number	F606W [mag]	SNR	nspec	declination [°]	right ascension [°]
58364	17.8370	21.4370	3	-47.4940	201.7183
59821	18.7980	14.8594	3	-47.4933	201.7143
61488	18.0970	25.3322	4	-47.4923	201.7089
61952	18.7810	21.9212	3	-47.4913	201.7070
63606	15.4310	161.0954	3	-47.4936	201.7014
63764	17.9330	46.8487	6	-47.4931	201.7004
64568	16.0330	56.0373	7	-47.4939	201.6965
65789	15.8740	86.6431	4	-47.4939	201.6883
66492	19.0710	12.8620	2	-47.4917	201.6901
66583	19.0130	7.0074	1	-47.4915	201.6912
67498	15.6070	241.2811	5	-47.4921	201.6853
70396	17.9440	40.7437	4	-47.4915	201.6757
81769	19.1400	26.2796	5	-47.4904	201.7159
82383	19.0690	21.1678	3	-47.4890	201.7149
83242	15.6720	144.7464	5	-47.4900	201.7110
84348	15.6150	202.9692	4	-47.4909	201.7058
84815	18.8370	20.6327	2	-47.4898	201.7041
88289	18.3570	50.7355	8	-47.4885	201.6947
91508	18.7080	26.2728	3	-47.4904	201.6802
91935	15.6590	134.3745	5	-47.4896	201.6776
92191	16.2650	155.3021	5	-47.4885	201.6807
101871	15.9650	197.4687	4	-47.4865	201.7282
103322	16.5370	154.1562	4	-47.4853	201.7241
103748	17.4220	88.4405	2	-47.4871	201.7206
104927	18.8360	35.1376	5	-47.4841	201.7190
106320	18.5610	39.4843	8	-47.4840	201.7130
109246	15.8240	179.8724	9	-47.4870	201.6983
110570	16.5680	157.8297	9	-47.4868	201.6962
110573	18.6190	20.4592	6	-47.4867	201.6963

112401	19.3430	14.7952	1	-47.4852	201.6894
114057	18.7470	23.5939	3	-47.4843	201.6828
115802	15.8460	71.0602	4	-47.4862	201.6750
124027	18.7220	22.9827	4	-47.4817	201.7335
127805	18.6240	46.3293	4	-47.4813	201.7216
128568	15.4650	286.6681	8	-47.4830	201.7142
129695	15.5820	290.7123	11	-47.4805	201.7125
132054	18.6710	18.0179	2	-47.4821	201.7041
132240	17.4540	56.5215	4	-47.4819	201.7037
133047	17.2540	75.3685	8	-47.4835	201.6996
134820	19.0960	28.4227	2	-47.4829	201.6934
135809	18.7430	27.2256	3	-47.4837	201.6893
135937	18.9870	6.3868	2	-47.4831	201.6895
136429	18.8680	21.7343	2	-47.4820	201.6875
137333	15.6720	147.6924	5	-47.4833	201.6846
138764	18.3710	30.6515	7	-47.4827	201.6771
139374	18.9100	30.2858	7	-47.4812	201.6780
142667	18.7960	26.2166	4	-47.4825	201.6614
150918	16.0900	142.6838	4	-47.4780	201.7228
152249	15.4790	202.0151	3	-47.4780	201.7200
153712	17.9670	52.7885	12	-47.4771	201.7167
157019	15.5570	255.4616	17	-47.4804	201.6981
157050	15.4850	203.7383	8	-47.4802	201.7013
159743	18.3710	26.5996	6	-47.4774	201.6923
161050	15.9110	86.1621	9	-47.4776	201.6895
161627	18.9300	27.1761	6	-47.4796	201.6852
162506	17.9520	50.4872	7	-47.4776	201.6844
163623	18.9400	57.9760	8	-47.4783	201.6793
164848	19.0780	27.3384	8	-47.4779	201.6755
165031	18.2160	40.3805	6	-47.4777	201.6744
166544	15.4220	203.0192	4	-47.4773	201.6686
168792	19.2150	24.5952	2	-47.4778	201.6597
176654	15.9410	247.4225	7	-47.4759	201.7178
178209	17.7990	64.0823	8	-47.4752	201.7124
178504	17.7130	62.2091	4	-47.4740	201.7161
179376	15.9740	182.9117	4	-47.4753	201.7104
179475	18.8310	1.9225	1	-47.4748	201.7098
181146	16.8280	50.7432	15	-47.4769	201.6997
181358	18.8680	20.8606	7	-47.4766	201.6971
181837	18.8870	36.2300	6	-47.4749	201.6972
183558	16.3870	132.6811	8	-47.4770	201.6885

183932	18.8420	21.5297	3	-47.4760	201.6871
186637	18.8790	24.7341	5	-47.4755	201.6788
187660	17.3020	127.0211	4	-47.4765	201.6724
188087	16.3480	141.5368	4	-47.4754	201.6715
189451	17.7330	63.2863	4	-47.4744	201.6695
190317	16.4420	143.5132	4	-47.4754	201.6654
190877	17.2480	70.1956	4	-47.4743	201.6616
190932	17.0090	106.7397	4	-47.4737	201.6647
191547	19.0720	16.7681	2	-47.4750	201.6590
199933	18.6890	19.4875	2	-47.4710	201.7188
201451	15.4270	162.0363	4	-47.4705	201.7171
202481	18.7810	23.6158	4	-47.4709	201.7101
206684	18.9490	19.7536	3	-47.4712	201.6925
207152	16.2070	29.6273	3	-47.4731	201.6896
210300	18.7470	40.6835	6	-47.4726	201.6771
210338	17.8370	63.0785	8	-47.4720	201.6811
211555	19.2070	10.7165	2	-47.4723	201.6725
213167	17.7940	26.5138	2	-47.4718	201.6709
213629	16.5740	148.8631	5	-47.4708	201.6663
215742	18.9220	33.2612	6	-47.4725	201.6594
216275	18.9780	29.4126	7	-47.4711	201.6579
216703	16.7600	70.4976	4	-47.4734	201.6504
224456	19.3580	24.2218	1	-47.4694	201.7146
224585	15.8140	130.8092	4	-47.4688	201.7144
224782	16.0960	102.3812	4	-47.4681	201.7164
226377	18.3060	33.3643	4	-47.4672	201.7093
226405	18.3060	30.5459	4	-47.4673	201.7084
226465	19.0640	14.1827	2	-47.4669	201.7113
227264	16.0890	118.0890	4	-47.4684	201.7037
227398	17.9810	24.7797	4	-47.4681	201.7032
228599	18.4860	41.9308	6	-47.4691	201.7000
230954	19.0130	8.6922	3	-47.4701	201.6879
231833	16.4370	75.7058	4	-47.4674	201.6882
233361	17.4110	141.9741	7	-47.4701	201.6779
237785	18.6530	38.1077	5	-47.4688	201.6654
237804	18.5000	57.0768	7	-47.4688	201.6648
237993	18.5520	23.6442	8	-47.4683	201.6633
240693	18.8400	38.0535	4	-47.4695	201.6493
240748	17.1380	138.3917	4	-47.4683	201.6485
248534	16.6320	145.8937	4	-47.4663	201.7106
250782	16.1120	50.3651	1	-47.4641	201.7043

252739	18.3280	27.5172	7	-47.4660	201.6954
253216	18.9190	34.9921	7	-47.4649	201.6966
255748	17.7470	10.7005	4	-47.4649	201.6827
262847	17.1810	87.9780	4	-47.4657	201.6530
302411	18.2970	61.4476	4	-47.4585	201.6615
303239	16.1950	200.8695	4	-47.4591	201.6553

Table 2: Observational data of stars in the MUSE sample of NGC 6752

ID-number	F606W [mag]	SNR	nspec	declination [°]	right ascension [°]
12813	15.3440	267.8579	2	-59.9910	287.7406
12828	15.4180	233.6204	2	-59.9889	287.7400
13507	17.6600	20.1082	2	-59.9899	287.7357
13864	17.2690	124.6968	4	-59.9858	287.7334
15836	15.5950	30.5954	2	-59.9990	287.7211
16331	15.8060	255.5501	4	-59.9940	287.7187
16746	16.6110	84.1042	7	-59.9860	287.7174
16962	17.6870	61.5186	4	-59.9937	287.7160
17733	17.2420	74.7475	2	-59.9929	287.7124
17944	16.2760	118.7097	4	-59.9867	287.7121
19432	17.2600	48.7248	2	-59.9865	287.7035
20102	15.9720	163.1596	4	-59.9854	287.6993
20215	17.8130	59.1510	2	-59.9874	287.6988
20877	17.1180	77.3446	1	-59.9945	287.6936
21185	16.2960	160.2441	2	-59.9879	287.6921
29643	16.9420	80.9238	2	-59.9830	287.7426
29979	16.9430	121.6284	2	-59.9731	287.7404
31030	15.7400	149.3830	2	-59.9783	287.7333
32816	16.9270	49.7306	2	-59.9832	287.7234
32820	15.8920	228.1055	4	-59.9822	287.7239
33102	17.0800	72.5371	4	-59.9841	287.7220
33332	17.9900	50.3427	2	-59.9776	287.7213
33926	17.1160	113.4397	4	-59.9801	287.7187
34548	15.5780	219.8502	4	-59.9746	287.7165
35208	15.4120	305.0496	8	-59.9831	287.7141
35220	15.9440	171.6610	2	-59.9823	287.7140
35473	16.1780	104.6489	3	-59.9731	287.7134
35974	15.3690	223.3151	4	-59.9828	287.7106
36780	16.8900	95.4834	3	-59.9832	287.7065
37003	17.2650	86.5898	2	-59.9722	287.7058
37229	17.5410	72.6145	4	-59.9851	287.7035
37550	16.6100	156.3467	2	-59.9761	287.7019
37802	17.5660	78.1038	4	-59.9850	287.6998
37882	17.6600	38.0953	1	-59.9749	287.6999
37973	17.1210	59.0249	1	-59.9765	287.6992
38141	15.3560	150.7286	4	-59.9817	287.6977
38259	15.5800	112.7001	4	-59.9818	287.6971
38725	16.6030	132.5459	4	-59.9827	287.6940
38786	16.4260	162.5815	2	-59.9754	287.6936

38978	17.5440	83.0153	1	-59.9748	287.6924
39125	17.6450	58.6254	2	-59.9811	287.6910
44211	16.1400	21.4441	2	-59.9712	287.7458
47365	16.3780	141.0229	4	-59.9701	287.7142

Appendix A2

Fit results

Table 3: Fit results for stars in the MUSE sample of ω Cen

ID-number	T_{eff} [K]	log g [dex]	log $N(\text{He})/N(\text{H})$[dex]	$v_{\text{rad}}[\frac{\text{km}}{\text{s}}]$
58364	28997 ± 2095	5.22 ± 0.28	-2.59 ± 0.53	198 ± 8
61488	20328 ± 2078	3.67 ± 0.31	-2.43 ± 0.89	308 ± 21
61952	33391 ± 2502	5.64 ± 0.41	-1.24 ± 0.19	217 ± 99
63606	11842 ± 224	4.12 ± 0.03	-1.49 ± 0.34	238 ± 3
63764	24847 ± 2082	4.79 ± 0.25	-1.20 ± 0.15	232 ± 143
64568	30124 ± 895	5.72 ± 0.12	-1.92 ± 0.20	261 ± 6
65789	15149 ± 336	4.00 ± 0.05	-2.07 ± 0.31	234 ± 4
67498	11977 ± 222	3.96 ± 0.03	-1.53 ± 0.23	207 ± 3
70396	29171 ± 2014	4.80 ± 0.27	-4.00 ± 0.00	200 ± 9
81769	31856 ± 1338	5.18 ± 0.24	-1.00 ± 0.00	224 ± 22
82383	31432 ± 1500	6.08 ± 0.27	-1.00 ± 0.00	241 ± 506
83242	12535 ± 126	3.98 ± 0.03	-1.64 ± 0.96	232 ± 3
84348	12658 ± 135	3.90 ± 0.03	-3.23 ± 0.38	231 ± 2
84815	28000 ± 2577	5.52 ± 0.42	-3.20 ± 0.56	195 ± 61
88289	31402 ± 1026	5.33 ± 0.19	-2.72 ± 0.43	224 ± 8
91508	30344 ± 870	5.98 ± 0.20	-3.58 ± 0.48	202 ± 14
91935	16122 ± 434	3.97 ± 0.06	-1.57 ± 0.27	215 ± 5
92191	15439 ± 227	4.21 ± 0.04	-2.99 ± 0.52	194 ± 3
101871	14299 ± 337	4.17 ± 0.06	-2.54 ± 0.62	197 ± 4
103322	18093 ± 779	4.36 ± 0.04	-1.54 ± 0.29	237 ± 4
103748	23922 ± 738	5.08 ± 0.06	-2.87 ± 0.50	225 ± 71
104927	38825 ± 911	6.00 ± 0.24	-1.00 ± 0.00	191 ± 13
106320	33654 ± 919	5.41 ± 0.15	-2.64 ± 0.72	243 ± 115
109246	13703 ± 145	4.10 ± 0.04	-2.17 ± 0.61	254 ± 3
110570	17242 ± 588	4.48 ± 0.05	-2.32 ± 0.21	207 ± 3
110573	32398 ± 775	6.76 ± 0.08	-2.15 ± 0.15	268 ± 28
114057	32431 ± 1491	6.21 ± 0.34	-1.74 ± 0.17	249 ± 58
115802	13081 ± 462	3.78 ± 0.07	-2.69 ± 1.11	244 ± 5
124027	37413 ± 1826	5.69 ± 0.42	-1.18 ± 0.66	147 ± 32

127805	27527 ± 2876	5.21 ± 0.34	-2.59 ± 0.30	274 ± 7
128568	11865 ± 100	4.08 ± 0.03	-1.50 ± 0.13	255 ± 3
129695	13261 ± 700	4.24 ± 0.15	-1.99 ± 0.35	279 ± 4
132240	20178 ± 650	4.62 ± 0.06	-1.58 ± 0.18	243 ± 14
133047	21036 ± 572	4.81 ± 0.07	-2.33 ± 0.20	232 ± 35
134820	24280 ± 2214	4.34 ± 0.28	-1.80 ± 0.60	282 ± 29
135809	34966 ± 1905	5.97 ± 0.51	-1.21 ± 0.53	232 ± 12
136429	28442 ± 3214	5.35 ± 0.47	-1.34 ± 0.29	289 ± 19
137333	15468 ± 238	4.29 ± 0.03	-2.48 ± 0.26	235 ± 3
138764	32547 ± 1740	5.42 ± 0.27	-3.30 ± 0.55	230 ± 13
139374	37262 ± 1041	6.28 ± 0.19	-1.00 ± 0.00	227 ± 37
142667	33721 ± 643	5.63 ± 0.19	-4.00 ± 0.00	196 ± 11
150918	17128 ± 711	4.16 ± 0.05	-1.97 ± 0.33	233 ± 4
152249	12438 ± 739	4.02 ± 0.15	-2.10 ± 0.71	217 ± 3
153712	30502 ± 1161	4.40 ± 0.14	-4.00 ± 0.00	225 ± 23
157019	12559 ± 665	3.99 ± 0.14	-1.66 ± 0.55	246 ± 3
157050	12233 ± 101	3.91 ± 0.02	-3.23 ± 0.34	198 ± 3
159743	34351 ± 1571	4.16 ± 0.17	-4.00 ± 0.00	217 ± 32
161050	14204 ± 139	4.18 ± 0.03	-1.88 ± 0.23	177 ± 3
161627	33452 ± 1637	5.27 ± 0.26	-1.99 ± 0.74	270 ± 51
162506	21016 ± 864	5.26 ± 0.13	-1.34 ± 0.16	250 ± 6
163623	35581 ± 861	5.76 ± 0.13	-1.00 ± 0.00	235 ± 8
164848	36674 ± 909	5.60 ± 0.18	-1.00 ± 0.00	191 ± 45
165031	30479 ± 1293	5.66 ± 0.18	-3.40 ± 0.53	245 ± 22
166544	16272 ± 656	3.79 ± 0.09	-1.74 ± 0.31	211 ± 3
168792	33533 ± 2118	6.37 ± 0.14	-1.00 ± 0.00	278 ± 18
176654	14450 ± 1288	4.21 ± 0.10	-2.29 ± 0.45	239 ± 3
178209	41040 ± 530	5.82 ± 0.11	-1.00 ± 0.00	221 ± 89
178504	25878 ± 1023	5.47 ± 0.11	-2.12 ± 0.23	287 ± 189
179376	14492 ± 212	4.21 ± 0.04	-1.93 ± 0.18	234 ± 3
181146	19077 ± 372	4.51 ± 0.06	-2.59 ± 0.53	222 ± 8
181358	32462 ± 997	5.25 ± 0.22	-4.00 ± 0.00	188 ± 17
181837	24454 ± 3802	5.17 ± 0.45	-3.35 ± 0.54	268 ± 14
183558	15615 ± 325	4.31 ± 0.05	-1.85 ± 0.19	249 ± 4
183932	34513 ± 981	5.92 ± 0.20	-1.00 ± 0.00	227 ± 26
186637	30922 ± 1216	6.26 ± 0.26	-1.00 ± 0.00	207 ± 15
187660	25414 ± 660	5.04 ± 0.05	-2.42 ± 0.24	275 ± 32
188087	18957 ± 367	4.31 ± 0.05	-2.11 ± 0.23	246 ± 5
189451	31634 ± 491	5.27 ± 0.09	-3.48 ± 0.58	262 ± 7
190317	25409 ± 587	4.57 ± 0.04	-1.94 ± 0.20	255 ± 30
190877	21657 ± 511	4.93 ± 0.05	-2.39 ± 0.23	216 ± 705

190932	19147 ± 282	4.49 ± 0.04	-2.35 ± 0.21	221 ± 6
201451	11712 ± 490	3.97 ± 0.10	-3.34 ± 0.61	246 ± 3
202481	27341 ± 5575	4.89 ± 0.57	-1.35 ± 0.60	271 ± 23
207152	13075 ± 399	4.15 ± 0.10	-1.00 ± 0.00	244 ± 507
210300	34386 ± 1205	6.20 ± 0.12	-1.00 ± 0.00	236 ± 10
210338	39377 ± 1436	5.68 ± 0.15	-1.40 ± 0.19	238 ± 8
213167	27071 ± 2701	5.80 ± 0.35	-1.86 ± 0.15	226 ± 9
213629	18253 ± 779	4.41 ± 0.11	-2.45 ± 0.35	243 ± 5
215742	27168 ± 1926	5.76 ± 0.23	-3.08 ± 0.53	222 ± 8
216275	35345 ± 918	6.35 ± 0.11	-1.00 ± 0.00	232 ± 24
216703	18094 ± 962	4.11 ± 0.08	-2.47 ± 0.44	235 ± 5
224456	27854 ± 1374	4.00 ± 0.16	-4.00 ± 0.00	208 ± 24
224585	14102 ± 268	4.13 ± 0.04	-2.34 ± 0.34	239 ± 4
224782	15917 ± 479	4.13 ± 0.05	-1.77 ± 0.24	234 ± 3
226377	26000 ± 3419	4.97 ± 0.34	-4.00 ± 0.00	234 ± 23
226405	31851 ± 1086	4.83 ± 0.18	-3.51 ± 1.18	232 ± 12
227264	14720 ± 351	4.26 ± 0.04	-2.09 ± 0.26	214 ± 3
227398	12753 ± 634	3.63 ± 0.18	-4.00 ± 0.00	220 ± 8
228599	29274 ± 2890	5.79 ± 0.35	-2.46 ± 0.22	219 ± 8
231833	20102 ± 507	4.42 ± 0.04	-2.15 ± 0.33	253 ± 6
233361	19157 ± 256	4.84 ± 0.04	-2.58 ± 0.31	248 ± 3
237785	31829 ± 1528	5.63 ± 0.28	-1.14 ± 0.23	199 ± 9
237804	29125 ± 882	6.04 ± 0.17	-2.89 ± 0.34	254 ± 8
237993	34362 ± 642	6.54 ± 0.08	-1.00 ± 0.00	228 ± 28
240693	41889 ± 2506	6.45 ± 0.23	-3.53 ± 1.02	226 ± 13
240748	31222 ± 343	5.38 ± 0.05	-2.45 ± 0.18	222 ± 19
248534	17619 ± 258	4.47 ± 0.04	-1.55 ± 0.20	216 ± 4
250782	14489 ± 191	4.06 ± 0.05	-1.47 ± 0.36	232 ± 9
252739	35723 ± 981	6.24 ± 0.18	-2.27 ± 0.58	199 ± 110
253216	32226 ± 801	5.33 ± 0.19	-3.26 ± 0.50	208 ± 55
262847	21466 ± 437	4.87 ± 0.05	-2.33 ± 0.33	263 ± 58
302411	29660 ± 992	5.30 ± 0.13	-3.57 ± 0.51	221 ± 6
303239	14807 ± 502	4.20 ± 0.04	-2.26 ± 0.21	208 ± 3

Table 4: Fit results for stars in the MUSE sample of NGC 6752

ID-number	T_{eff} [K]	log g [dex]	log $N(\text{He})/N(\text{H})$[dex]	$v_{\text{rad}}[\frac{\text{km}}{\text{s}}]$
12813	14340 ± 362	4.28 ± 0.05	-2.40 ± 0.51	-31 ± 2
12828	14698 ± 277	4.19 ± 0.04	-2.00 ± 0.19	-43 ± 2
13507	29015 ± 2916	5.75 ± 0.30	-3.36 ± 0.54	11 ± 14
13864	28063 ± 748	5.59 ± 0.10	-2.99 ± 0.24	-29 ± 3
15836	12771 ± 1132	4.04 ± 0.30	-4.00 ± 0.00	-44 ± 5
16331	18418 ± 508	4.55 ± 0.06	-2.40 ± 0.21	-37 ± 2
16746	28048 ± 481	5.12 ± 0.05	-3.96 ± 0.48	-35 ± 2
16962	28228 ± 2434	5.38 ± 0.28	-3.73 ± 0.49	-29 ± 4
17733	28352 ± 695	5.43 ± 0.09	-4.00 ± 0.00	-26 ± 4
17944	28097 ± 929	4.86 ± 0.08	-2.77 ± 0.21	-40 ± 9
19432	26766 ± 2399	5.28 ± 0.27	-2.50 ± 0.21	-35 ± 5
20102	19000 ± 661	4.58 ± 0.07	-2.83 ± 0.48	-28 ± 3
20215	29820 ± 687	5.85 ± 0.11	-4.00 ± 0.00	-32 ± 6
20877	30108 ± 1016	5.16 ± 0.15	-2.38 ± 0.26	-42 ± 4
21185	19304 ± 722	4.66 ± 0.09	-1.78 ± 0.30	-13 ± 2
29643	21935 ± 885	4.92 ± 0.16	-1.86 ± 0.28	-38 ± 3
29979	27224 ± 967	5.32 ± 0.11	-2.46 ± 0.16	-20 ± 3
31030	18405 ± 608	4.47 ± 0.07	-2.01 ± 0.21	-21 ± 2
32816	28485 ± 1337	4.98 ± 0.10	-2.01 ± 0.28	-49 ± 8
32820	18710 ± 675	4.46 ± 0.09	-2.65 ± 0.31	-36 ± 2
33102	28545 ± 1774	6.05 ± 0.26	-2.00 ± 0.14	-18 ± 3
33332	28656 ± 987	5.68 ± 0.14	-3.45 ± 0.27	-21 ± 5
33926	27200 ± 687	5.22 ± 0.08	-2.36 ± 0.22	-32 ± 3
34548	14877 ± 463	4.27 ± 0.06	-2.08 ± 0.29	-29 ± 2
35208	13963 ± 441	4.32 ± 0.05	-2.24 ± 0.36	-24 ± 2
35220	18718 ± 378	4.57 ± 0.05	-2.29 ± 0.20	-22 ± 3
35473	16899 ± 658	4.41 ± 0.05	-2.51 ± 0.46	-32 ± 2
35974	15282 ± 494	4.36 ± 0.04	-2.87 ± 0.40	-27 ± 2
36780	23624 ± 758	5.08 ± 0.07	-2.86 ± 0.37	-29 ± 3
37003	27750 ± 870	5.33 ± 0.12	-2.34 ± 0.22	-32 ± 3
37229	33309 ± 771	6.17 ± 0.13	-4.00 ± 0.00	-25 ± 7
37550	22254 ± 1745	4.73 ± 0.11	-2.36 ± 0.36	-31 ± 3
37802	26000 ± 1320	5.40 ± 0.10	-2.20 ± 0.23	-41 ± 5
37882	29212 ± 1424	5.95 ± 0.21	-2.69 ± 0.27	-15 ± 7
37973	32390 ± 819	5.39 ± 0.12	-2.38 ± 0.22	-44 ± 5
38141	15417 ± 310	4.49 ± 0.04	-2.74 ± 0.39	-25 ± 2
38259	15967 ± 307	4.43 ± 0.04	-2.47 ± 0.52	-55 ± 3
38725	22756 ± 831	4.87 ± 0.05	-2.47 ± 0.27	-31 ± 3
38786	20582 ± 657	4.79 ± 0.06	-2.63 ± 0.35	-33 ± 3

38978	30323 ± 752	5.71 ± 0.11	-2.36 ± 0.20	-13 ± 4
39125	31170 ± 377	5.94 ± 0.07	-3.75 ± 0.29	-28 ± 4
44211	17433 ± 1337	4.24 ± 0.22	-1.60 ± 0.44	-28 ± 6
47365	20239 ± 621	4.63 ± 0.06	-2.26 ± 0.30	-28 ± 2

Appendix A3

Additional plots

A3.1 ω Cen
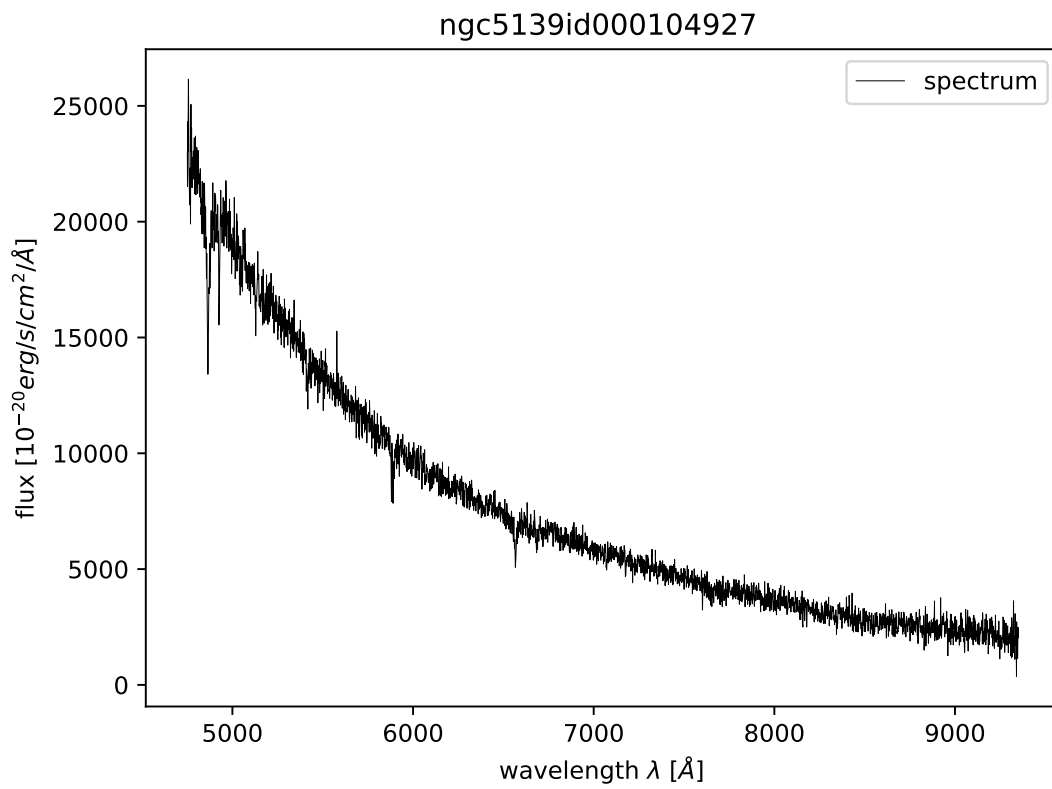
Figure 1: Spectrum of the star 104927, a EHB star, in ω Cen observed with MUSE
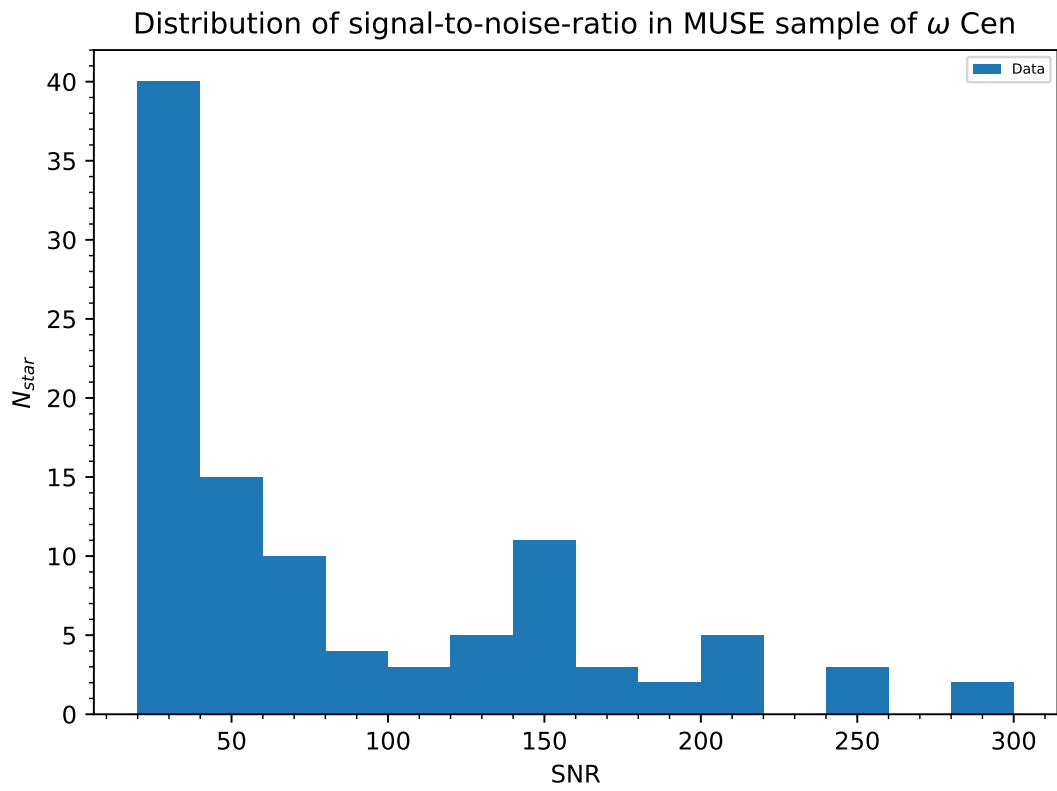
Figure 2: SNR distribution in ω Cen
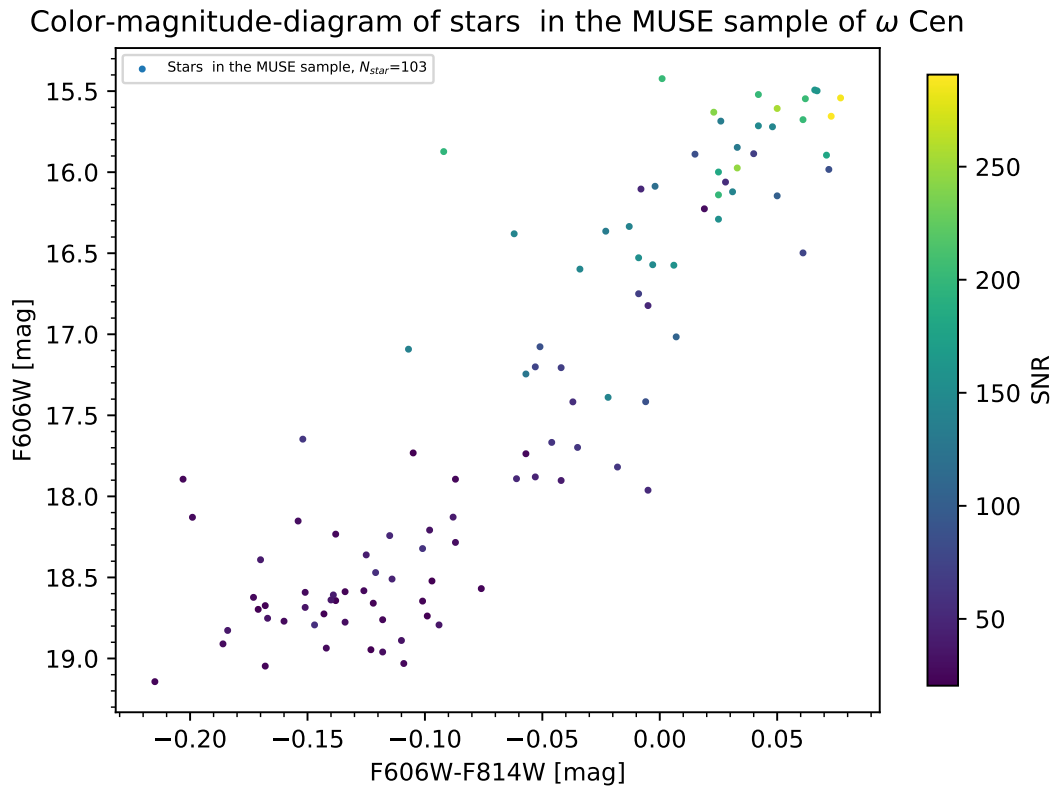
Figure 3: CMD of the ω Cen sample color coded with the SNR
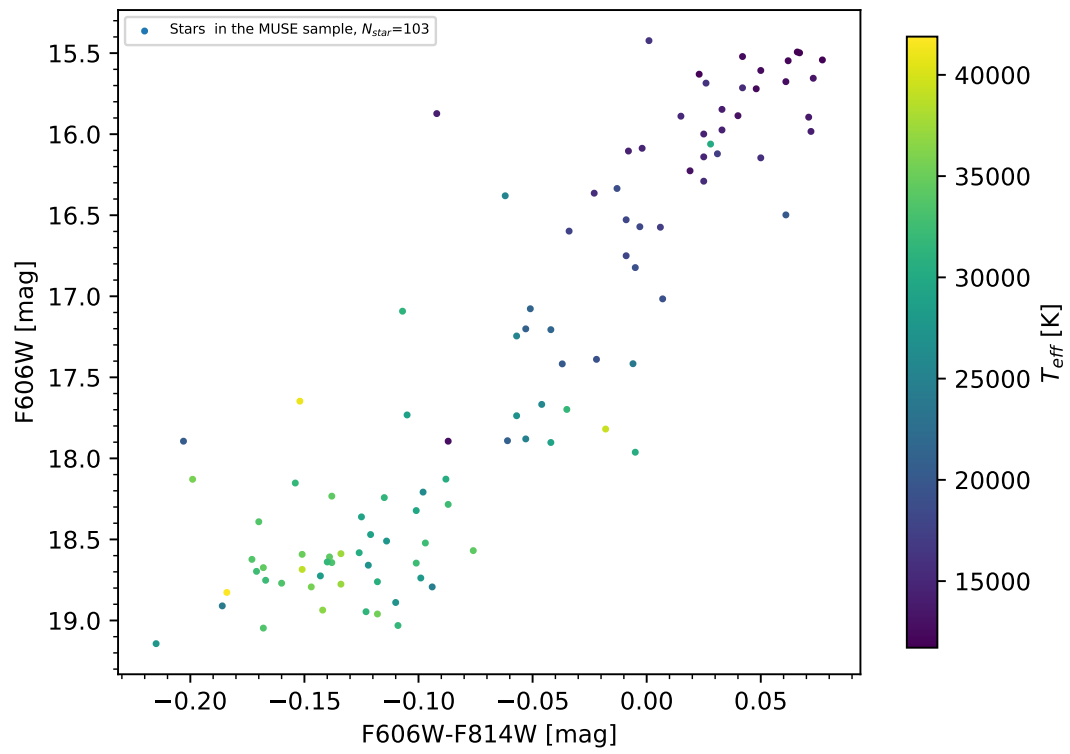
Figure 4: CMD of the ω Cen sample color coded with T_{eff}
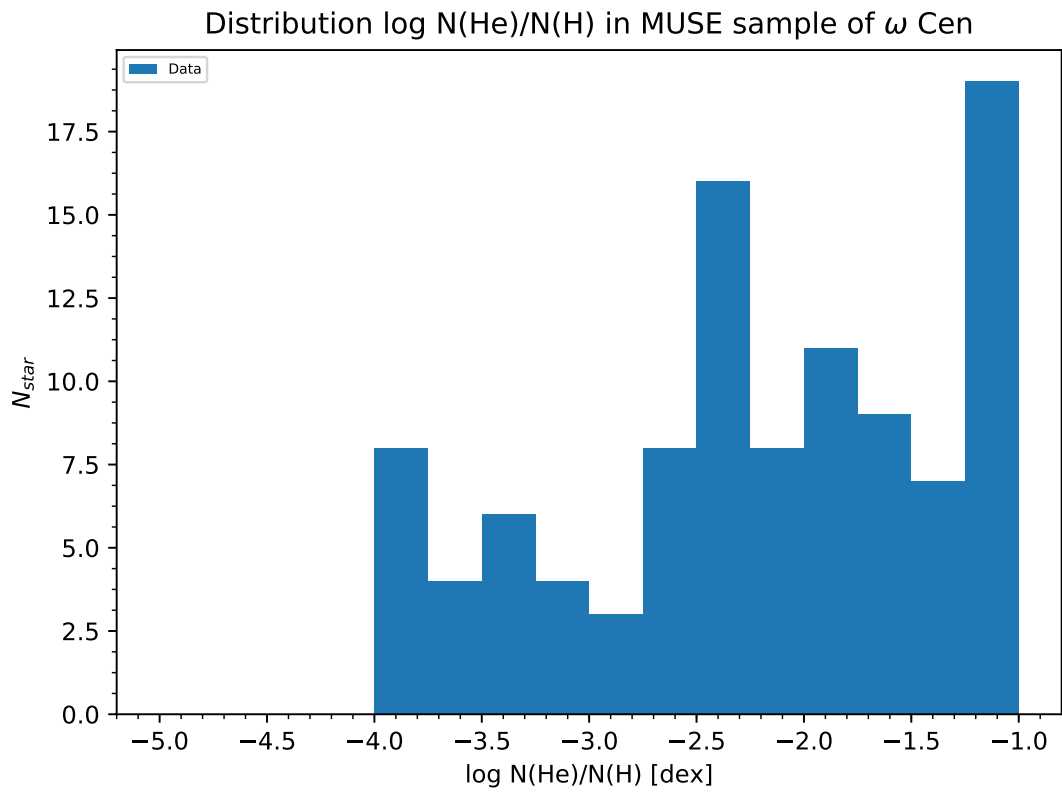
Figure 5: Distribution of observed helium abundances in ω Cen
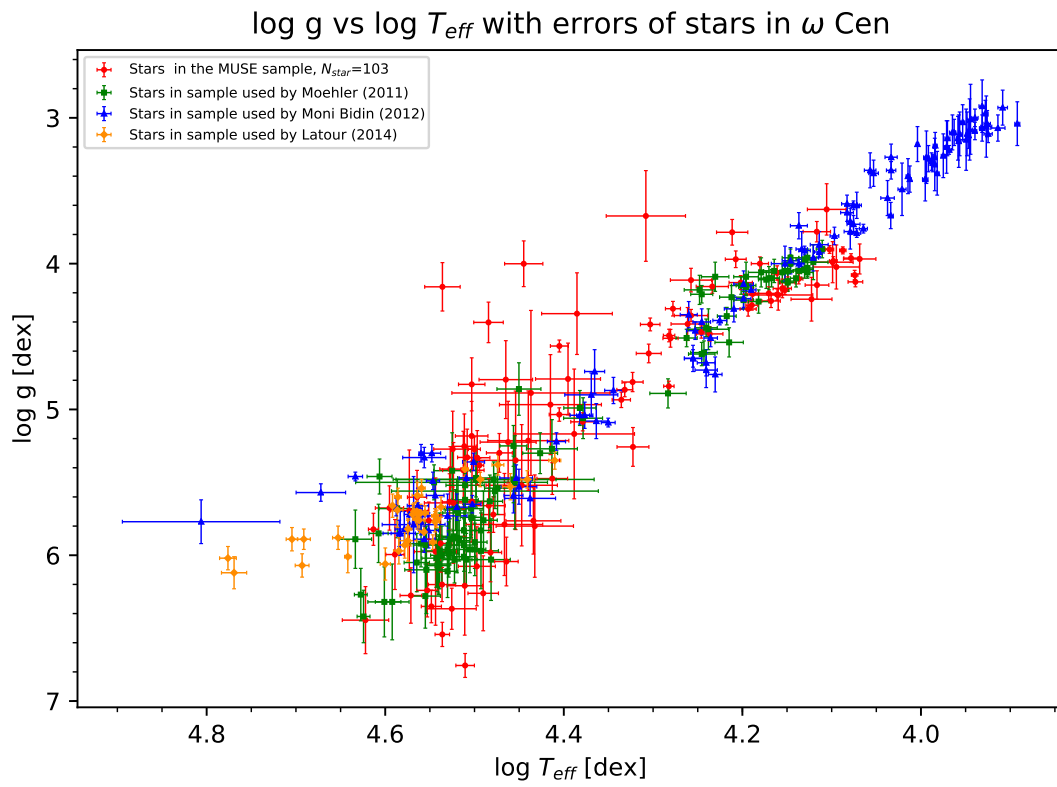
Figure 6: Stars in the ω Cen samples in the log g-log T_{eff} space
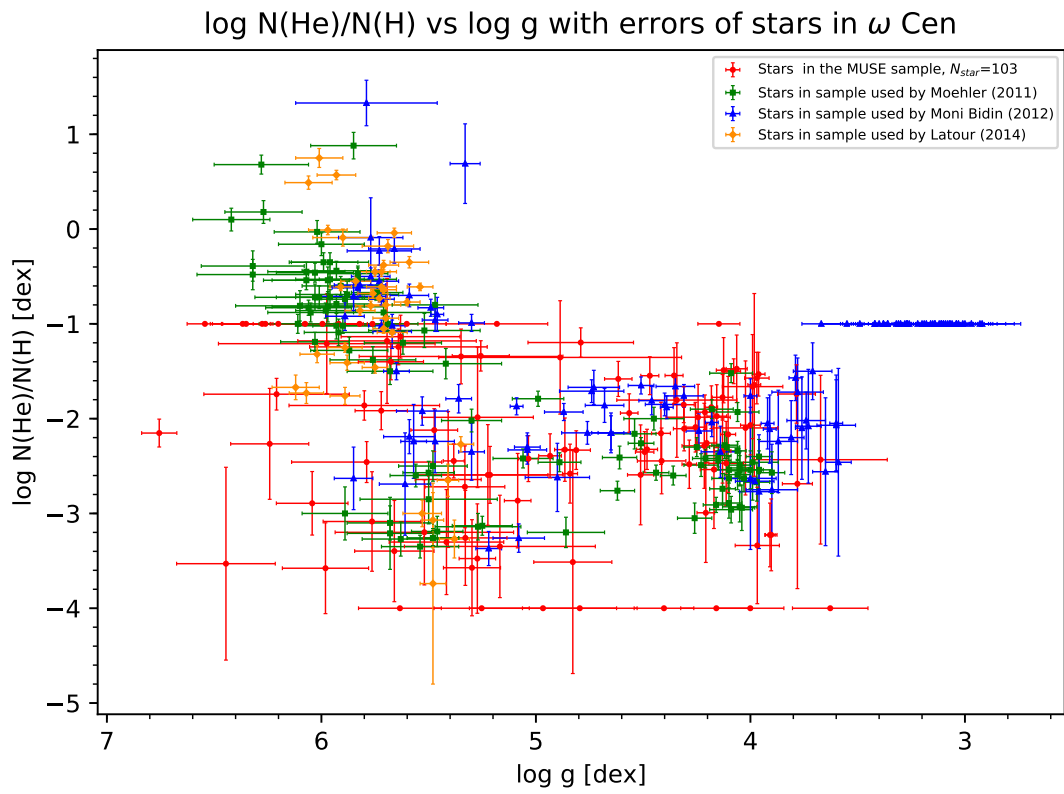
Figure 7: Stars in the ω Cen samples in the log g-helium abundance space

A3.2 NGC 6752
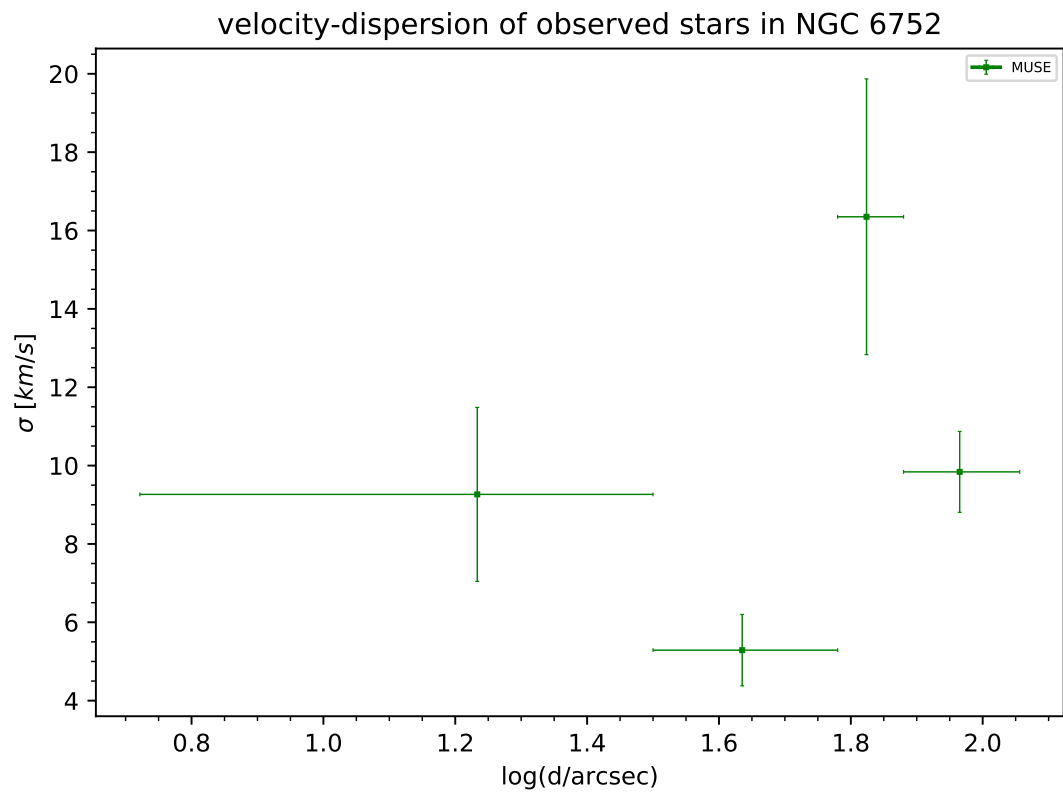
Figure 8: Velocity-dispersion of stars in a certain distance from the center in NGC 6752
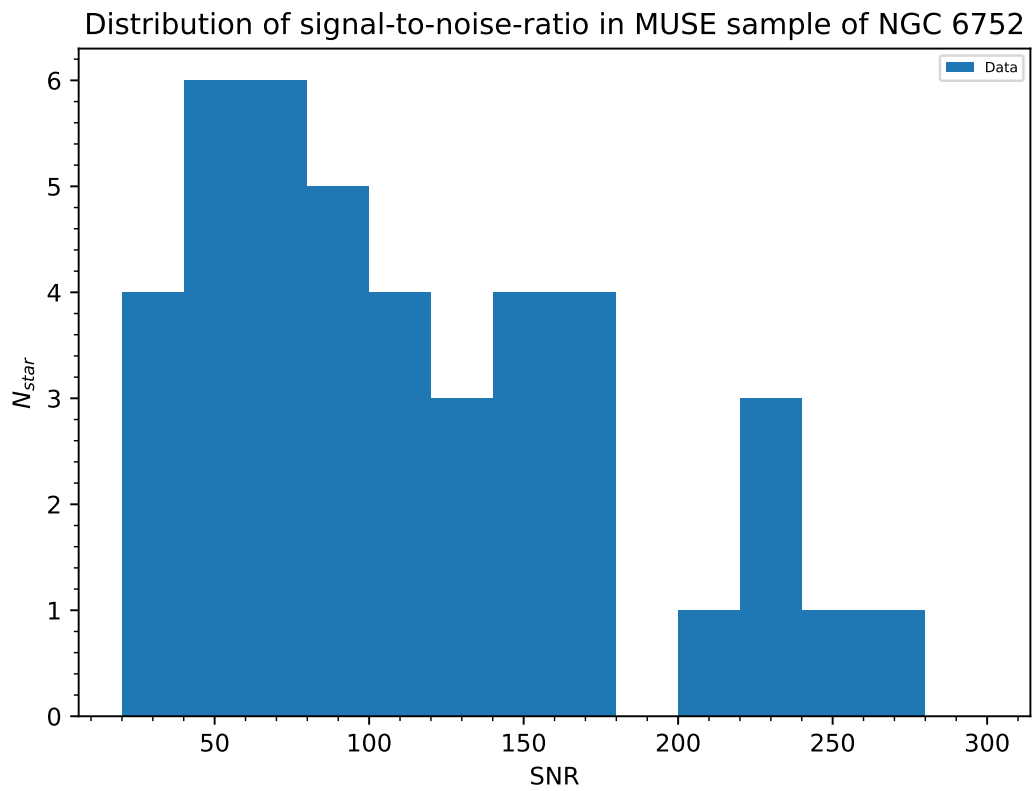
Figure 9: SNR distribution in NGC 6752
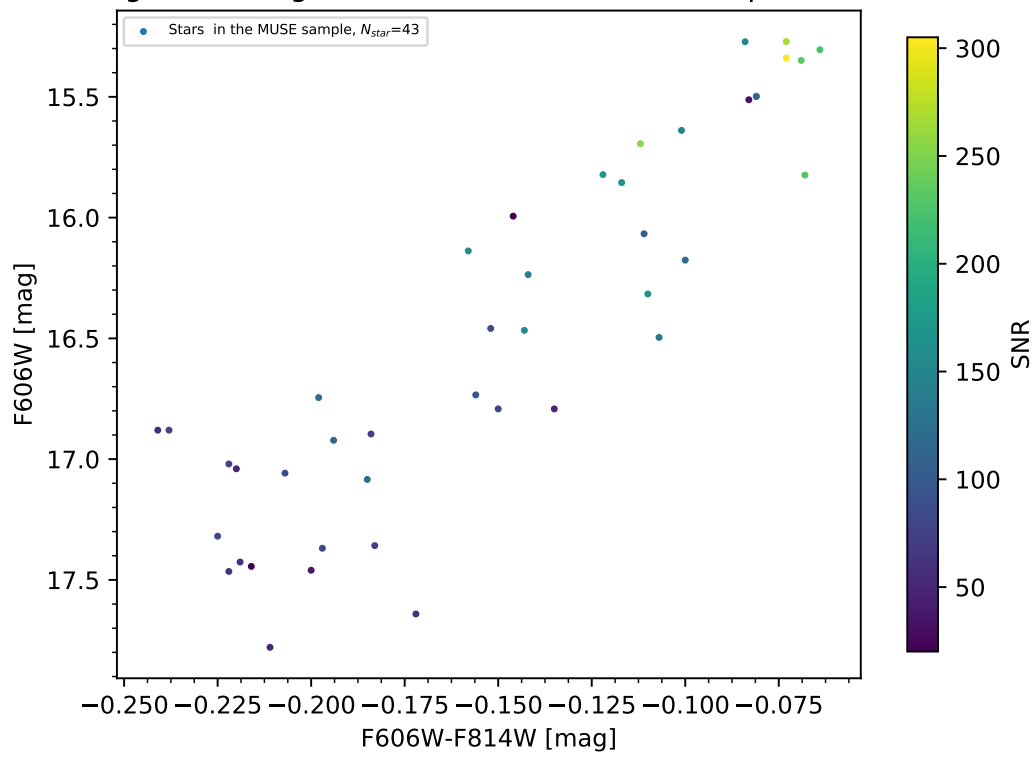
Figure 10: CMD of the NGC 6752 sample color coded with the SNR
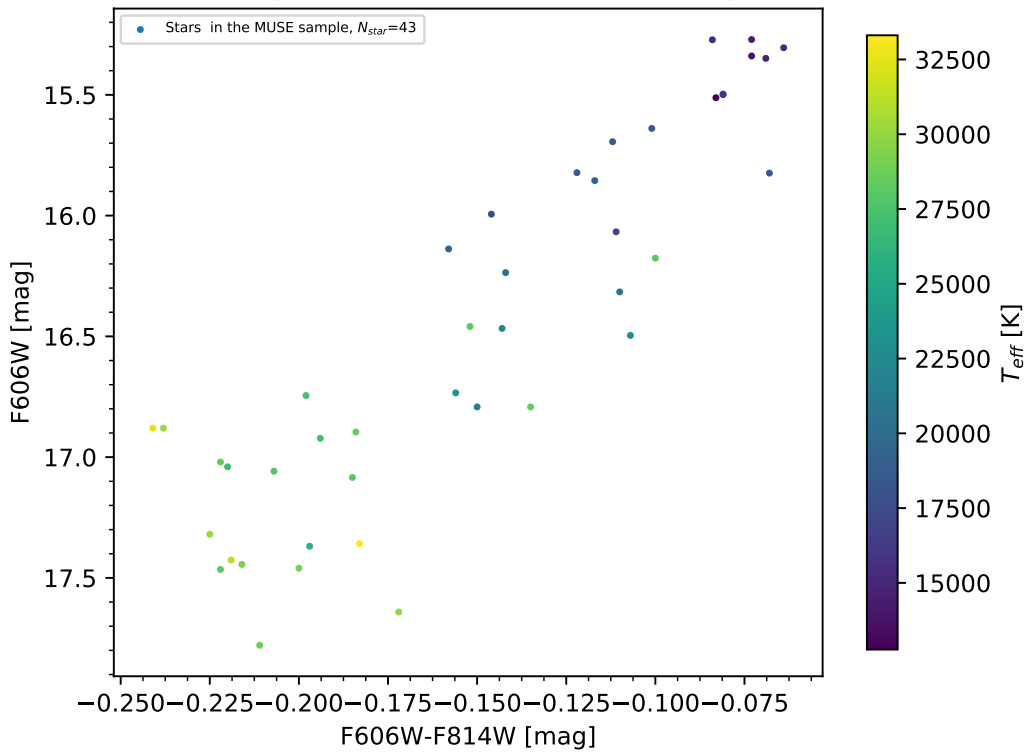
Figure 11: CMD of the NGC 6752 sample color coded with T_{eff}
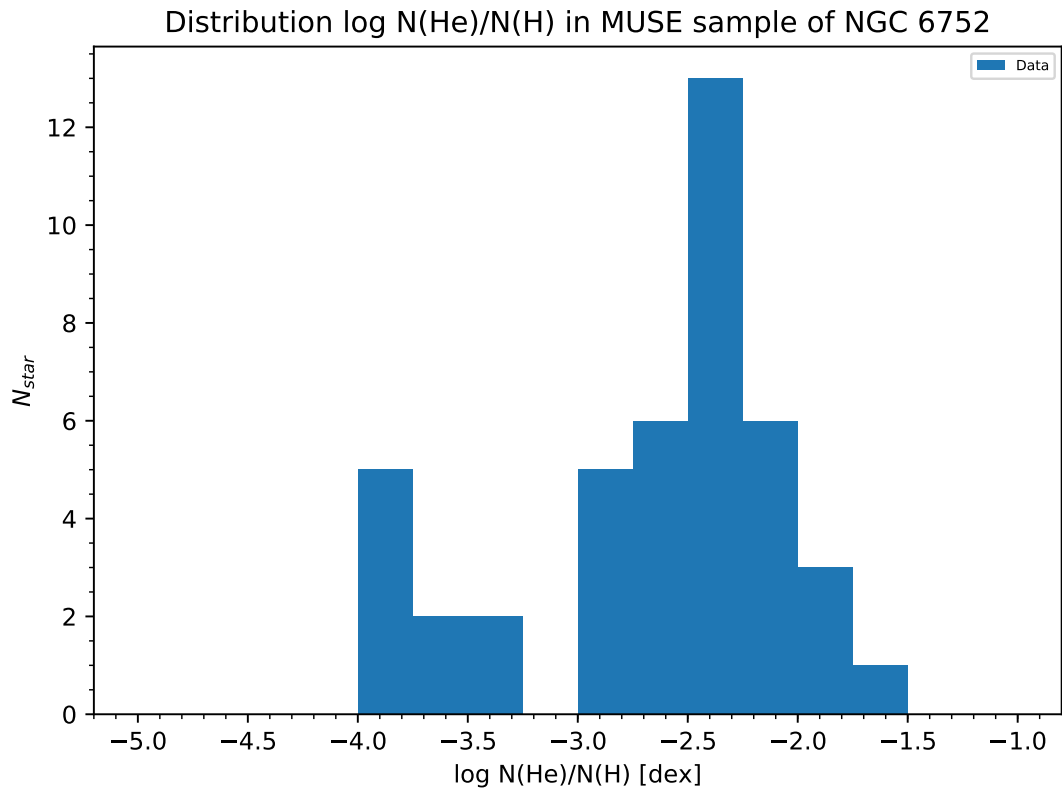
Figure 12: Distribution of observed helium abundances in NGC 6752
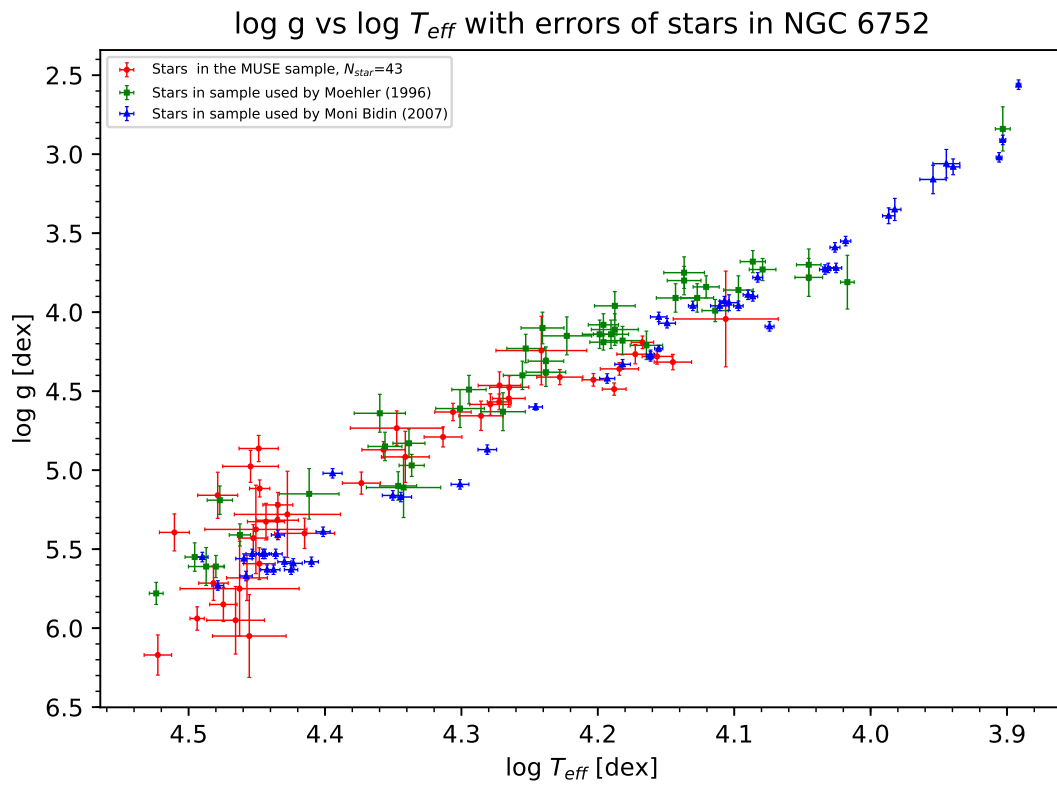
Figure 13: Stars in the NGC 6752 samples in the log g-log T_{eff} space
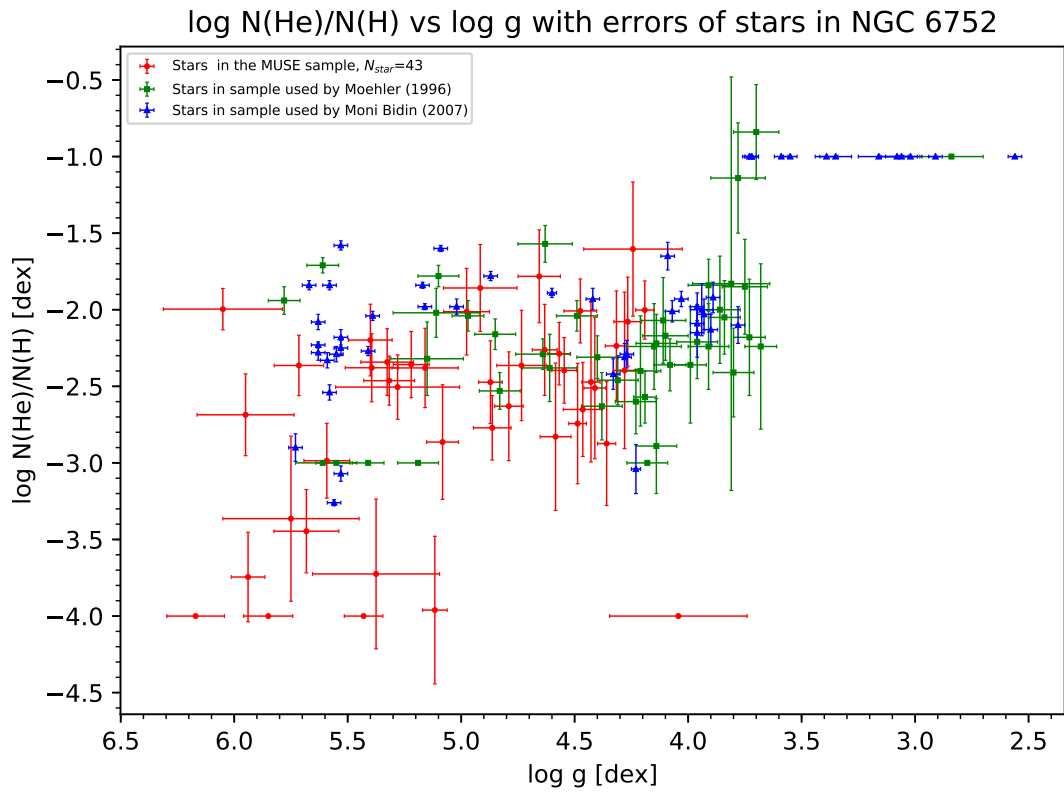
Figure 14: Stars in the NGC 6752 samples in the log g-helium abundance space

Erklärung:

Hiermit bestätige ich, dass ich diese Arbeit selbstständig und nur unter Verwendung der angegebenen Hilfsmittel angefertigt habe.

_____   _____
Ort, Datum   Steven Hämmerich